P-ISSN 0126-3188
E-ISSN 2443-3926

BRIN
BADAN RISET
DAN INOVASI NASIONAL

METALURGI

VOLUME 39 No 3 2024

SCIENTIFIC JOURNAL ACCREDITATION NO.3/E/KPT/2019

National Research and Innovation Agency

Publisher:
National Research and Innovation Agency (BRIN)
KST B.J Habibie Serpong, Tangerang Selatan, Banten, Indonesia, 15314

E-mail: metalurgi@brin.go.id

Science and technology magazine, regularly published every year; one volume consists of 3 editions

METALURGI

VOLUME 39 NUMBER 3 2024

P-ISSN 0126-3188
E-ISSN 2443-3926

ACCREDITATION: SK No. 72/E/KPT/2024

PREFACE

The author gives thanks to Allah for bestowing His blessing and direction, allowing the **Metalurgi Journal Volume 39, Edition 3**, **2024** to be successfully published.

The first article results from Aprilia Erryani and colleagues' research activities on *Self-Healing Behavior of Hydrothermally Engineered HAp/PAA Coatings on Magnesium Alloy WE43*. Rizal Tresna and colleagues presented the second article, *Effect of Surface Roughness on Adhesion Strength and Corrosion Resistance of Silica-Epoxy Composite Coated Low Carbon Steel*. Atika Putri Adenia and colleagues' research activities on *Kinetic Modelling of Solid-Liquid Extraction of Tin from Dimethyltin Dichloride by-Product: Effect of Solvent and Stirring Speed*. For the fourth article, Fendy Rokhmanto presented *Corrosion Behavior of Equiatomic CoCrMoMnNb Bio-High Entropy Alloy Fabricated by Multiple Remelting Processes*. The fifth article by Mochamad Achyarsyah and his colleagues discussed *Investigation of Failure Mechanisms in U-Bend Tubes of Shell-and Tube Heat Exchanger*.

The publication of this volume in the Metalurgi Journal will benefit the advancement of research in Indonesia.

EDITORIAL

METALURGI

ISSN 0126 – 3188 Vol. 39 No. 3, 2024

Keywords sourced from articles. This abstract is reproduced without permission or fee.

Aprilia Erryani[a, b], Fendy Rokhmanto[a, b], Albertus Deny Heri Setyawan[b], Yudi Nugraha Thaha[b], Ahmad Zakiyuddin[a], Ika Kartika[b], Sri Harjanto[a] ([a]Department of Metallurgy and Materials Engineering, Faculty of Engineering, Universitas Indonesia; [b]Research Center for Metallurgy, National Research and Innovation Agency (BRIN)

Metalurgi, Vol. 39 No. 3, 2024

Self-Healing Behavior of Hydrothermally Engineered HAp/PAA Coatings on Magnesium Alloy WE43

This work examines the self-healing properties and corrosion prevention mechanisms of hydrothermally synthesized HAp/PAA (hydroxyapatite/polyacrylic acid) composite coatings on magnesium alloy WE43. The coatings were produced with different PAA concentrations (0.15, 0.3, and 0.5 wt.%) by a hydrothermal method at 140 °C for 3 hours. The composite layers were analyzed using FTIR (fourier transform infrared spectroscopy), SEM (scanning electron microscopy), and EIS (electrochemical impedance spectroscopy) to assess their structural and electrochemical properties, as well as their self-healing capabilities via a scratch–immersion test in Hank's solution at 37 °C for 48 hours. FTIR analysis confirmed the simultaneous presence of HAp and PAA phases without any chemical reaction, indicating physical contact through hydrogen bonding. The elevation of PAA concentration markedly affected coating morphology, resulting in denser and more uniform structures characterized by spherical HAp crystals at 0.5 wt.% PAA. SEM analysis following scratching and immersion demonstrated that the 0.5 wt.% PAA coating successfully preserved surface integrity and displayed partial restoration of the injured region via the reprecipitation of Ca–P compounds. The EIS findings indicated that the 0.5 wt.% PAA coating maintained the maximum impedance modulus (>10^4 Ω·cm^2) and a steady phase angle after 48 hours of immersion, therefore affirming its exceptional corrosion resistance and self-healing properties. The results demonstrate that an ideal PAA content fosters a dense, ion-responsive hybrid layer that effectively reinstates barrier characteristics following mechanical impairment. The hydrothermally produced 0.5 wt.% HAp/PAA coating offers an efficient self-healing and corrosion-resistant surface for WE43 magnesium alloy, indicating significant potential for use in next-generation biodegradable implant systems.

Keywords: Magnesium WE43, hydroxyapatite, polyacrilic acid, hydrothermal coating, self-healing

METALURGI
ISSN 0126 – 3188 Vol. 39 No. 3, 2024

Rizal Tresna[a] , Keanu Rafi Amrullah[a], Aqil Rahmatullah[a], Eni Febriana[b], Latifa Hanum Lalasari[b], Rini Riastuti[a] ([a] Department of Metallurgical and Materials Engineering, Faculty of Engineering, Universitas Indonesia; [b] Research Center for Metallurgy, National Research and Innovation Agency (BRIN))

Metalurgi, Vol. 39 No. 3, 2024

Effect of Surface Roughness on Adhesion Strength and Corrosion Resistance of Silica-Epoxy Composite Coated Low Carbon Steel

Low-carbon steel is widely used in various industries but is susceptible to corrosion in aggressive environments, prompting this study on an epoxy-silica composite coating with variations in silica concentration (0-5 wt.%), sonication dispersion, and surface preparation (abrasive blast cleaning and power tool cleaning); the results showed that abrasive blast cleaning produced a surface roughness of 79 µm and superior adhesion strength (10.48 MPa) compared to power tool cleaning, with a perfect 5A rating in the x-cut tape test for all silica concentrations, while the highest adhesion strength of 14.33 MPa was achieved at 3 wt.% silica, and coating durability tests revealed the best performance exhibiting minimal corrosion propagation of only 0.55 mm after 72 hours at 5 wt.% silica in scratch tests using abrasive blast cleaning, underscoring the significant influence of surface preparation method on coating performance.

Keywords: Epoxy-silica composite, corrosion resistance, surface preparation, adhesion strength, sonication

METALURGI

ISSN 0126 – 3188 Vol. 39 No. 3, 2024

Atika Putri Adenia[a,b], Jayanudin[a], Widya Ernayati Kosimaningrum[a], Teguh Kurniawan[a], Farah Alifia Zulfaidah[b], Yudhistira Madani Putra Siahaan[b] ([a]Department of Chemical Engineering, Faculty of Engineering, Universitas Sultan Ageng Tirtayasa, Indonesia; [b]PT Timah Industri)

Metalurgi, Vol. 39 No. 3, 2024

Kinetic Modelling of Solid-Liquid Extraction of Tin from Dimethyltin Dichloride by-Product: Effect of Solvent and Stirring Speed

Indonesia is the world's second-largest tin exporter; however, downstream utilization of tin remains limited. One potential source of secondary tin is the by-product generated from the production of DMT (dimethyltin dichloride) at PT Timah Industri, which contains 40–70% tin in both organic and inorganic forms. This study aims to investigate the extraction kinetics and evaluate the effects of solvent type and agitation speed on tin recovery from the DMT by-product. Extraction experiments were conducted using different solvents (water, 50% methanol, and pure methanol) and agitation speeds (300 and 400 rpm) for 24 hours. Tin concentrations in the filtrate were determined using XRF (x-ray fluorescence). Kinetic modeling was performed using first-order and second-order models through both linear and non-linear approaches. The results show that the extraction process follows second-order kinetics, with rate constants (k) in the short-time regime ranging from 0.002 to 0.005 $L\cdot(g\cdot min)^{-1}$ and in the long-time regime from 0.0001 to 0.0002 $L\cdot(g\cdot min)^{-1}$. Water demonstrated the highest dissolution capacity (35.35 ± 0.09%), while pure methanol selectively dissolved organotin compounds (30.45 ± 0.12%). The 50% methanol solvent yielded intermediate extraction results (32.65 ± 0.37%) due to the combined characteristics of both solvents. Agitation speed significantly enhanced tin dissolution.

Keywords: Dimethyltin-dichloride-by-product, solid-liquid-extraction, extraction kinetics, valorization.

METALURGI
ISSN 0126 – 3188 Vol. 39 No. 3, 2024

Fendy Rokhmanto[a, b], Aprilia Erryani[a, b], Albertus Deny Heri Setyawan[b], Yudi Nugraha Thaha[b], Ahmad Zakiyuddin[a], Ika Kartika[b], Sri Harjanto[a] ([a]Department of Metallurgy and Materials Engineering, Faculty of Engineering, Universitas Indonesia; [b]Research Center for Metallurgy, National Research and Innovation Agency (BRIN))

Corrosion Behavior of Equiatomic CoCrMoMnNb Bio-High Entropy Alloy Fabricated by Multiple Remelting Processes

High-entropy alloys are described as equiatomic alloys of more than five elements or materials with five or more element constituents with a high mixing entropy (ΔSmix ≥ 1.5R), where the composition of the element is 5–35%, respectively. One application of HEA (high entropy alloys) materials is in the orthopedic field, where they are developed as biomaterials. Behavior, the correlation between the elemental distribution, and the microstructure of the material were investigated during multiple remelting processes known as Bio-HEAs. The development of Bio-HEAs is exciting in terms of design material, fabrication, and their properties. In this paper, the corrosion behavior and the correlation of the elemental distribution and the microstructure of the material were investigated during the multiple remelting process. The equiatomic CoCrMoMnNb was prepared in vacuum arc melting under an argon atmosphere and melted in a water-cooled copper mold. The total amount of ingot was approximately 25 grams, then flipped and remelted several times, 4, 8, and 12 cycles. The final composition of the alloys was confirmed by EDX (energy dispersive x-ray spectroscopy). The microstructure was investigated with an optical microscope and the SEM (scanning electron microscope). The corrosion parameter occurred in Hank's solution at 37°C, at a scan rate of 1 mV/s. The CCM-MnNb fabricated with 8 cycles of the remelting process exhibits the lowest corrosion rate (0.0038 mmpy) and donor densities (2.67×10^{19} cm^{-3}), while the charge transfer resistance number is the highest (18250.94 Ω cm^{-2}). The outstanding corrosion resistance of the alloys is induced by the presence of the finer dendrites and the chromium oxide (Cr_2O_3) protective layer on the alloy's surface.

Keywords: High entropy alloy, bio-HEA, CoCrMo, biomaterial, remelting cycles, corrosion resistance

METALURGI
ISSN 0126 – 3188 Vol. 39 No. 3, 2024

Mochamad Achyarsyah[a], Kus Hanaldi[a], Wiwik Purwadi[a], Gita Novian Hermana[b], Ari Siswanto[b], Cecep Ruskandi[b], Muhammad Rizki Gorbyandi Nadi[b] ([a]Department of Foundry Engineering, Bandung Polytechnic for Manufacturing; [b]Department of Advanced Materials Engineering, Bandung Polytechnic for Manufacturing)

Metalurgi, Vol. 39 No. 3, 2024

Investigation of Failure Mechanisms in U-Bend Tubes of Shell-and Tube Heat Exchanger

The U-bend tubes of a shell-and-tube heat exchanger made of SA-234 Grade WPB carbon steel failed prematurely within 14 days after replacement and welding. This study investigates failure mechanisms through an integrated failure analysis that includes visual inspection, dye penetrant testing, chemical composition analysis, hardness measurements, and microstructural characterization. The results reveal that the tube contained 0.324 wt.% C, exceeding the maximum limit specified by the standard, which promoted the formation of Widmanstätten ferrite and reduced toughness. The welded joint exhibited multiple defects, including porosity and lack of fusion, which acted as stress concentration sites. Hardness measurements showed average values of 205 HV in the weld metal, 199 HV in the HAZ (heat-affected zone), and 184 HV in the base metal. Under operating conditions of 275 °C and 58.48 barg, these defects progressively opened, leading to fluid leakage. The escaping high-pressure fluid accelerated erosion-corrosion, as evidenced by oxygen-rich corrosion products detected by EDS analysis. The findings demonstrate that the combined effects of material non-compliance, poor welding quality, and unfavorable microstructural evolution governed the premature failure. This study provides quantitative insights to improve welding practices and material selection, thereby enhancing the reliability of U-bend tubes in shell-and-tube heat exchangers.

Keywords: U-bend tube, failure analysis, heat exchangers, steel, widmanstätten

Metalurgi (2024) 3: 107-116

METALURGI
Majalah Ilmu dan Teknologi
p-ISSN 0126-3188 | e-ISSN 2443-3926
ejurnalmaterialmetalurgi.lipi.go.id

SELF-HEALING BEHAVIOR OF HYDROTHERMALLY ENGINEERED HAP/PAA COATINGS ON MAGNESIUM ALLOY WE43

Aprilia Erryani[a, b, *], Fendy Rokhmanto[a, b], Albertus Deny Heri Setyawan[b], Yudi Nugraha Thaha[b], Ahmad Zakiyuddin[a], Ika Kartika[b], Sri Harjanto[a,*]

[a]Department of Metallurgical and Materials Engineering, University of Indonesia
Kampus UI, Kukusan, Depok, Indonesia 16424
[b]Research Center for Metallurgy, National Research and Innovation Agency (BRIN)
B.J. Habibie Sains and Technology Area, Banten, Indonesia 15314
*E-mail: aprilia.erryani@gmail.com; sri.harjanto@ui.ac.id

Received: 23-10-2025, Revised: 16-12-2025, Accepted: 17-12-2025

Abstract

This work examines the self-healing properties and corrosion prevention mechanisms of hydrothermally synthesized HAp/PAA (hydroxyapatite/polyacrylic acid) composite coatings on magnesium alloy WE43. The coatings were produced with different PAA concentrations (0.15, 0.3, and 0.5 wt.%) by a hydrothermal method at 140 °C for 3 hours. The composite layers were analyzed using FTIR (fourier transform infrared spectroscopy), SEM (scanning electron microscopy), and EIS (electrochemical impedance spectroscopy) to assess their structural and electrochemical properties, as well as their self-healing capabilities via a scratch–immersion test in Hank's solution at 37 °C for 48 hours. FTIR analysis confirmed the simultaneous presence of HAp and PAA phases without any chemical reaction, indicating physical contact through hydrogen bonding. The elevation of PAA concentration markedly affected coating morphology, resulting in denser and more uniform structures characterized by spherical HAp crystals at 0.5 wt.% PAA. SEM analysis following scratching and immersion demonstrated that the 0.5 wt.% PAA coating successfully preserved surface integrity and displayed partial restoration of the injured region via the reprecipitation of Ca–P compounds. The EIS findings indicated that the 0.5 wt.% PAA coating maintained the maximum impedance modulus (>10^4 Ω·cm²) and a steady phase angle after 48 hours of immersion, therefore affirming its exceptional corrosion resistance and self-healing properties. The results demonstrate that an ideal PAA content fosters a dense, ion-responsive hybrid layer that effectively reinstates barrier characteristics following mechanical impairment. The hydrothermally produced 0.5 wt.% HAp/PAA coating offers an efficient self-healing and corrosion-resistant surface for WE43 magnesium alloy, indicating significant potential for use in next-generation biodegradable implant systems.

Keywords: *Magnesium WE43, hydroxyapatite, polyacrilic acid, hydrothermal coating, self-healing*

1. INTRODUCTION

The concept of self-healing coating has recently gained significant attention in the advancement of biodegradable implant materials. This coating can autonomously restore its protective function following damage, thus prolonging the material's service life and mitigating localized corrosion [1]-[2]. Self-healing mechanisms are crucial for magnesium (Mg)-based materials and their alloys, which, despite exhibiting biocompatibility and mechanical properties similar to natural bone, encounter the challenge of rapid degradation in physiological environments. The elevated corrosion rate results in hydrogen gas production, a rise in local pH, and a reduction in mechanical strength before the complete regeneration of bone tissue [3].

Magnesium alloy WE43 is recognized for its high strength and favorable biocompatibility, attributed to its composition of yttrium (Y), rare earth (RE), and zirconium (Zr) elements [4]-[5].

DOI: 10.55981/metalurgi.2024.780

Metalurgi is Sinta 2 Journal (https://sinta.kemdikbud.go.id/journals/profile/3708) accredited by Ministry of Education, Culture, Research, and Technology, Republic Indonesia

The increased corrosion rate in the body's environment continues to be a significant limitation [6]. A surface system is required that offers protection against corrosion and possesses the ability to self-heal following mechanical or chemical damage [7].

A prevalent method involves the application of hydroxyapatite (HAp) due to its chemical resemblance to bone minerals and its osteoconductive properties[8]-[9]. Pure HAp layers exhibit brittleness, susceptibility to cracking, and weak adhesion to magnesium substrates. Various studies have addressed these weaknesses by combining HAp with biocompatible polymers to enhance the flexibility and interfacial strength of the layers[10]-[11].

PAA is a promising hydrophilic polymer distinguished by a high density of carboxylate groups (-COOH) [12]. These groups bind to calcium ions and form hydrogen bonds with phosphate groups from HAp, which improves adhesion and makes the layers more uniform [13]. PAA acts as an ionic reservoir and diffusion regulator, helping the protective layer to rebuild in places where it has been damaged [14]. The soaking procedure in physiological solution lets the PAA phase move Ca^{2+} and PO_4^{3-} ions to the scratched sites, which helps build protective compounds like HAp or Ca–P crystals. This process creates a self-healing mechanism that rebuilds the protective layer, sealing up microcracks and restoring the barrier's ability to guard against corrosion [15]-[16].

This phenomenon is increasingly reported; however, the systematic study of the relationship between PAA concentration, layer morphology, and self-healing efficiency remains limited. The level of self-healing ability is significantly affected by the microstructure of the layer, ion mobility, and the organic-inorganic ratio in the composite, all of which can be regulated through hydrothermal synthesis parameters.

This study synthesized HAp/PAA composite layers on magnesium alloy WE43 via the hydrothermal method, utilizing varying PAA concentrations of 0.15%, 0.3%, and 0.5% w/v. This study examined the impact of PAA content on self-healing properties and the mechanisms underlying corrosion protection following mechanical surface damage. Evaluation was performed through scratch-immersion testing in Hank's solution and EIS (electrochemical impedance spectroscopy) analysis to assess the evolution of coating integrity over immersion time. This research aims to enhance understanding of the dynamic self-healing mechanism in the HAp/PAA composite system and its potential application as an adaptive smart coating for next-generation biodegradable magnesium implants.

2. MATERIALS AND METHODS

The research employed commercial magnesium alloy WE43, acquired from Smith Metal Products Co., Ltd., UK. The alloys contain 3.7-4.3% Y, 2.4-4.4% RE (Nd, Gd), and 0.4% Zr by weight. The specimens were subjected to wet abrasion with SiC paper up to a 3000-grit level, utilizing ethanol spray as a lubricant. Subsequently, polishing was conducted with a micro cloth utilizing diamond paste of varying particle sizes: 8, 6, 3, 1, and 0.1 μm, respectively. The object underwent ultrasonic cleaning in ethanol for 10 minutes, followed by air drying at ambient temperature. The compounds listed are $Ca(NO_3)_2{\cdot}4H_2O$ and $Na_2HPO_4{\cdot}2H_2O$, both with a purity of 99.9% from Merck. PAA possesses a molecular weight ranging from 800 to 1000 gr/mol. The PAA-HAp coating was applied using the hydrothermal method within a 75 mL reaction autoclave containing a Ca-P solution. A hydrothermal solution was prepared by dissolving 0.05 M calcium nitrate tetrahydrate ($Ca(NO_3)_2{\cdot}4H_2O$) and 0.03 M sodium phosphate dibasic dihydrate ($Na_2HPO_4{\cdot}2H_2O$). The properties of the polymer were analyzed by varying the composition to include 0.15, 0.3, and 0.5 w/v% of PAA in deionized water. Subsequently, the magnesium alloy WE43 was immersed in the deposition solution, positioned within the autoclave, and subjected to heating in an electric oven at a temperature of 140°C. Following a period of 3 hours, the PAA-HAp/Mg samples were subjected to multiple rinses with deionized water and 95% ethanol. Subsequently, a drying process was conducted at a temperature of 60°C to eliminate any impurities.

The coatings' functional groups were analyzed using an FTIR (fourier-transform infrared spectrophotometer) with ATR (attenuated total reflectance) Bruker Alpha II. The coatings' surface morphology and elemental composition were analyzed using a scanning electron microscope (SEM; JEOL JSM-6390). The self-healing capability of the coatings was examined through the scratching method, while the corrosion behavior of the samples was analyzed using electrochemical impedance spectroscopy. A straight scratch was introduced on the coating surface using a stainless-steel blade with a hemispherical tip (tip radius ~20–30 μm) under a constant normal load of 2 N, in accordance with the manual scratch procedures described in ISO 1518-1 and ASTM C1624. The scratch length was approximately 5–8 mm with a controlled

scratching speed of ~1 mm·s^{-1}. The sample was subsequently immersed in Hank's solution at 37°C for a duration of up to 48 hours. The self-healing capability was assessed at 24-hour and 48-hour immersion intervals. Electrochemical impedance spectroscopy (EIS) was conducted using an AutoLab 302 Multi BA electrochemical workstation with Hank's solution (pH 7.4–7.2) at a temperature of 37±1 °C. A three-electrode electrochemical configuration was utilized, comprising a coated WE43 specimen as the working electrode, an Ag/AgCl reference electrode saturated in KCl, and a platinum counter electrode for the electrochemical assessment. The samples were permitted to stabilize at their open circuit potential (OCP) for 5 minutes before the commencement of measurements.

3. Results and Discussion

3.1 Chemical Composition

Figure 1 shows the FTIR spectra of the autoclaving-synthesized HAp/PAA composite coatings on WE43 magnesium alloy with varying PAA concentrations (0.15, 0.3, and 0.5 weight %). The O–H stretching vibrations are related to a broad absorption band observed about 3400 cm^{-1}, which indicates that there are hydroxyl groups from HAp and maybe some water that has been absorbed. Characteristic peaks at around 1700 cm^{-1} have been assigned to the stretching vibrations of carbonyl (C=O) groups from PAA. Clearly visible C–H stretching vibrations about 2900 cm^{-1} confirm the inclusion of the organic PAA phase within the coatings.

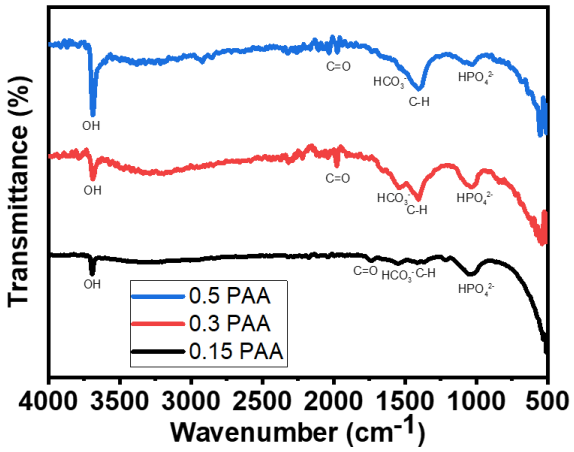

Figure 1. FTIR spectra of magnesium WE 43 coated hydrothermally HAp with a varying composition of PAA

In addition, assigned to the phosphate (HPO_4^{2-}) groups of HAp are significant absorption bands between 1000 and 1100 cm^{-1}, therefore showing the effective development of the inorganic HAp phase. Higher PAA concentrations were shown to cause an increase in the intensity of the C=O and C–H peaks, therefore suggesting a larger polymeric phase contribution in the composite coating. On the other hand, the quite constant phosphate-related peaks indicate that the HAp level was kept constant throughout all the samples. These findings demonstrate that the HAp/PAA composite coatings were effectively generated without any notable chemical reactions and that the connection between HAp and PAA is most likely physical and involves hydrogen bonding [17].

3.2 Surface Morphology

Figure 2 presents the surface morphologies of the hydrothermally synthesized HAp/PAA composite coatings on magnesium alloy WE43 with varying PAA concentrations of (a) 0.15%, (b) 0.3%, and (c) 0.5% (w/v). The variation in PAA concentration markedly affects the nucleation behavior, particle dispersion, and compactness of the coating layers.

At the lowest PAA concentration (0.15%, Fig. 2(a)), the surface shows an inhomogeneous and coarse morphology, characterized by large agglomerated HAp clusters and noticeable voids between them. The uneven distribution of particles indicates insufficient stabilization of HAp precursors, resulting in uncontrolled crystal growth and a porous coating structure. Such morphology may lead to reduced barrier properties and increased susceptibility to corrosion.

When the PAA concentration increases to 0.3% (Fig. 2(b)), the coating surface becomes denser and more uniform, with smaller and more evenly distributed particles. The presence of an adequate amount of PAA improves dispersibility and controls the nucleation of HAp, forming a relatively compact and continuous layer [18]. However, minor textural irregularities are still visible, suggesting partial agglomeration during growth. At the highest concentration (0.5% PAA, Fig. 2(c)), the surface morphology transforms into a fine, compact layer composed of uniformly distributed spherical-like HAp crystals. The excess PAA promotes rapid nucleation while restricting further crystal growth, producing nanosized spherical particles that tightly fill the surface. This morphology results in a smooth and highly compact coating, indicating improved interface coverage and reduced surface defects. The uniform and dense arrangement of spherical HAp particles likely enhances corrosion protection by limiting electrolyte penetration and stabilizing the interfacial layer [19]. 3.3 Self-Healing Evaluation

Figure 3 shows how the scratched HAp/PAA coatings on the WE43 alloy looked before and

after being put in Hank's solution for 24 and 48 hours. The changes in surface characteristics can tell us about how well each coating composition can repair itself, how well it stays intact, and how it reacts to corrosion. In the first stage (Figs. 3(a), 3(d), and 3(g)), the scratched regions are easy to see on all of the coatings. This sign indicates that mechanical damage has exposed the substrate. The surface of the 0.15 PAA coating (Fig. 3(a)) is very rough, and debris builds up unevenly along the scratch. The 0.3 PAA (Figure 3d) and 0.5 PAA (Fig. 3(g)) coatings, on the other hand, seem more compact and continuous, which means they stick better and are stronger. The 0.5 PAA sample, in particular, has a smoother and denser surface surrounding the scratch. This suggests that the composite layer and the substrate are more strongly bonded at the interface [20].

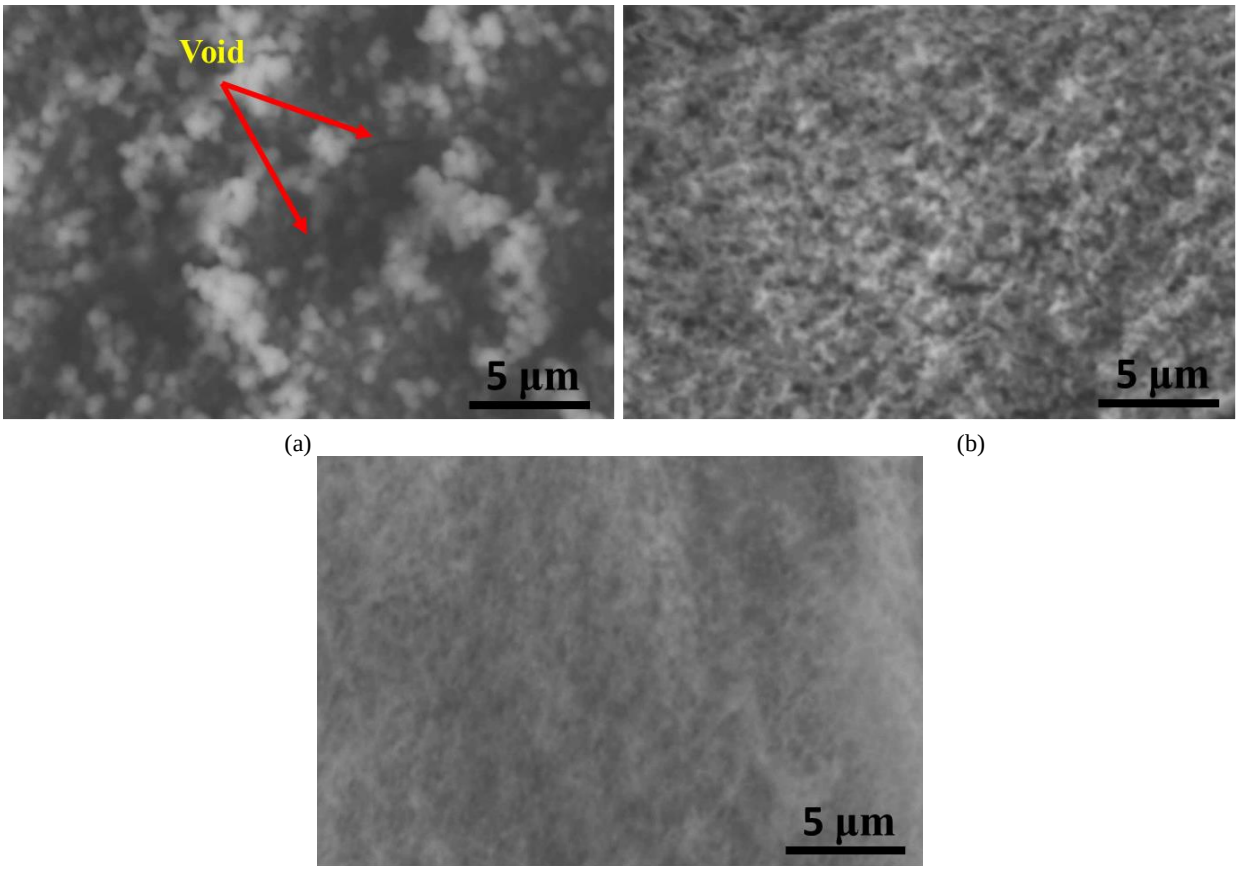

(a) (b)

(c)

Figure 2. SEM image of magnesium WE 43 coated HAp with PAA (a) 0.15 PAA, (b) 0.3 PAA, and (c) 0.5 PAA (w/v)

When a scratch occurs, the electrolyte gets into the coating and penetrates the green layer and magnesium substrate below, which starts localized corrosion. This makes $Mg(OH)_2$ and raises the pH in the area that was impacted. The alkaline environment speeds up the precipitation of phosphate and allows the coating and immersion medium absorb Ca^{2+} ions. This leads to the formation and growth of calcium phosphate phases. These deposits slowly turn into hydroxyapatite (HAp), which fills in and seals the scratched region. The created layer effectively blocks aggressive ion movement and stops more electrolyte from getting in, which reduces localized corrosion and makes self-healing capabilities easier to achieve [21]-[22].

After 24 hours of immersion (Figs. 3(b), 3(e), and 3(h)), the coatings show clear differences. The 0.15 PAA sample (Fig. 3(b)) displays clear microcracks and localized corrosion products developing along the scratch lines. This suggests that the coating wasn't able to keep the electrolyte from getting through. The 0.3 PAA coating (Fig. 3(e)) produces a denser network of microcracks, although the surface is still mostly intact. The 0.5 PAA coating (Fig. 3(h)), on the other hand, is mostly intact, showing only minor surface fractures and an absence of major pitting. This implies that the increased concentration of PAA made the coating more compact and less susceptible to damage in specific areas. After 48 hours of immersion (Figs. 3(c), 3(f), and 3(i)), the lower-PAA coatings show greater signs of deterioration. The 0.15 PAA sample (Fig. 3(c)) shows a lot of delamination and deep fissures, which means that the magnesium substrate

underneath is corroding a lot. The 0.3 PAA coating (Fig. 3(f)) is partially coming off and collecting corrosion products, which means it offers modest protection. The 0.5 PAA coating (Fig. 3(i)), on the other hand, keeps a smooth and continuous surface with only a few signs of corrosion. The fine, round HAp crystals and increased polymer content probably made the microstructure more compact, which stopped ions from moving around and protected the substrate while it was in hanks'solution for a long time [23].

Overall, the microstructural evolution during immersion demonstrates that increasing PAA concentration improves the coating's ability to withstand corrosion and maintain surface integrity after mechanical damage. Among the tested compositions, the coating prepared with 0.5% PAA exhibits the best corrosion resistance and healing behavior, characterized by minimal crack propagation and the presence of a stable protective layer after 48 h of immersion [24]

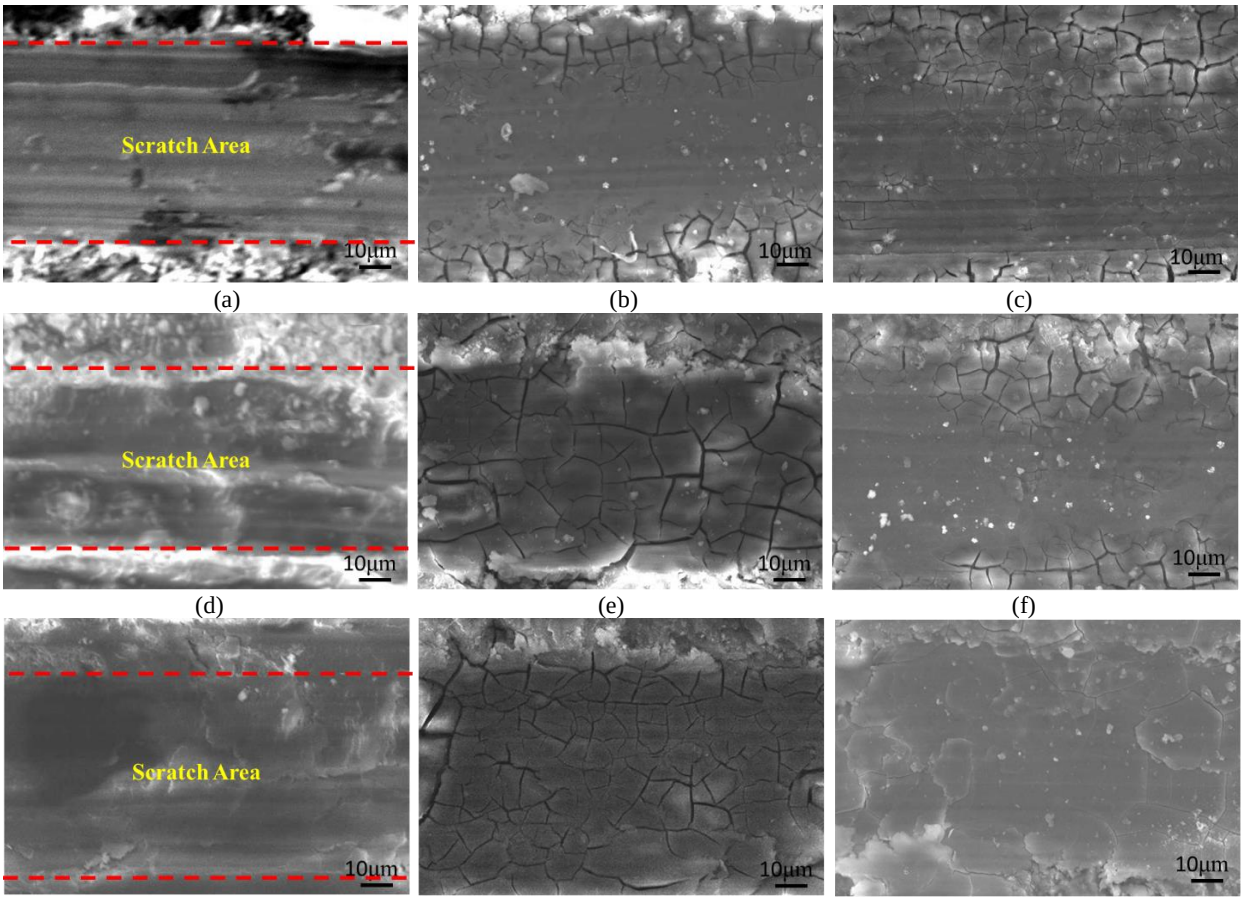

Figure 3. SEM image of the coating's surface morphology in the scratch-immersion test on the HAp/PAA-coated WE43 alloy: (a) 0.15 PAA just after scratching, (b) 0.15 PAA after 24 h, and (c) 0.15 PAA after 48 h, (d) 0.3 PAA just after scratching, (e) 0.3 PAA after 24 h, and (f) 0.3 PAA after 48 h, (g) 0.5 PAA just after scratching, (h) 0.5 PAA after 24 h, and (i) 0.5 PAA after 48 h of immersion in Hanks' solution at 37 °C

Figure 4 shows the electrochemical impedance spectra of the HAp/PAA coatings on WE43 alloy with varied PAA concentrations (0.15%, 0.3%, and 0.5% w/v). The spectra were taken at different periods of immersion (before scratching, after scratching, and after 24 and 48 hours of immersion in Hank's solution). The Nyquist plots (Figs. 4(a), 4(d), and 4(g)), Bode modulus plots (Figs 4(b), 4(e), and 4(h)), and Bode phase plots (Figs 4(c), 4(f), and 4(i)) show how the coating's electrochemical response and protective stability change over time while it is in Hank's solution.

For the coating with 0.15% PAA (Figs 4(a)-4(c)), the Nyquist diagram displays a small capacitive semicircle with a noticeable reduction in diameter after scratching and immersion. The impedance modulus at low frequencies ($|Z|_{0.01Hz}$) decreases sharply after 24 h, indicating the rapid loss of protective properties. The Bode phase plot shows a single relaxation time that shifts toward lower frequencies, confirming that corrosion processes dominate after electrolyte penetration. These results are consistent with the SEM observations (Figs. 3(a)-3(c)), where extensive cracking and delamination occurred, suggesting that the porous and inhomogeneous coating formed at low PAA concentration provides insufficient corrosion protection [25].

For 0.3% PAA (Figs. 4(d)-4(f)), the Nyquist plots show bigger capacitive loops and higher impedance values than for 0.15% PAA. This means that the barrier works better. The Bode phase diagram shows two-time constants, one for the outside porous HAp/PAA layer and one for the inner corrosion product layer. After 48 hours of immersion, though, there is a slight drop in impedance, which suggests that the coating is breaking down in some way. The electrochemical trends are in line with the SEM results (Figs. 3(d)-3(f)), which reveal that the 0.3% PAA coating keeps its structure better than the 0.15% PAA coating but develops microcracks and localized corrosion characteristics with time.

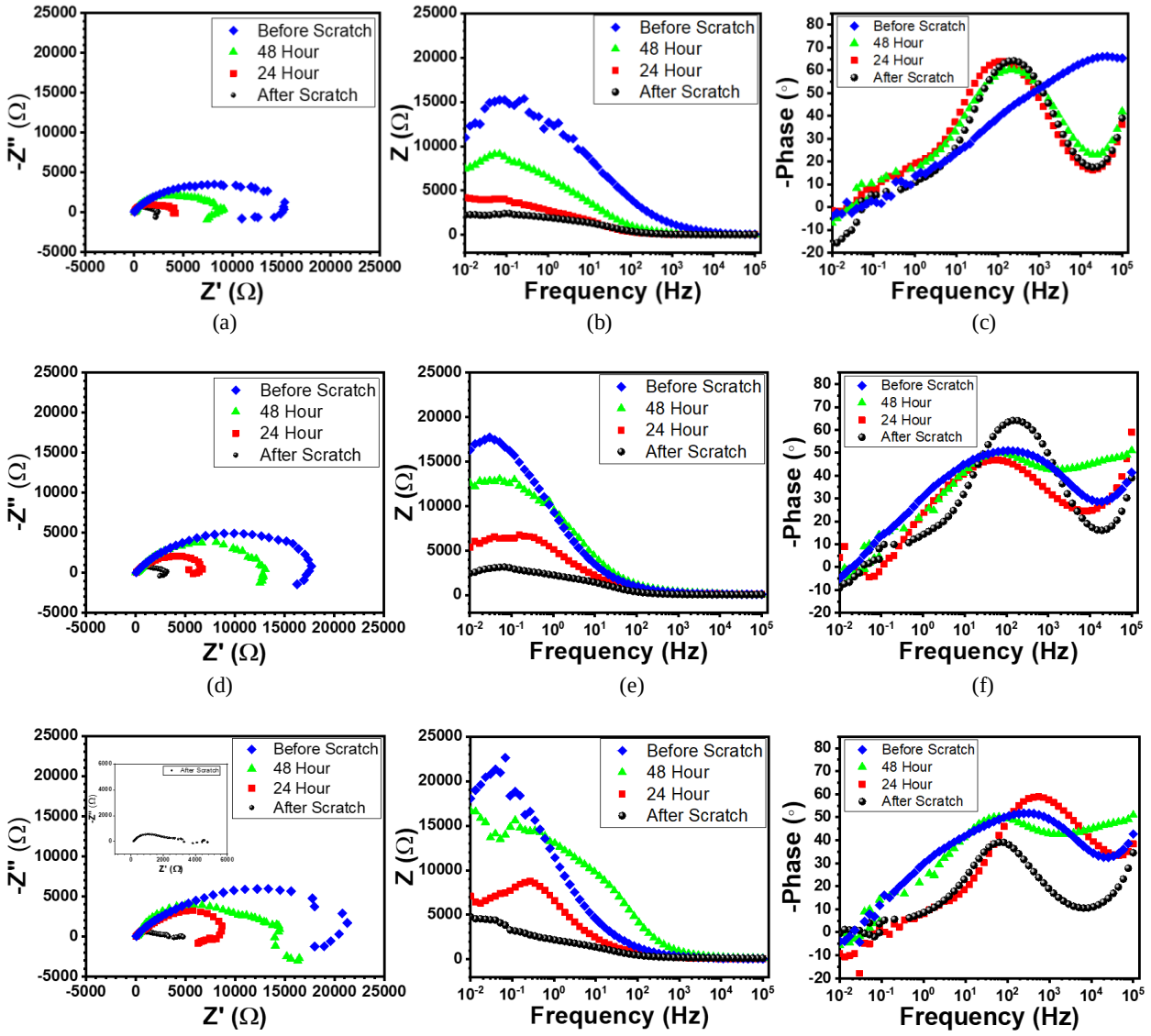

Figure 4. Electrochemical impedance spectra of the scratch-immersion test on the HAp/PAA-coated WE43 alloy: (a) Nyquist plot of 0.15 PAA, (b) Bode Modulus plot of 0.15 PAA (c) Bode Phase plot of 0.15 PAA, (d) Nyquist plot of 0.3 PAA, (e) Bode Modulus plot of 0.3 PAA (f) Bode Phase plot of 0.3 PAA, (g) Nyquist plot of 0.5 PAA, (h) Bode Modulus plot of 0.5 PAA (i) Bode Phase plot of 0.5 PAA

The coating with 0.5% PAA (Figs. 4(g)-4(i)) demonstrates the highest impedance values and the largest Nyquist semicircle radius, even after 48 h of immersion. The Bode modulus remains above 10^4 Ω·cm² at low frequencies, and the phase angle approaches −70°, indicating a highly capacitive and protective surface. The two distinct time constants persist, suggesting stable dual-layer protection consisting of a compact outer HAp/PAA layer and a corrosion-resistant interface layer beneath it. Only a minor reduction in impedance is observed after scratching, demonstrating that the coating effectively limits electrolyte access and exhibits partial self-healing capability. These findings are consistent with SEM observations (Figs. 3(g)-3(i)), where the 0.5% PAA coating retained a smooth, dense morphology with minimal cracking after

prolonged immersion. The presence of spherical and uniformly distributed HAp crystals, as seen in Fig. 2(c), contributes to the formation of a tightly packed microstructure that enhances barrier resistance and adhesion [26].

In general, the EIS results back up what the SEM investigations found about how the shapes changed. The corrosion resistance and coating stability of the HAp/PAA composite layers become a lot better when the PAA concentration Figure 5 presents equivalent circuits calculated from the Nyquist plot characterization results of the scratch-immersion test. The variations in the equivalent circuit models derived from each PAA composition and immersion condition illustrate the dynamic and intricate characteristics of the HAp/PAA composite layer system throughout the degradation process. The model's inconsistency or randomness arises not from measurement errors, but from actual alterations in the structure of the metal layers and interfaces during the scratch-immersion test. In the layer with low PAA content (0.15%), the porous structure yields a straightforward electrochemical response characterized by one to two time constants. In contrast, at 0.3% PAA, the system exhibits goes up. The 0.5% PAA coating has the most stable electrochemical behavior of all the formulations. Even after mechanical damage or prolonged immersion in water, it maintains high impedance values and phase stability. The compact, spherical HAp shape and the thick PAA polymer matrix work together to stop corrosion reactions and keep the metal-coating contact stable, which is why the formulation works so well [27].

increased complexity due to the development of a double protective layer and regenerative reactions in the scratched region. At 0.5% PAA, the thicker and more hydrophilic layer is capable of absorbing water, which facilitates the formation of ionic diffusion pathways and results in an inductive response at low frequencies. This difference shows that the protective mechanisms in each case are not static; they change over time and are affected by the layer's organic-inorganic composition. The variety of equivalent circuit models reinforces the understanding that corrosion and film recovery processes occur progressively and adaptively in response to environmental conditions.

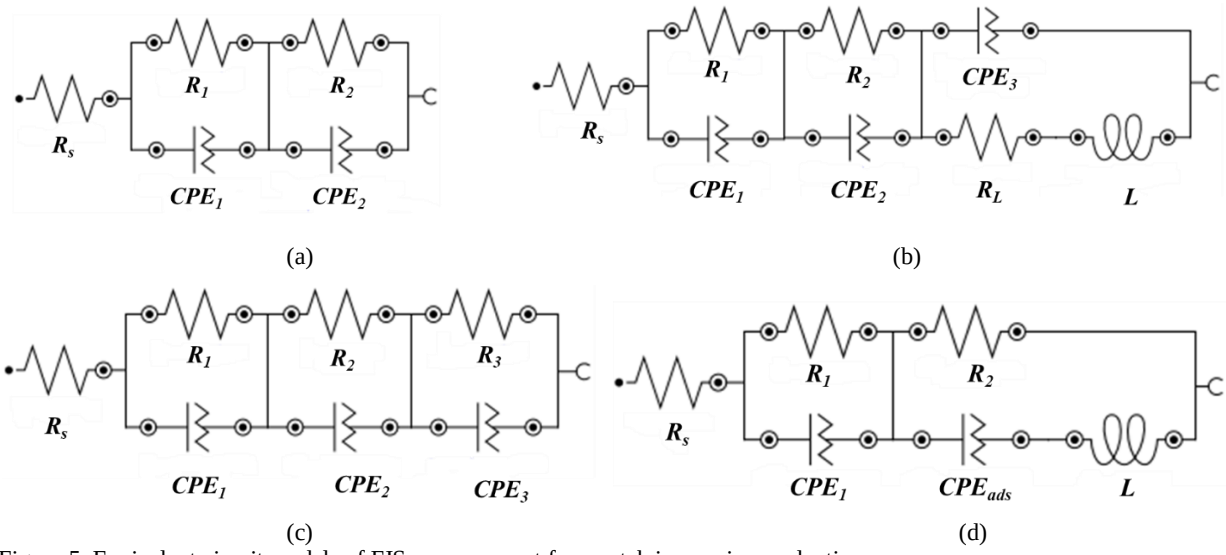

Figure 5. Equivalent circuit models of EIS measurement for scratch immersion evaluation

4. CONCLUSION

The hydrothermally synthesized hydroxyapatite/polyacrylic acid (HAp/PAA) composite coating was proven to enhance corrosion resistance and exhibit effective self-healing behavior on WE43 magnesium alloy. Variations in PAA concentration play a crucial role in determining the microstructure, density, and stability of the layer. The increased PAA content results in better dispersion of HAp crystals and promotes the formation of a dense and homogeneous microstructure, thereby strengthening the interface between the layers and the substrate. FTIR analysis indicates that HAp and PAA physically interact through hydrogen bonds without forming new compounds, while SEM results show that the layer with 0.5% PAA can maintain its surface integrity even after mechanical damage. During the soaking process in Hank's solution, the PAA phase acts as an ionic reservoir, facilitating the migration of Ca^{2+} and PO_4^{3-} ions toward the

scratched areas, thus leading to the re-formation of Ca–P compounds or HAp crystals that seal microcracks and restore the protective layer's function. The EIS test results reinforce these findings by showing that the 0.5% PAA layer has the highest impedance value and consistent phase stability after 48 hours of immersion, indicating superior corrosion resistance and self-healing ability. Thus, the HAp/PAA composite layer with an optimal composition of 0.5% PAA can be said to have the most compact, stable, and adaptive characteristics to the corrosive environment, making it highly promising as a smart and bioactive coating system for next-generation biodegradable magnesium implant applications.

ACKNOWLEDGEMENT

This work was supported by Hibah Riset UI, PUTI Pasca Sarjana Research Project, and Research Organization for Nanotechnology and Materials-National Research and Innovation Agency (BRIN) grant with the number 3/III.10/HK/2023. This work was also part of the Degree by Research Program of the National Research and Innovation Agency (BRIN).

REFERENCES

[1] N. A. Johari, J. Alias, A. Zanurin, N. S. Mohamed, N. A. Alang, and M. Z. M. Zain, "Recent progress of self-healing coatings for magnesium alloys protection," *J. Coatings Technol. Res.*, vol. 19, no. 3, pp. 757-774, 2022. DOI: 10.1007/s11998-021-00599-2.

[2] G. Cui, Z. Bi, S. Wang, J. Liu, X. Xing, Z. Li, and B. Wang, "A comprehensive review on smart anti-corrosive coatings," *Prog. Org. Coatings*, vol. 148, no. 66, p. 105821, 2020. DOI: 10.1016/j.porgcoat.2020.105821.

[3] B. Li, Z. Zhang, T. Liu, Z. Qiu, Y. Su, J. Zhang, C. Lin, and L. Wang, "Recent progress in functionalized coatings for corrosion protection of magnesium alloys: A review," *Materials (Basel).*, vol. 15, no. 11, 2022. DOI: 10.3390/ma15113912.

[4] G. S. Pereira, G. Y. Koga, J. A. Avila, I. M. Bittencourt, F. Fernandez, M. H. Miyazaki, W. J. Botta, and W. W. Bose Filho, "Corrosion resistance of WE43 Mg alloy in sodium chloride solution," *Mater. Chem. Phys.*, vol. 272, 2021. DOI: 10.1016/j.matchemphys.2021.124930.

[5] S. H. Byun, H. K. Lim, K. H. Cheon, S. M. Lee, H. E. Kim, and J. H. Lee, "Biodegradable magnesium alloy (WE43) in bone-fixation plate and screw," *J. Biomed. Mater. Res.-Part B Appl. Biomater.*, vol. 108, no. 6, pp. 2505-2512, 2020. DOI: 10.1002/jbm.b.34582.

[6] C. H. Shih, C. Y. Huang, T. H. Hsiao, and C. S. Lin, "The effect of the secondary phases on the corrosion of AZ31B and WE43-T5 Mg alloys," *Corros. Sci.*, vol. 211, p. 110920, 2023. DOI: 10.1016/j.corsci.2022.110920.

[7] V. K. Manivasagam, M. Sankar, C. B. Garcia, J. Vishnu, K. Chatterjee, S. Suwas, G. Manivasagam, and T. J. Webster, "Surface-modified WE43 magnesium alloys for reduced degradation and superior biocompatibility," *Vitr. Model.*, vol. 1, no. 3, pp. 273-288, 2022. DOI: 10.1007/s44164-022-00016-x.

[8] H. Zhang, C. Zhang, and S. D. Jiang, "Morphology evolution of hydroxyapatite: Synergistic effects and water treatment application," *Mater. Lett.*, vol. 341, p. 134288, 2023. DOI: 10.1016/j.matlet.2023.134288.

[9] S. Wen, X. Liu, J. Ding, Y. Liu, Z. Lan, Z. Zhang, and G. Chen, "Hydrothermal synthesis of hydroxyapatite coating on the surface of medical magnesium alloy and its corrosion resistance," *Prog. Nat. Sci. Mater. Int.*, vol. 31, no. 2, pp. 324-333, 2021. DOI: 10.1016/j.pnsc.2020.12.013.

[10] G. Wang, Y. Wei, J. Hong, and J. Lv, "Spray-synthesized organic composite/hydroxyapatite coating on magnesium alloys with enhanced corrosion resistance," *Front. Chem.*, vol. 13, pp. 1-11, 2025. DOI: 10.3389/fchem.2025.1566676.

[11] S. Roshan, H. E. Mohammadloo, A. A. Sarabi, and M. Afshari, "Biocompatible hybrid chitosan/hydroxyapatite coating applied on the AZ31 Mg alloy substrate : In-vitro corrosion, surface and structure studies," *Mater. Today Commun.*, vol. 30, p. 103153, 2022. DOI: 10.1016/j.mtcomm.2022.103153.

[12] H. Arkaban, M. Barani, M. R. Akbarizadeh, N. P. S. Chauhan, S. Jadoun, M. D. & Soltani, and P. Zarrintaj, "Polyacrylic acid nanoplatforms: antimicrobial, tissue engineering, and cancer theranostic applications," *Polymers*, vol. 14, no. 1259. 2022. DOI: 10.3390/polym14061259.

[13] P. Zheng, J. Deng, L. Jiang, N. Ni, X. Huang, Z. Zhao, X. Hu, X. Cen, J. Chen,

and R. Wang, "Polyacrylic acid-reinforced organic-inorganic composite bone adhesives with enhanced mechanical properties and controlled degradability," *J. Mater. Chem. B*, vol. 12, no. 34, pp. 8321–8334, 2024. DOI: 10.1039/d4tb00857j.

[14] M. E. Diken, S. Doğan, M. Doğan, and Y. Turhan, "Synthesis and characterization of poly(acrylic acid)/nanohydroxyapatite nanocomposite hydrogels and evaluation of its antibacterial, bio- and hemo-compatibility characteristics," *Int. J. Polym. Mater. Polym. Biomater.*, vol. 71, no. 18, pp. 1425-1436, 2022. DOI: 10.1080/00914037.2021.1981320.

[15] J. Yang, Y. Zhao, J. Dai, L. Han, and Q. Dong, "Surface & coatings technology fabrication and growth mechanism of multilayered hydroxyapatite/organic composite coatings on the WE43 magnesium alloy," *Surf. Coat. Technol.*, vol. 452, p. 129125, 2023. DOI: 10.1016/j.surfcoat.2022.129125.

[16] Z. Zhang, Y. Chen, D. Mandler, and M. Shenker, "Transport of hydroxyapatite nanoparticles coated with polyacrylic acid under unsaturated water flow in soil columns," *Soil Sci. Plant Nutr.*, vol. 69, no. 2, pp. 124-136, 2023. DOI: 10.1080/00380768.2022.2163457.

[17] S. Sözügeçer and N. P. Bayramgil, "Preparation and characterization of polyacrylic acid-hydroxyapatite nanocomposite by microwave-assisted synthesis method," *Heliyon*, vol. 7, no. 6, p. e07226, 2021. DOI: 10.1016/j.heliyon.2021.e07226.

[18] X. J. Ji, L. Gao, J. C. Liu, J. Wang, Q. Cheng, J. P. Li, S. Q. Li, K. Q. Zhi, R. C. Zeng, and Z. L. Wang, "Corrosion resistance and antibacterial properties of hydroxyapatite coating induced by gentamicin-loaded polymeric multilayers on magnesium alloys," *Colloids Surfaces B Biointerfaces*, vol. 179, pp. 429-436, 2019. DOI: 10.1016/j.colsurfb.2019.04.029.

[19] J. Chen, Y. Yang, I. P. Etim, L. Tan, K. Yang, R. D. K. Misra, J. Wang, and X. Su, "Recent advances on development of hydroxyapatite coating on biodegradable magnesium alloys: A review," *Materials (Basel).*, vol. 14, no. 19, pp. 1-15, 2021. DOI: 10.3390/ma14195550.

[20] K. P. P. Kumar, K. R. C. S. Raju, and R. Subasri, "Self-healing corrosion protection coatings obtained by anodization and sol–gel process on Mg AZ31 alloy," *Prot. Met. Phys. Chem. Surfaces*, vol. 58, no. 4, pp. 856-871, 2022. DOI: 10.1134/S2070205122040116.

[21] G. S. Hikku, C. Arthi, R. B. J. Robert, K. Jeyasubramanian, and R. Murugesan, "Calcium phosphate conversion technique : A versatile route to develop corrosion-resistant hydroxyapatite coating over Mg / Mg alloys based implants," *J. Magnes. Alloy.*, vol. 10, no. 7, pp. 1821-1845, 2022. DOI: 10.1016/j.jma.2022.06.005.

[22] Y. Zhao, J. Bai, F. Xue, R. Zeng, G. Wang, P. K. Chu, and C. Chu, "Smart materials in manufacturing smart self-healing coatings on biomedical magnesium alloys : A review," *Smart Mater. Manuf.*, vol. 1, no. 2, p. 100022, 2023. DOI: 10.1016/j.smmf.2023.100022.

[23] J. K. E. Tan, N. Birbilis, S. Choudhary, S. Thomas, and P. Balan, "Corrosion protection enhancement of Mg alloy WE43 by in-situ synthesis of MgFe LDH/citric acid composite coating intercalated with 8HQ," *Corros. Sci.*, vol. 205, p. 110444, 2022. DOI: 10.1016/j.corsci.2022.110444.

[24] M. Ostapiuk, J. Bieniaś, M. V. Loureiro, and A. C. Marques, "The effect of self-healing on the corrosion resistance of a Mg alloy promoted by isocyanate microcapsules of polyurethane/polyurea shell," *J. Mater. Eng. Perform.*, vol. 6, 2025. DOI: 10.1007/s11665-025-11760-y.

[25] A. S. Gnedenkov, V. S. Filonina, S. L. Sinebryukhov, and S. V. Gnedenkov, "A superior corrosion protection of Mg alloy via smart nontoxic hybrid inhibitor-containing coatings," *Molecules*, vol. 28, no. 6, 2023. DOI: 10.3390/molecules28062538.

[26] N. S. Grewal, U. Batra, K. Kumar, and A. Mahapatro, "Novel PA encapsulated PCL hybrid coating for corrosion inhibition of biodegradable Mg alloys: A triple-triggered self-healing response for synergistic multiple protection," *J. Magnes. Alloy.*, vol. 11, no. 4, pp. 1440-1460, 2023. DOI: 10.1016/j.jma.2023.01.019.

[27] Z. Shi, F. Yang, Y. Hu, Q. Pang, L. Shi, T. Du, Y. Cao, B. Song, X. Yu, Z. Cao, Z.

Ye, C. Liu, R. Yu, X. Chen, Y. Zhu, and Q. Pang, “An oxidized dextran-composite self-healing coated magnesium scaffold reduces apoptosis to induce bone regeneration,” *Carbohydr. Polym.*, vol. 327, p. 121666, 2024. DOI: 10.1016/j.carbpol.2023.121666.

Metalurgi (2024) 3: 117-128

METALURGI
Majalah Ilmu dan Teknologi
p-ISSN 0126-3188 | e-ISSN 2443-3926
ejurnalmaterialmetalurgi.lipi.go.id

EFFECT OF SURFACE ROUGHNESS ON ADHESION STRENGTH AND CORROSION RESISTANCE OF SILICA-EPOXY COMPOSITE COATED LOW CARBON STEEL

Rizal Tresna[a,*], Keanu Rafi Amrullah[a], Aqil Rahmatullah[a], Eni Febriana[b], Latifa Hanum Lalasari[b], Rini Riastuti[a]

[a]Department of Metallurgical and Materials Engineering, University of Indonesia
Kampus UI, Kukusan, Depok, Indonesia 16424
[b]Research Center for Metallurgy, National Research and Innovation Agency (BRIN)
B.J. Habibie Sains and Technology Area, Banten, Indonesia 15314
*E-mail: Rizal.tresna@yahoo.com

Received: 22-10-2025, Revised: 29-12-2025, Accepted: 31-12-2025

Abstract

Low-carbon steel is widely used in various industries but is susceptible to corrosion in aggressive environments, prompting this study on an epoxy-silica composite coating with variations in silica concentration (0-5 wt.%), sonication dispersion, and surface preparation (abrasive blast cleaning and power tool cleaning); the results showed that abrasive blast cleaning produced a surface roughness of 79 µm and superior adhesion strength (10.48 MPa) compared to power tool cleaning, with a perfect 5A rating in the x-cut tape test for all silica concentrations, while the highest adhesion strength of 14.33 MPa was achieved at 3 wt.% silica, and coating durability tests revealed the best performance exhibiting minimal corrosion propagation of only 0.55 mm after 72 hours at 5 wt.% silica in scratch tests using abrasive blast cleaning, underscoring the significant influence of surface preparation method on coating performance.

Keywords: *Epoxy-silica composite, corrosion resistance, surface preparation, adhesion strength, sonication*

1. INTRODUCTION

Low-carbon steel, often referred to as mild steel, constitutes the backbone of global industrial development, with annual production exceeding 1.8 billion tons [1]. Its unparalleled dominance in construction, automotive, and marine applications is attributed to a favorable combination of economical cost, ease of fabrication, and adequate mechanical strength [2]. Despite these advantages, a critical Achilles' heel remains: its pronounced susceptibility to corrosion, especially in aggressive environments such as seawater rich in chloride ions [2]. This degradation not only drastically shortens the material's service life but also elevates the risk of catastrophic structural failures, necessitating the development of robust, effective, and sustainable protective solutions.

Organic polymeric coatings, particularly those based on epoxy resins, are widely employed as primary protective barriers. Epoxy is favored for its strong adhesion, chemical resistance, and dimensional stability [3]. To further improve performance, composite coatings incorporating functional fillers such as silica (SiO_2) have attracted considerable interest. In this study, high-purity precipitated silica derived from quartz sand sourced from Kendawangan, West Kalimantan, is used. The silica was obtained through a series of steps, including roasting, hot-water dissolution, leaching, precipitation, and repeated hydrochloric acid washing. This silica composition test result

DOI: 10.55981/metalurgi.2024.777

Metalurgi is Sinta 2 Journal (https://sinta.kemdikbud.go.id/journals/profile/3708) accredited by Ministry of Education, Culture, Research, and Technology, Republic Indonesia

confirmed that precipitated silica achieves a purity level of 99.99%, as can be seen in Table 1[4].

The incorporation of such silica into the epoxy matrix enhances barrier properties by creating a tortuous path that hinders the penetration of water, oxygen, and corrosive ions. Additionally, silica serves as a reinforcing phase, improving mechanical properties such as abrasion resistance and hardness [5].

Table 1. The chemical composition of silica precipitate

Compound	Content (wt.%)
SiO_2	99.99566
Al_2O_3	0.00088
Fe_2O_3	0.00034
TiO_2	0.00112
CaO	0.00012
MgO	0.00024
NaO	0.00088
LOI	0.00077

The performance of silica-epoxy composite coatings is highly dependent on two crucial factors: the uniformity of filler dispersion and the quality of substrate preparation. Silica particles, particularly at nano- and micro-scales, tend to agglomerate due to strong van der Waals forces, leading to defects that can become pathways for corrosive agents and points of stress concentration. Therefore, achieving a homogeneous dispersion is essential [6]. While various mechanical mixing methods are available, ultrasonication has been identified as a highly effective technique. It uses high-frequency sound waves to generate acoustic cavitation, producing intense local shear forces that break apart agglomerates and ensure even distribution within the epoxy matrix [7].

Equally important is the preparation of the steel substrate, as coating performance is fundamentally reliant on adhesion. Surface treatment methods such as abrasive blast cleaning and power tool cleaning are designed to remove contaminants like rust, mill scale, and old paint, while also imparting a specific surface roughness. Abrasive blast cleaning, which involves propelling abrasive media at high speed, typically produces a higher and more consistent surface profile compared to power tool techniques such as grinding or wire brushing [8]. The resulting surface topography enhances mechanical interlocking between the coating and substrate, significantly improving adhesion and long-term durability [9].

While the individual effects of silica reinforcement and surface preparation on coating performance have been examined separately, their combined influence, particularly the interaction between surface roughness and dispersion quality in relation to adhesion and corrosion resistance, remains insufficiently explored. This represents a significant research gap regarding the synergistic relationships among these critical parameters [10].

The present study aims to address this gap through a comprehensive investigation of epoxy-silica composite coatings applied to low-carbon steel substrates. The research systematically examines three key variables: silica concentration was varied from 0 to 5 wt.% to determine optimal loading levels; ultrasonication was employed as the dispersion method to ensure homogeneous distribution within the epoxy matrix; and a direct comparison was made between abrasive blast cleaning and power tool cleaning to evaluate their respective effects on surface roughness.

Through this integrated approach, the study seeks to identify the optimal conditions that synergistically enhance coating performance. The findings are expected to provide valuable practical insights for industrial applications in corrosive environments, particularly where both mechanical durability and long-term corrosion protection are essential requirements.

2. MATERIALS AND METHODS

In this experiment, a surface-tolerant epoxy resin was used as the primary matrix for the coating. The epoxy composite was modified by incorporating microsilica filler at a 99 wt% from Kendawangan quartz sand. To ensure homogeneous dispersion and deagglomeration of the filler within the epoxy matrix, the mixture was subjected to a sonication process. The resulting epoxy composite coating was then applied to a substrate of low-carbon steel, specifically AISI 1008 series, to evaluate its performance.

2.1 Materials

The coating was formulated using a commercial surface-tolerant epoxy system, specifically International Paint's RE 1553 (Part A) and RE 6529 (Part B). This two-component system was prepared by first mixing the base resin with a dedicated hardener at a fixed ratio of 6:1 (resin to hardener). To achieve an optimal application viscosity, the mixture was diluted with thinner, which was added at a concentration of 20% by volume of the total solution. Microsilica filler was subsequently incorporated into this epoxy blend to form a composite. The specific weight percentage (wt.%) of the microsilica filler used in this study is provided in Table 1.

The substrate selected for this investigation was low-carbon steel, conforming to the AISI 1008 series specification. The precise elemental

composition of this steel substrate was quantitatively ascertained using OES (optical emission spectroscopy) to ensure material consistency and for subsequent corrosion performance analysis; the full OES results are detailed in Table 2.

The formulated epoxy composite coating was then uniformly applied to the prepared surface of this AISI 1008 steel substrate to evaluate its protective properties.

Table 2. Chemical composition of carbon steel using OES

Element	Content (wt.%)
Fe	99.54
C	0.052
Mn	0.187
N	0.048
Al	0.028
Fe	99.54
Cu	0.022
Te	0.035
Ni	0.015
Cr	0.011
W	0.013
V	0.0056
Co	0.0081
Sb	0.0077
Nb	0.0068
Bi	0.0035

The adhesive strength of the applied epoxy composite coating was quantitatively evaluated using a direct pull-off test according to a relevant standard (e.g., ASTM D4541 or ISO 4624). For this purpose, a dolly was affixed to the coated surface using a high-strength epoxy adhesive (araldite) and subjected to a perpendicular tensile force until failure.

Qualitative assessment of adhesion was further conducted via an X-cut tape test (e.g., ASTM D3359 or ISO 2409), utilizing a precision cutter and a specified pressure-sensitive tape to determine the coating's resistance to detachment from the substrate.

Furthermore, the coating's corrosion resistance and the durability of its adhesion in a hostile environment were investigated through a salt spray test (e.g., ASTM B117 or ISO 9227). A 5 wt% sodium chloride (NaCl) solution was prepared by dissolving 5 g of NaCl in 1000 mL of deionized water and was used to maintain a continuous corrosive fog within the testing chamber.

2.2 Methods

This study was conducted using a low-carbon steel plate as the primary substrate, prepared in three distinct dimensions: 10×10×3 mm for salt spray and adhesion testing and 1.5×1.5×3 mm for SEM-EDX characterization. Surface preparation was performed via two methods: power tool cleaning with a steel wire brush cup and abrasive blast cleaning using garnet abrasive. The resulting surface profile was measured using a Testex tape and an analog snap gauge to ensure preparation consistency.

An epoxy-silica composite coating was formulated through a sonication process to achieve optimal particle dispersion, followed by the addition of a hardener agent. The physical characteristics of the coating solution, including density and flow rate, were measured using a pycnometer and a flow cup viscometer.

Ambient conditions during coating application were monitored with a sling psychrometer, and the coating thickness was controlled using a manual film applicator and verified with a PosiTector 6000 coating thickness gauge.

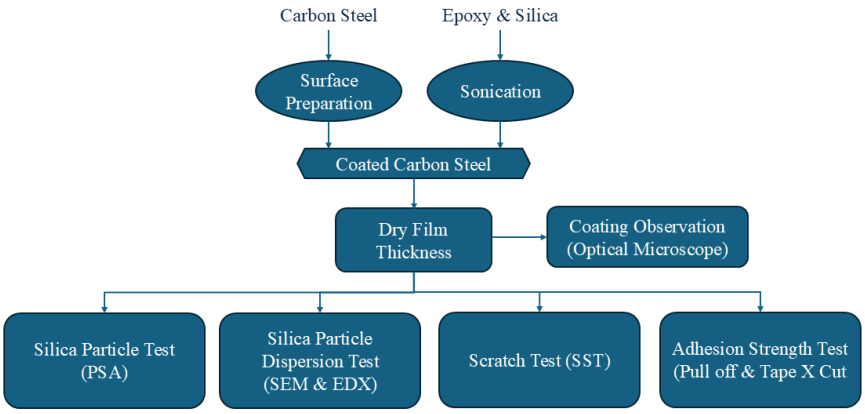

Figure 1. Research flowchart

2.3 Characterization

The characterization process in this study focused on analyzing the dispersion and

distribution of silica within the epoxy matrix following the sonication process.

The particle size distribution of the silica within the epoxy composite was determined using a laser scattering particle size distribution analyzer (Horiba LA-960). The epoxy composite in liquid form was placed in a sample cell for characterization to evaluate the effectiveness of the sonication process in deagglomerating the silica particles.

The microstructure and elemental composition of the epoxy-silica composite were analyzed using a scanning electron microscope (JEOL JSM-IT200) equipped with an energy dispersive X-ray spectroscopy system. This technique provided high-resolution images of the surface morphology to visually assess the dispersion homogeneity of the silica filler. The integrated EDX system was used to perform quantitative elemental analysis and to map the distribution of silicon and oxygen, confirming the uniform distribution of silica particles within the epoxy polymer matrix.

3. RESULTS AND DISCUSSION

3.1 Visual Surface Observation

Visual assessment against SSPC-VIS 1 and SSPC-VIS 3 standards confirmed that both abrasive blast cleaning and power tool cleaning significantly improved the surface condition from an initial Rust Grade C.

Abrasive blast cleaning effectively produced a surface meeting the CSP-5 (white metal) standard. The process successfully removed all visible mill scale, rust, and old coatings, exposing a clean, profiled metallic substrate ideal for coating adhesion. This high level of cleanliness is attributed to the high kinetic energy of the abrasive particles.

In contrast, power tool cleaning achieved the SSPC C SP3 PWB standard. While this method also removed the majority of contaminants, minimal residues remained on the surface. The results demonstrate that abrasive blast cleaning provides a superior surface profile and cleanliness compared to power tool cleaning, which leaves slight staining.

3.2 Surface Roughness After Preparation

Surface roughness measurements were conducted to verify the consistency of the surface profile generated by the two preparation methods. The results, presented in Table 3, show a distinct difference between the techniques.

Abrasive blast cleaning resulted in a high average surface roughness of 79.4 μm, with a standard deviation of approximately 6.4. This value falls within the typical range reported in the literature for garnet abrasives (40-125 μm) and is attributed to the aggressive impact of the abrasive particles on the steel substrate [11].

In contrast, power tool cleaning yielded a significantly lower average roughness of 27.2 μm with a standard deviation of about 3.4. The mechanical action of the steel wire brush cup not only cleans the surface but also has a polishing effect, resulting in a smoother final profile. This clear distinction highlights that the choice of preparation method directly determines the resultant surface topography, a critical factor for coating adhesion.

Table 3. Surface roughness value after surface preparation

Surface Preparation Method	Sample	Roughness (μm)	Average (μm)
Abrasive Blast Cleaning	1	75	79.4
	2	80	
	3	74	
	4	90	
	5	78	
Power Tool Cleaning	1	30	27.2
	2	29	
	3	23	
	4	30	
	5	24	

3.3 Silica Dispersion and Particle Size Analysis

SEM-EDX mapping analysis was performed to evaluate the dispersion quality of silica particles within the epoxy matrix across different filler loadings. Figures 2(a)-2(c) reveal that at low silica concentrations (0.3-0.75 wt.%), the filler particles were not uniformly distributed and tended to form agglomerates. The significant discrepancy between the added silica and the EDX-measured composition confirmed this poor dispersion, a phenomenon previously reported [12]. In contrast, Figures 3(a) and 3(b) show that samples with 1 and 3 wt.% loadings exhibited superior dispersion homogeneity, with EDX results closely matching the intended concentrations. However, at the highest loading of 5 wt.% (Fig. 3(c)), a degradation in dispersion quality was observed, indicated by a lower EDX-measured value, suggesting particle re-agglomeration due to dominant van der Waals forces and exceeding the optimal capacity for the sonication energy [13].

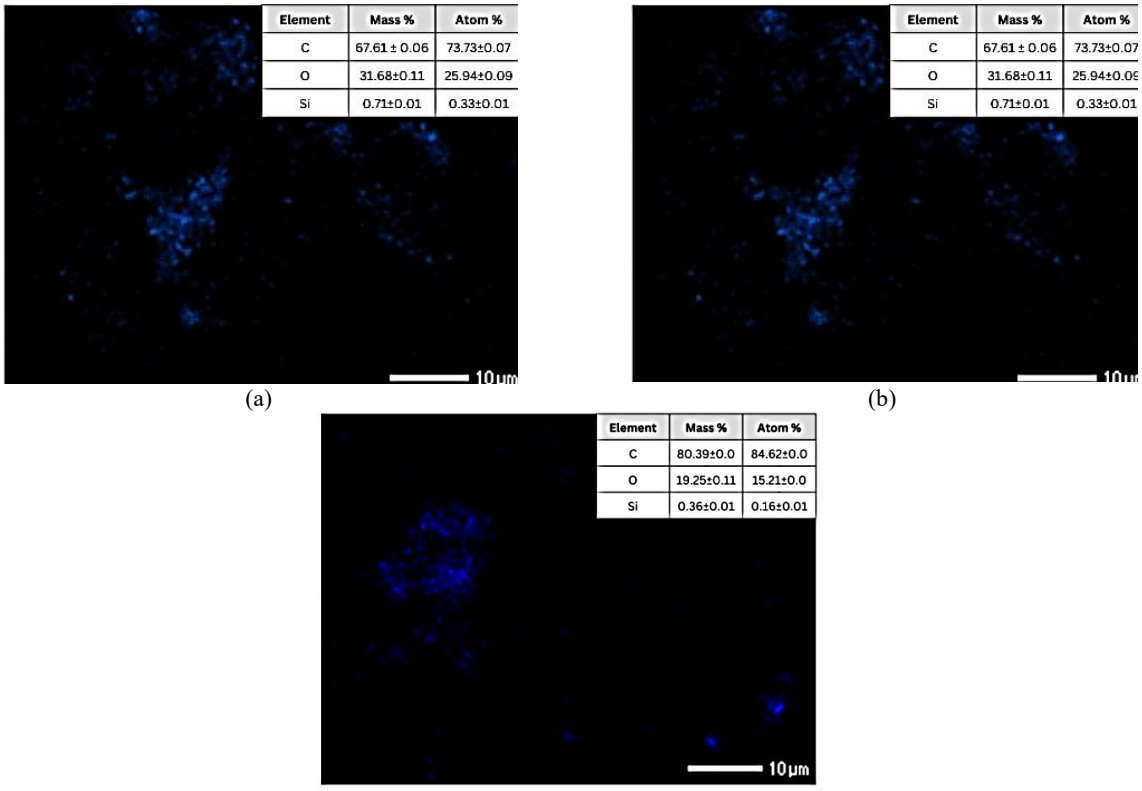

Figure 2. SEM and EDX analysis results with the addition of silica filler (wt.%): (a) 0.3, (b) 0.5, (c) 0.75

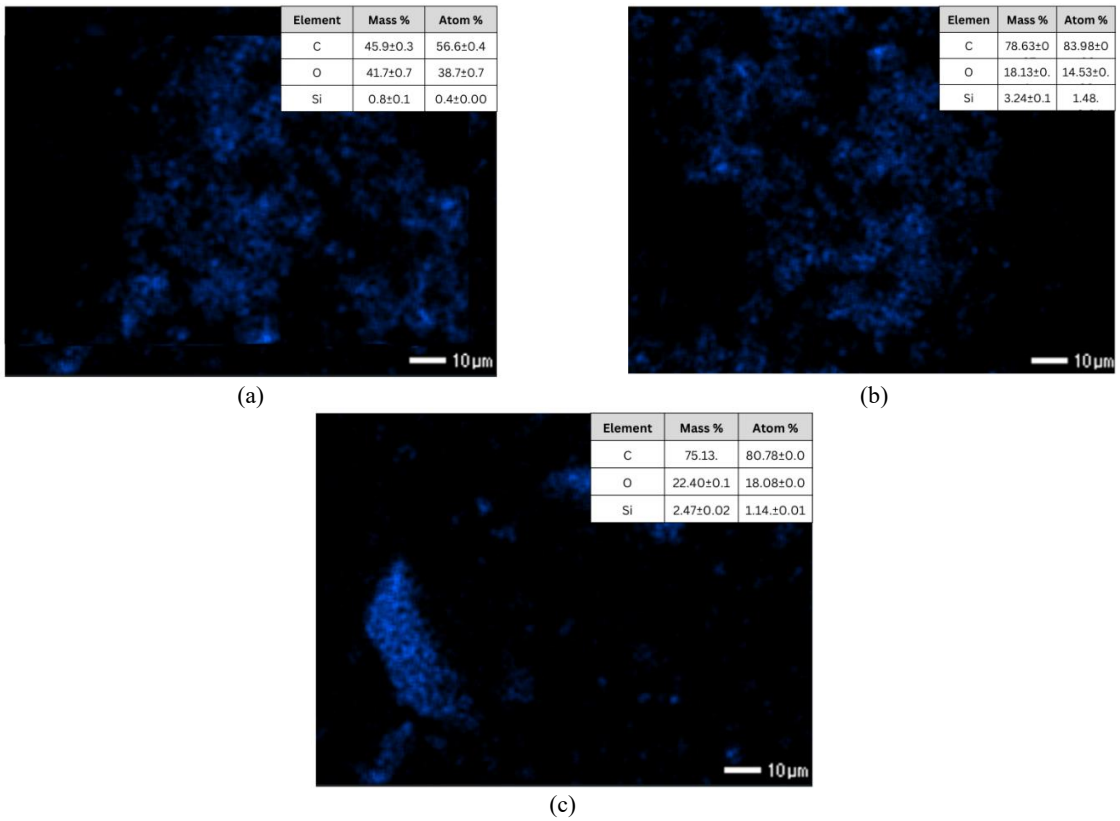

Figure 3. SEM and EDX analysis results with the addition of silica filler (wt.%): (a) 1, (b) 3, (c) 5

Particle size analysis revealed that sonication effectively reduced the initial silica size (~44 µm) to a range of 4.12-13.86 µm. The smallest average particle size (4.12 µm) was achieved at 1 wt.% loading, indicating optimal sonication efficiency where particle concentration allowed for effective energy transfer and deagglomeration without causing overcrowding. At lower concentrations (0.3-0.75 wt.%),

The larger particle sizes suggest suboptimal utilization of sonication energy due to an insufficient number of particle collisions [14].

Conversely, at higher loadings (3-5 wt.%), the observed increase in particle size is attributed to overloading, where particle screening effects and increased viscosity hinder effective sonication and promote re-agglomeration [13].

3.4 Flow Rate and Density of Epoxy Composite

The incorporation of silica filler significantly influenced the physical properties of the epoxy composite. As shown in Tables 4 and 5, increasing the silica content from 0 to 5 wt.% resulted in a consistent rise in density, from 1.091 g/mL to 1.1500 g/mL. This linear increase is attributed to the higher intrinsic density of silica particles compared to the epoxy matrix and their effective role in filling the free volume within the polymer structure [15].

Table 4. Density of epoxy composite solution

Silica Parameters (wt.%)	Density (g/mL)
0	1.091
0.30	1.096
0.5	1.099
0.75	1.008
1	1.1120
3	1.1372
5	1.1500

Concurrently, the flow rate of the composite decreased substantially from 0.36 cm/s for the neat epoxy to 0.07 cm/s for the 5 wt.% formulation. This inverse relationship between filler loading and flow rate demonstrates the increased viscosity and internal resistance to flow caused by the silica particles, which form a network that hinders the movement of the polymer chains [16]. Despite this reduction, the flow rates remained within a workable range for coating applications. The controlled increase in density and the corresponding adjustment in flow rate within the 1-5 wt.% range are considered beneficial for enhancing mechanical and barrier properties without compromising processability [17].

Table 5. Flow rate of epoxy composite solution

Silica Addition	Time (Second)	Height (cm)	FlowRate (cm/second)
0	32	11.5	0.36
0.3	45	11.5	0.26
0.5	72	11.5	0.16
0.75	117	11.5	0.10
1	130	11.5	0.09
3	147	11.5	0.08
5	160	11.5	0.07

3.5 Coating Layer Analysis

Optical microscopy analysis revealed a significant influence of the surface preparation method on the coating morphology and integrity. Coatings applied on abrasively blast-cleaned substrates. Figure 4 exhibited a uniform, void-free epoxy composite layer with a consistent thickness. In contrast, coatings on power tool-cleaned substrates showed the presence of residual oxide layers, indicating the method's inability to completely remove surface contaminants [13].

A key distinction was the presence of mechanical interlocking, visible in all samples on blast-cleaned surfaces (red circles, Fig. 4). This anchoring mechanism, resulting from the higher surface roughness, enhances coating adhesion [18]. This feature was absent in all coatings on power tool-cleaned surfaces (Fig. 5), which only provided cleaning without creating a significant anchoring profile [19].

The superior surface profile generated by abrasive blast cleaning is therefore concluded to be critical for achieving optimal coating adhesion and anticipated corrosion resistance.

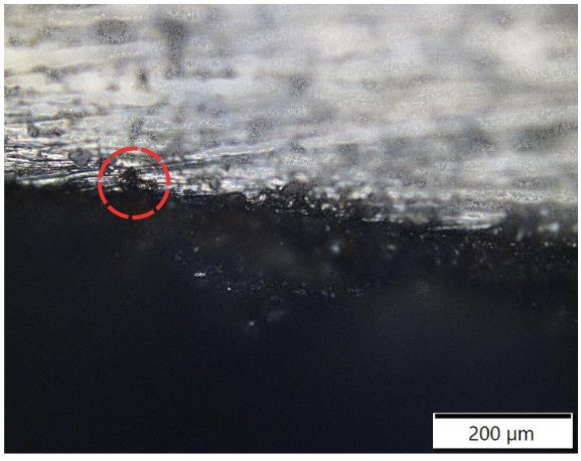

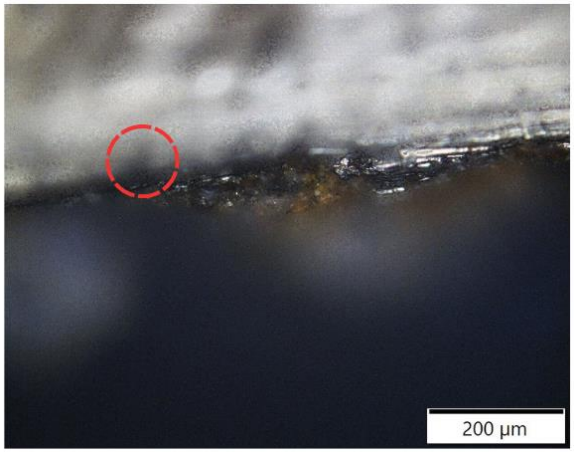

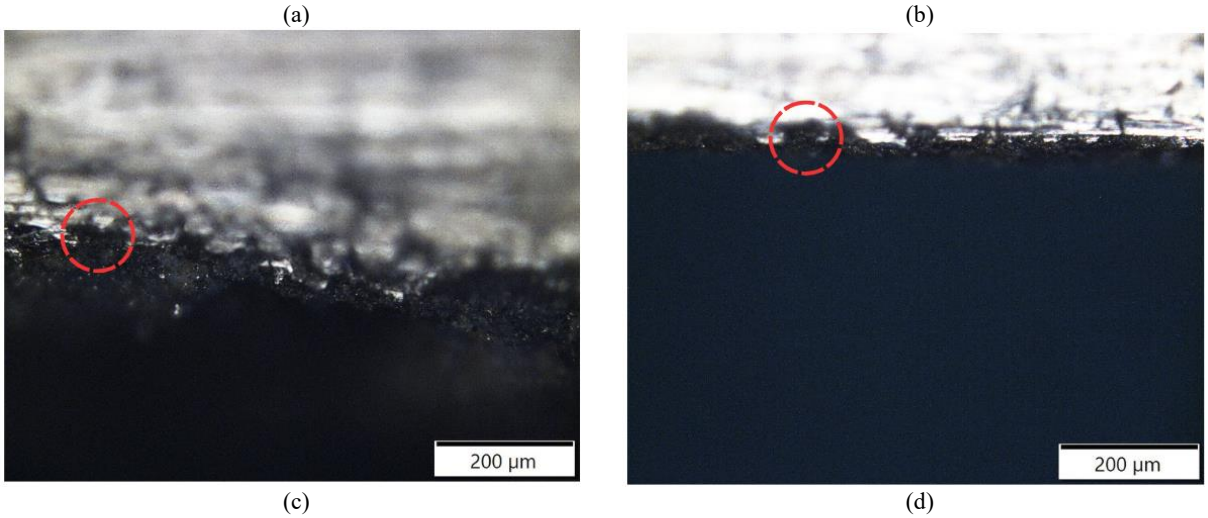

Figure 4. OM results on epoxy coatings using the abrasive blast cleaning method with the addition of silica filler (wt.%): (a) 0, (b)1, (c). 3 and (d) 5

3.5 Coating Thickness Analysis

The DFT (dry film thickness) of the cured epoxy coatings was measured at multiple points across all samples. Coatings applied on abrasively blast-cleaned substrates consistently yielded higher average thicknesses, ranging from approximately 170-227 µm across different silica loadings. In contrast, coatings on power tool-cleaned surfaces showed lower average thicknesses, ranging from about 104-164 µm [20]. This variation is attributed to the different surface profiles created by the preparation techniques. The rougher profile from abrasive blasting retained a thicker coating layer. Furthermore, for both methods, an increase in silica filler content generally resulted in a trend towards greater coating thickness, which aligns with the previously observed increase in composite density and viscosity [21]. Despite the variations, all measured thicknesses were within a range considered acceptable for protective coating applications [22].

3.6 Adhesion Strength Analysis

The adhesion of the epoxy-silica composite coatings was evaluated using two complementary methods: a qualitative tape test (x-cut) and a quantitative pull-off test. The results from both tests are detailed in the following subsections to provide a comprehensive analysis of the coating-substrate bond strength.

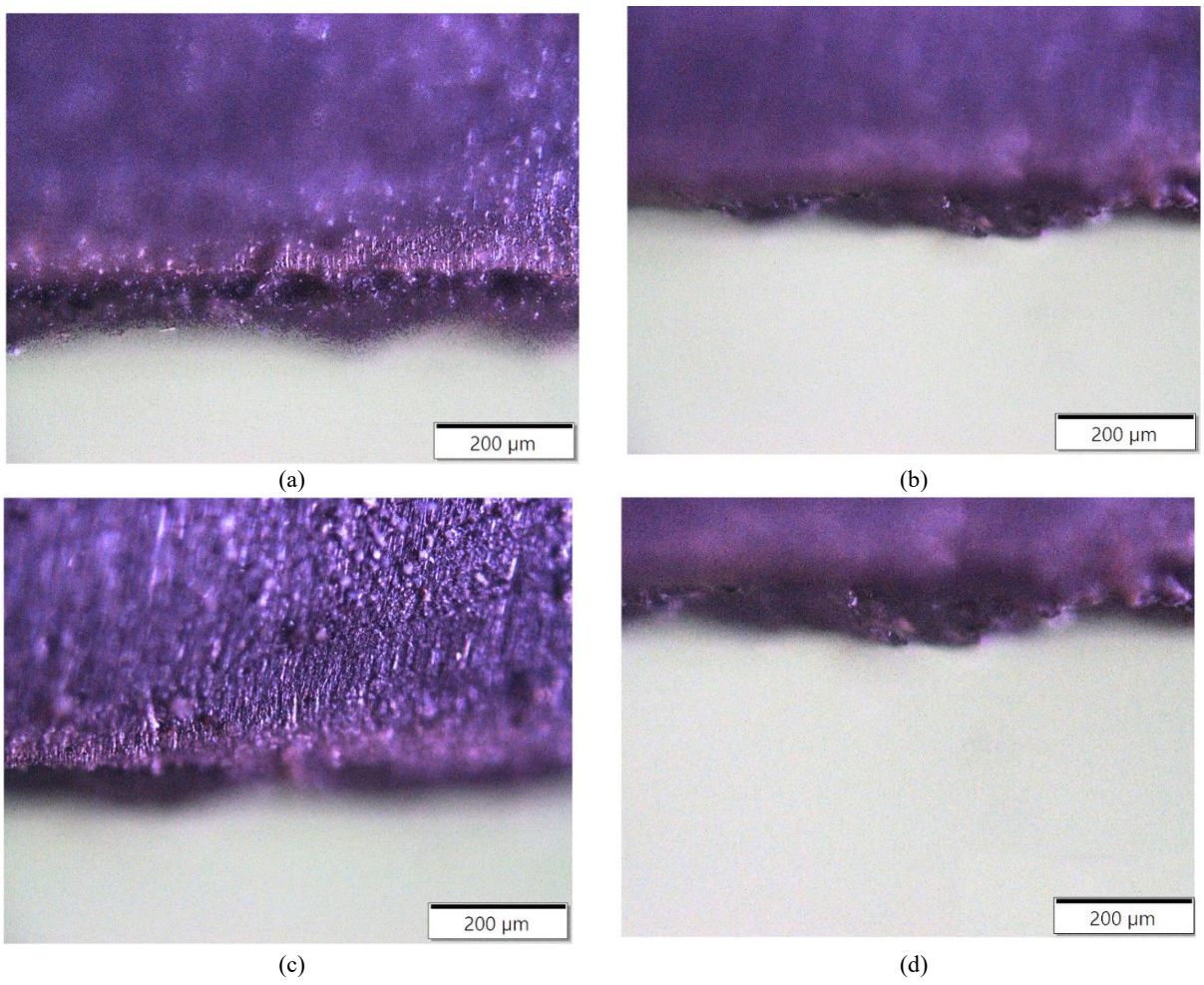

Figure 5. OM results on epoxy coatings using the power tool cleaning method with the addition of silica filler (wt.%): (a) 0, (b)1, (c). 3 and (d) 5

3.7 Tape X-Cut Test Results

The qualitative adhesion of the epoxy-silica composite coatings was evaluated using the Tape X-Cut test according to ASTM D3359. The results, detailed in Table 6, demonstrate a clear correlation between surface preparation, silica content, and adhesion performance.

Coatings applied on abrasively blast-cleaned substrates consistently achieved a perfect 5A rating (no peeling) across all silica loadings (0 to 5 wt.%). This superior performance is attributed to the high surface roughness generated by this method, which provides excellent mechanical interlocking for the coating [23].

In contrast, coatings on power tool-cleaned surfaces showed more variable results. While the 0.5 wt.% and 0.75 wt.% silica samples achieved a 5A rating, the unfilled (0 wt.%) and 0.3 wt.% samples showed lower adhesion with ratings of 4A and 3A, respectively. This indicates that the incorporation of silica filler above 0.5 wt.% significantly enhances adhesion strength [24], likely by improving the composite toughness and the interfacial bond between the polymer matrix and the substrate [25]. This effect compensates for the inherently lower surface profile provided by the power tool cleaning method.

3.8 Pul Off Test Results

Quantitative adhesion strength was evaluated using the pull-off test, revealing a significant influence of surface preparation and silica content. As shown in Figure 6, coatings applied on abrasively blast-cleaned substrates demonstrated a higher average adhesion strength (10.48 MPa) compared to those on power tool-cleaned surfaces (6.16 MPa) [26]. This is directly correlated with the superior surface roughness (79.4 µm) provided by abrasive blasting, which enhances mechanical interlocking [10].

Table 6. X-cut test result

Surface Preparation Methods	Dosage of Silica (wt.%)	antitative Scale of Adhesion Strength
Abrasive blast cleaning	0	5A
	1	5A
	3	5A
	5	5A
Power tool cleaning	0	4A
	0.3	3A

0.5	5A
0.75	5A

The effect of silica filler was distinct for each preparation method. For power tool cleaning, adhesion increased drastically to 9.33 MPa at 0.5 wt.% silica, demonstrating the filler's role in enhancing bond strength. For abrasive blast cleaning, the optimal adhesion strength of 14.33 MPa was achieved at 3 wt.% silica.

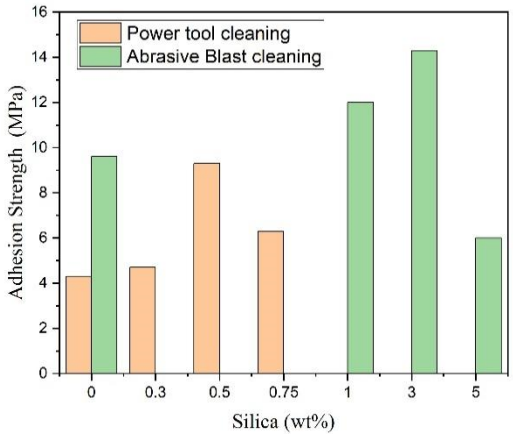

Figure 6. Comparison chart of adhesion strength of abrasive blast cleaning and power tool cleaning on silica materials

However, a further increase to 5 wt.% silica caused adhesion to drop to 6 MPa, likely due to filler agglomeration and a non-ideal, excessive coating thickness, which can lead to higher internal stresses [27]. Failure mode analysis showed a predominance of adhesive failure (60-90%), indicating that the interface bond was stronger than the internal strength of the coating itself in most cases.

3.9 Coating Corrosion Resistance

The corrosion resistance of the coatings was evaluated using a scratch test, where an X-shaped scribe was made on the coating, and the sample was exposed to a 5% NaCl salt spray for 72 hours. The creepage, or under-film corrosion, from the scribe was measured periodically.

The results, detailed in Figs. 7 and 8, demonstrate a clear trend: coatings applied on abrasively blast-cleaned substrates (Fig. 8) exhibited significantly lower creepage and higher rating numbers than those on power tool-cleaned surfaces (Fig. 7) for all silica loadings [28].

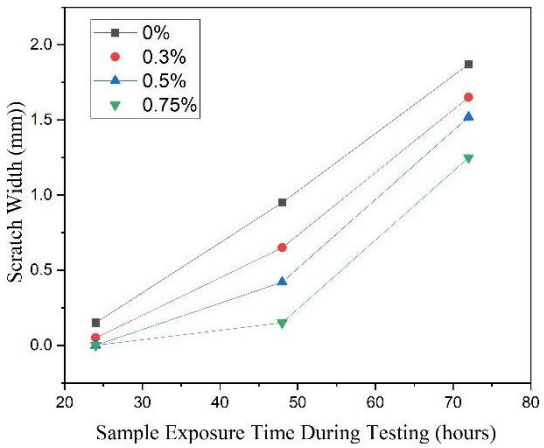

Figure 7. Comparison chart of pattern width vs exposure time for each addition of silica using the power tool cleaning method

This confirms the dominant role of surface preparation, where the superior profile from abrasive blasting provides a more effective barrier against corrosion undercutting [29].

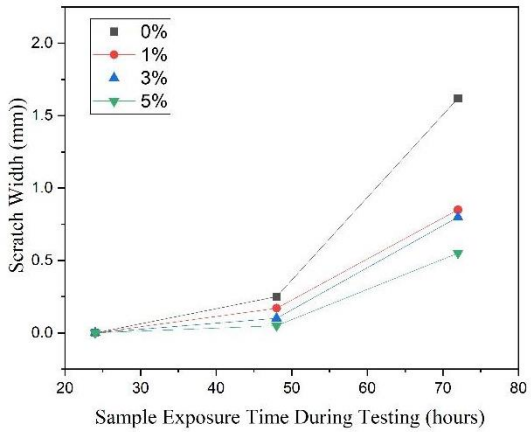

Figure 8. Comparison chart of pattern width versus exposure time for each addition of silica using abrasive blast cleaning

Furthermore, within each preparation method, the addition of silica filler consistently improved corrosion resistance. For power tool cleaning, the 0.75 wt.% silica sample showed the best performance (1.55 mm creepage after 72h). For abrasive blast cleaning, the 5 wt.% silica sample provided the optimal protection, with the lowest final creepage of 0.55 mm. This indicates that silica enhances the coating's barrier properties, but its effectiveness is maximized when combined with an appropriate surface profile [30].

The effect of surface roughness is evident when comparing power tool cleaning and abrasive blast cleaning samples. Power tool cleaning shows greater blister widening over time due to under film corrosion, where an oxide layer forms between the coating and substrate. This layer reduces adhesion strength and accelerates corrosion, consistent with previous studies [29].

4 CONCLUSION

Based on the findings of this study, it is concluded that the surface roughness of low carbon steel, dictated by the preparation method, is a fundamental factor controlling the adhesion performance that can contribute to the corrosion performance of silica-epoxy composite coatings. Abrasive blast cleaning, which produced a superior surface roughness (79 μm), was proven to be the critical enabler for both perfect adhesion (5A) using the tape x cut test and the pull off test (10.48 MPa), which increase 41% of adhesion strength compared to the average of power tool cleaning. The optimal adhesive strength (14.33 MPa) was achieved with 3 wt.% silica. Notably, the highest corrosion resistance, evidenced by a minimal creepage of 0.55 mm after 72 hours, was attained with 5 wt.% silica on this properly roughened surface, underscoring that optimal corrosion protection is achieved through the synergy of adequate filler concentration and a substrate roughness that ensures flawless coating adhesion.

ACKNOWLEDGEMENT

The authors would like to express their sincere gratitude to the National Research and Innovation Agency (BRIN) for funding this research through the LPDP program, managed by BRIN under the RIIM Funding Program with grant numbers: B-807/II.7.5/FR/6/2022 and B-6952/III.10/KS.00.00/6/2022.

REFERENCES

[1] P. Refait, A.-M. Grolleau, M. Jeannin, C. Rémazeilles, and R. Sabot, "Corrosion of carbon steel in marine environments: Role of the corrosion product layer," *Corrosion and Materials Degradation*, vol. 1, no. 1, pp. 198-218, 2020. DOI: 10.3390/cmd1010010

[2] M. F. Álvarez, F. Velasco, A. Bautista, F. C. M. Lobo, E. M. Fernandes, and R. L. Reis, "Manufacturing and characterization of coatings from polyamide powders functionalized with nanosilica," *Polymers*, vol. 12, no. 10, p. 2298, 2020. DOI: 10.3390/polym12102298.

[3] A. Szewczak and M. Szeląg, "Physico-mechanical and rheological properties of epoxy adhesives modified by microsilica and sonication process," *Materials*, vol. 13, no. 23, p. 5310, 2020. DOI: 10.3390/ma13235310.

[4] A. B. Prasetyo, M. Handayani, E. Sulistiyo, F. Firdiyono, E. Febriana, W. Mayangsari, S. Wahyuningsih, E. Pramono, A Maksum, R. Riastuti, and J. W. Soedarsono, "Fabrication of high-purity silica precipitates from quartz sand toward photovoltaic application," *Journal of Ceramic Processing Research*, vol. 24, no. 1, pp. 103-110, 2023. DOI: 10.36410/jcpr.2023.24.1.103.

[5] A. A. Khan, A. Khan, Z. Zafar, I. Ahmad, and B. Islam, "Corrosion protection of aluminum alloy 7075 using functionalized micro-silica-based epoxy coatings," *Materials Research Express*, vol. 10, no. 4, p. 45301, 2023. DOI: 10.1088/2053-1591/acc6b5.

[6] A. Guzanová, J. Brezinová, D. Draganovská, and F. Jaš, "A study of the effect of surface pre-treatment on the adhesion of coatings," *Journal of Adhesion Science and Technology*, vol. 28, no. 17, pp. 1754-1771, 2014. DOI: 10.1080/01694243.2014.920762.

[7] M. K. Schäfer, "Ultrasonic mixing head for resin transfer molding: The interaction between sonication, process characteristics and resin system properties," Universität München, 2018.

[8] M. Brogly, "Forces involved in adhesion," *in Handbook of Adhesion Technology*, L. F. M. da Silva, A. Öchsner, and R. D. Adams, Eds., Cham: Springer International Publishing, pp. 1-28, 2017. DOI: 10.1007/978-3-319-42087-5_3-2.

[9] A. Rudawska, I. Danczak, M. Müller, and P. Valasek, "The effect of sandblasting on surface properties for adhesion," *International Journal of Adhesion and Adhesives*, vol. 70, pp. 176-190, 2016. DOI: 10.1016/j.ijadhadh.2016.06.010.

[10] W. Pathanatecha, "A study of various parameters affecting adhesion of coatings to metal substrates," 2019. [Online]. Available: https://api.semanticscholar.org/CorpusID:215762179

[11] M. A. Iglesias-Campos, "Effects of mechanical cleaning by manual brushing and abrasive blasting on lime render coatings on architectural heritage," *Materiales de Construcción*, vol. 64, no. 316, p. e039, 2014. DOI: 10.3989/mc.2014.08313.

[12] R. Wang, C. Zhang, and W. Liu, "Compatibility and anti-oxidation properties of study on liquid oxygen

compatibility with nano-modified epoxy composites," *Polymers and Polymer Composites*, vol. 19, no. 4-5, pp. 351-356, 2011. DOI: 10.1177/0967391111019004-515.

[13] M. F. Uddin and C. T. Sun, "Improved dispersion and mechanical properties of hybrid nanocomposites," *Composites Science and Technology*, vol. 70, no. 2, pp. 223-230, 2010. DOI: 10.1016/j.compscitech.2009.09.017.

[14] B. B. Johnsen, T. R. Fromyr, T. Thorvaldsen, and T. Olsen, "Preparation and characterization of epoxy/alumina polymer nanocomposites," *Composite Interfaces*, vol. 20, no. 9, pp. 721-740, 2013. DOI: 10.1080/15685543.2013.815603.

[15] R. J. Ghayyib, A. J. Salman, Z. F. Jawad, and Z. S. Al-Khafaji, "Effect of silica-based wastes on wear rate and hardness properties of epoxy composites as a construction material," *Key Engineering Materials*, vol. 895, pp. 31-40, 2021. DOI: 10.4028/www.scientific.net/KEM.895.31.

[16] R. Babba, K. Hebbache, A. Douadi, M. Boutlikht, R. Hammouche, S. Dahmani, G. D. Serroni and L. Morreti, "Impact of silica sand on mechanical properties of epoxy resin composites and their application in CFRP-concrete bonding," *Applied Sciences*, vol. 14, no. 15, p. 6599, 2024. DOI: 10.3390/app14156599.

[17] J. Sroka, A. Rybak, R. Sekula, and M. Sitarz, "An investigation into the influence of filler silanization conditions on mechanical and thermal parameters of epoxy resin-fly ash composites," *Journal of Polymers and the Environment*, vol. 24, no. 4, pp. 298-308, 2016. DOI: 10.1007/s10924-016-0773-8.

[18] C. Li, X. Jia, S. Wu, F. Li, X. Wang, and Y. Ren, "The removal mechanism considering the shape and size of abrasive particles in wet blast cleaning of paint," *Sustainability*, vol. 14, no. 21, p. 14289, 2022. DOI: 10.3390/su142114289.

[19] A. R. Safin, R. R. Khusnutdinov, and A. M. Kopylov, "The method topological optimization for design linear electric machines," in *2019 International Science and Technology Conference "EastConf,"* pp. 1-6, 2019. DOI: 10.1109/EastConf.2019.8725379.

[20] S. Luangkularb, S. Prombanpong, and V. Tangwarodomnukun, "Material consumption and dry film thickness in spray coating process," *Procedia CIRP*, vol. 17, pp. 789-794, 2014. DOI: 10.1016/j.procir.2014.02.046.

[21] S. R. Harisha, S. Sharma, U. A. Kini, and M. C. G. Shankar, "Study on spheroidization and related heat treatments of medium carbon alloy steels," *MATEC Web of Conferences*, vol. 144, p. 02008, 2018. DOI: 10.1051/matecconf/201714402008.

[22] S. Henkel, F. Beyrau, Y. Hardalupas, and A. M. K. P. Taylor, "Novel method for the measurement of liquid film thickness during fuel spray impingement on surfaces," *Optics Express*, vol. 24, no. 3, p. 2542, 2016. DOI: 10.1364/OE.24.002542.

[23] A. Kim, S. Kainuma, and M. Yang, "Surface characteristics and corrosion behavior of carbon steel treated by abrasive blasting," *Metals*, vol. 11, no. 12, p. 2065, 2021. DOI: 10.3390/met11122065.

[24] D. Schaubroeck, "Surface modifications of epoxy resins to improve the adhesion towards electroless deposited copper," Ghent University, 2015.

[25] A. J. Kinloch, J. H. Lee, A. C. Taylor, S. Sprenger, C. Eger, and D. Egan, "Toughening structural adhesives via nano- and micro-phase inclusions," *The Journal of Adhesion*, vol. 79, no. 8-9, pp. 867-873, 2003. DOI: 10.1080/00218460309551.

[26] Z. Zhang, Y. Wang, J. Lin, and D. Wang, "Study on factors influencing film formation of grease and calculation model for grease film thickness," *Lubricants*, vol. 10, no. 6, p. 123, 2022. DOI: 10.3390/lubricants10060123.

[27] M. A. Deyab, B. El Bali, Q. Mohsen, and R. Essehli, "Design new epoxy nanocomposite coatings based on metal vanadium oxy-phosphate M0.5VOPO4 for anti-corrosion applications," *Scientific Reports*, vol. 11, no. 1, p. 8182, 2021. DOI: 10.1038/s41598-021-87567-3.

[28] Sheetal, B. Chugh, S. Thakur, B. Pani, and A. K. Singh, "Fundamentals of corrosion chemistry," 2021, pp. 21-36. DOI: 10.1021/bk-2021-1403.ch002.

[29] M. Niknahad, S. Moradian, and S. M. Mirabedini, "The adhesion properties and corrosion performance of differently pretreated epoxy coatings on an aluminium alloy," *Corrosion Science*, vol. 52, no. 6, pp. 1948–1957, Jun. 2010, doi: 10.1016/j.corsci.2010.02.014.

[30] J. Wang, "Application and performance study of protective coatings in corrosion

resistance on industrial equipment surfaces," J*ournal of protective coatings & linings*, vol. 42, no. 4, pp. 57–73, 2025, [Online]. Available: https://paintsquare.com/jpcl/articles/2025/4245773.pdf

Metalurgi (2024) 3: 129-140

METALURGI
Majalah Ilmu dan Teknologi
p-ISSN 0126-3188 | e-ISSN 2443-3926
ejurnalmaterialmetalurgi.lipi.go.id

KINETIC MODELLING OF SOLID-LIQUID EXTRACTION OF TIN FROM DIMETHYLTIN DICHLORIDE BY-PRODUCTS: EFFECT OF SOLVENT AND STIRRING SPEED

Atika Putri Adenia[a,b]*, Jayanudin[a], Widya Ernayati Kosimaningrum[a], Teguh Kurniawan[a], Farah Alifia Zulfaidah[b], Yudhistira Madani Putra Siahaan[b]

[a]Department of Chemical Engineering, Universitas Sultan Ageng Tirtayasa
Jl. Jend. Sudirman Km. 3, Kotabumi, Banten, Indonesia 42435
[b]PT Timah Industri
Jl. Eropa 1 Kawasan Industri Krakatau 1 Kav. A3, Kotasari, Banten, Indonesia 42436
*E-mail: atikadenia@gmail.com

Received: 11-12-2025, Revised: 31-12-2025, Accepted: 6-1-2026

Abstract

Indonesia is the world's second-largest tin exporter; however, downstream utilization of tin remains limited. One potential source of secondary tin is the by-product generated from the production of DMT (dimethyltin dichloride) at PT Timah Industri, which contains 40–70% tin in both organic and inorganic forms. This study aims to investigate the extraction kinetics and evaluate the effects of solvent type and agitation speed on tin recovery from the DMT by-product. Extraction experiments were conducted using different solvents (water, 50% methanol, and pure methanol) and agitation speeds (300 and 400 rpm) for 24 hours. Tin concentrations in the filtrate were determined using XRF (x-ray fluorescence). Kinetic modeling was performed using first-order and second-order models through both linear and non-linear approaches. The results show that the extraction process follows second-order kinetics, with rate constants (k) in the short-time regime ranging from 0.002 to 0.005 L·(g·min)$^{-1}$ and in the long-time regime from 0.0001 to 0.0002 L·(g·min)$^{-1}$. Water demonstrated the highest dissolution capacity (35.35 ± 0.09%), while pure methanol selectively dissolved organotin compounds (30.45 ± 0.12%). The 50% methanol solvent yielded intermediate extraction results (32.65 ± 0.37%) due to the combined characteristics of both solvents. Agitation speed significantly enhanced tin dissolution.

Keywords: *Dimethyltin-dichloride-by-product, solid-liquid-extraction, extraction kinetics, valorization*

1. INTRODUCTION

Tin has re-emerged as a strategically important metal due to its critical applications in electronics, soldering materials, and catalytic processes. In Indonesia, tin downstream processing has become a national priority to enhance domestic value addition. However, current industrial practices still generate significant volumes of tin-bearing by-products that remain underutilized, creating gaps in circular-economy implementation and resource efficiency.

One such residue originates from the production of DMT (dimethyltin dichloride), which yields a solid by-product rich in organotin species, primarily DMT and monomethyltin trichloride (MMT), with tin contents reaching 40–70%. Despite this high value, the material remains unrecovered. Pyrometallurgical processing faces limitations due to volatilization of organotin species and stringent off-gas requirements, whereas hydrometallurgical extraction offers a more controlled and energy-efficient alternative [1]. Nevertheless, systematic understanding of dissolution mechanisms and kinetic behavior in industrial organotin residues remains very limited.

DOI: 10.55981/metalurgi.2024.785

Metalurgi is Sinta 2 Journal (https://sinta.kemdikbud.go.id/journals/profile/3708) accredited by Ministry of Education, Culture, Research, and Technology, Republic Indonesia

The extraction behavior of organotin compounds is strongly influenced by solvent properties. Although solubility data show that DMT and MMT dissolve more effectively in methanol than in water, and tin oxides remain largely insoluble [2]-[5], these assumptions have not been validated for complex industrial residues. Moreover, the combined effects of solvent system, extraction duration, and agitation intensity have rarely been examined, leaving fundamental questions about tin dissolution kinetics unanswered.

A crucial knowledge gap lies in the absence of reliable kinetic modeling. While pseudo-first-order and pseudo-second-order models are widely applied in hydrometallurgical systems, their applicability to organotin dissolution has not been evaluated [6]. Past studies often relied on linearized kinetic plots, which may introduce bias due to data transformation. In contrast, non-linear regression allows the full kinetic profile to be fitted without distortion, producing more accurate estimates of rate constants (k) and equilibrium concentrations (C_s) [7].

In many solid-liquid extraction systems, the kinetic curve exhibits two characteristic regimes: a short-time regime, dominated by external mass transfer and strongly influenced by agitation and solvent accessibility; and a long-time regime, where the rate gradually slows due to intraparticle diffusion or diminishing concentration gradients [8]. Recognizing these regimes is essential for distinguishing whether tin dissolution is controlled by surface reaction or diffusion limitations, and for selecting the most appropriate kinetic model and regression method.

Given these gaps, this study aims to: (i) evaluate the extraction performance of DMT by-product using water, methanol, and methanol–water mixtures under varying agitation rates; (ii) determine kinetic parameters using both linearized and non-linear regression of pseudo-first order and pseudo-second-order models; and (iii) establish a validated kinetic model describing tin dissolution behavior. The outcomes are expected to provide a robust solvent-parameter matrix for optimizing tin recovery and support sustainable hydrometallurgical strategies aligned with Indonesia's tin downstream agenda and global circular-economy initiatives.

The expected outcomes of this research include: (i) a validated kinetic model representing the extraction behavior of organotin species from industrial by-products, (ii) a solvent process parameter matrix for optimizing tin recovery

2. MATERIALS AND METHODS

2.1 Materials

The main material used in this study was the DMT by-product collected from a single production line of the DMT unit at PT Timah Industri (Fig. 1). Analytical-grade methanol (>99.8% PA), 50% methanol solution, and deionized water were used as solvents for the solid–liquid extraction process. All chemicals in this study were used without further purification.

Figure 1. DMT by-product sample

2.2 Solid-liquid extraction of tin

The sample was prepared through grinding, sieving, and mixing to obtain a uniform particle máximum size of 10 mesh. A total of 50 g of sample was mixed with 500 mL of solvent under stirring at either 300 or 400 rpm. Three types of solvents were tested: deionized water, a 50:50 methanol-water mixture, and pure methanol. The extraction process was carried out for 24 hours at ambient temperature. Samples were collected at specific time intervals: 0, 2, 4, 8, 15, 30, 60, 120, 240, 480, 960, and 1440 minutes. The tin concentration in the liquid samples was determined using XRF (x-ray fluorescence) analysis with a Malvern Panalytical Epsilon 1 instrument operating in the 7-50 keV energy range.

For the analysis, liquid filtrates were poured into dedicated XRF (x-ray fluorescence) liquid cups sealed with a 3 µm polypropylene thin film. This non-destructive method was selected due to the high concentration of tin in the samples (approximately 20–35%), which allowed for direct measurement without the extensive dilution required by ICP-OES (inductively coupled plasma-optical emission spectrometry) or AAS (atomic absorption spectrometry), thereby

minimizing potential dilution errors. Each experimental condition was performed in triplicate, and the reported data represents the average values of three independent runs.

2.3 Kinetic Modeling

In the extraction of tin from DMT by-product, the kinetics models tested for the research sample data were first-order and second-order kinetics. The first-order kinetics model is an equation that describes the value of the extraction rate, which is proportional to a driving force in the form of concentration (Cs-Ct), and this equation has a correlation to the linear driving force. In general, the equation is written in Eq. (1), while the second-order kinetics model assumes extraction influenced by surface adsorption-desorption and intraparticle diffusion in Eq. (2).

$$\frac{dC_t}{d_t} = k(C_s - C_t) \qquad \text{Eq. (1)}$$

$$\frac{dC_t}{d_t} = k(C_s - C_t)^2 \qquad \text{Eq. (2)}$$

For Cs is the concentration of tin when it reaches equilibrium (%), Ct is the concentration of tin at a certain time or extraction operation time (%), and k is the value of the extraction rate constant (min -1). It can be made linearly in the form of Eq. (3) and Eq. (4) by integrating Eq. (1) and Eq. (2), with boundary conditions when t = 0; Ct = 0 and when t = t; Ct = Ct.

$$ln\,(C_s - C_t) = \ln(C_s) - kt \qquad \text{Eq. (3)}$$

$$\frac{t}{C_t} = \frac{1}{kC_s{}^2} + \frac{1}{C_s}t \qquad \text{Eq. (4)}$$

For the first-order, the value of k can then be found by plotting t as the x-axis and ln(Cs-Ct) on the y-axis, while for the second-order, by plotting t/Ct vs t. It will provide a slope and intercept that can be used to find the value of the extraction rate constant of the first order (k).

While for the regression non-linear form, Eq. (5) and Eq (6) are used for model fitting performed using software Microsoft Excel to obtain rate constant k and equilibrium concentration Cs [9], [10].

$$C_t = C_s\,(1 - e^{-kt}) \qquad \text{Eq. (5)}$$

$$C_t = \frac{kC_s{}^2 t}{1 + kC_s t} \qquad \text{Eq. (6)}$$

3. Results and Discussion

3.1 Solid–liquid extraction of tin

The solid–liquid extraction process of the DMT by-product over 24 h with sampling at selected time intervals is presented in Fig. 2.

The concentration of tin increased progressively with longer extraction time. According to the last research [8], this trend arises from the prolonged contact time between the solvent and solid, which enhances mass transfer. A rapid increase in tin concentration was observed during the initial stage, followed by a gradual rise and eventual plateau as the extraction progressed. The rapid-extraction stage occurs at the beginning of the process, where tin species are readily released. As time progresses, the extraction rate decreases and approaches a nearly constant tin concentration. This behavior is crucial for subsequent kinetic modeling. Figure 2 also shows clear variations in extraction performance depending on the solvent used. Each solvent exhibits significantly different extraction behavior.

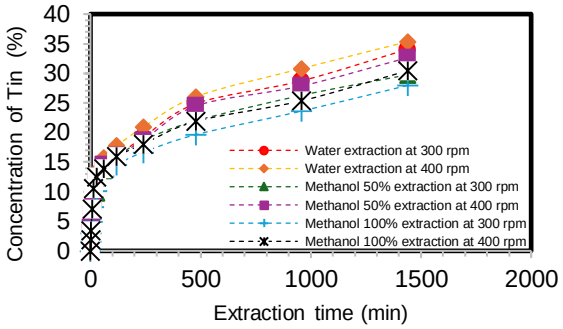

Figure 2. Extraction of tin (Sn) in DMTC-BP over time

Table 1 summarizes the average tin concentration obtained after 24 h. Water produced the highest tin concentration compared to 50% methanol and pure methanol. Increasing agitation speed from 300 to 400 rpm also enhanced extraction efficiency for all solvents, indicating the contribution of both solvent properties and hydrodynamic conditions. The average tin concentrations from triplicate experiments show that 400 rpm consistently produced higher tin concentrations than 300 rpm for all solvents. The highest tin concentration (35.35 ± 0.09%) was obtained using water, while the lowest (27.96 ± 0.71%) was obtained using pure methanol.

The two-way ANOVA results presented in Table 2 indicate that solvent type, agitation speed, and their interaction significantly affect the extraction performance. The F-value for solvent type (1184.69) is higher than the F-critical value of 2.48, with a P-value of 0.00 (<0.05), indicating a significant influence of solvent variation.

Table 1. Tin extraction yield: average result after 24 hours

Solvent Type	Stirring Speed	Final Tin Yield (%)
Water	300 rpm	34.07 ± 0.39
Water	400 rpm	35.35 ± 0.09
Methanol 50%	300 rpm	29.75 ± 3.62
Methanol 50%	400 rpm	32.65 ± 0.37

Methanol	300 rpm	27.96 ± 0.71
Methanol	400 rpm	30.45 ± 0.12

This suggests that the ability of solvents to dissolve or extract tin species from the DMT by-product differs according to their chemical characteristics.

Table 2. Analysis of variance of the experimental data for Tin (Sn) extraction

Source of Variation	F	P-value	F crit
Solvent types (a)	1184.69	0.00	2.48
Stirring speed (b)	252639.99	0.00	3.26
(a)*(b)	1109.18	0.00	2.11

Agitation speed shows the highest F-value (252639.99 > 3.26) with a P-value of 0.00, indicating that it is the most dominant factor. Higher agitation speed enhances mass transfer between the solid and liquid phases, increasing extraction efficiency. Furthermore, the interaction between solvent type and agitation speed is also significant (F = 1109.18 > 2.11; P = 0.00), showing that the effect of solvent type depends on the agitation conditions. Therefore, optimizing both solvent selection and agitation speed is crucial for maximizing extraction performance.

3.2 Extraction kinetics

Figures 3 and 4 present the first-order and second-order kinetic models. Kinetic parameters were calculated from the slope and intercept of each linear plot, while the coefficient of determination (R^2) was used to select the most suitable model [11].

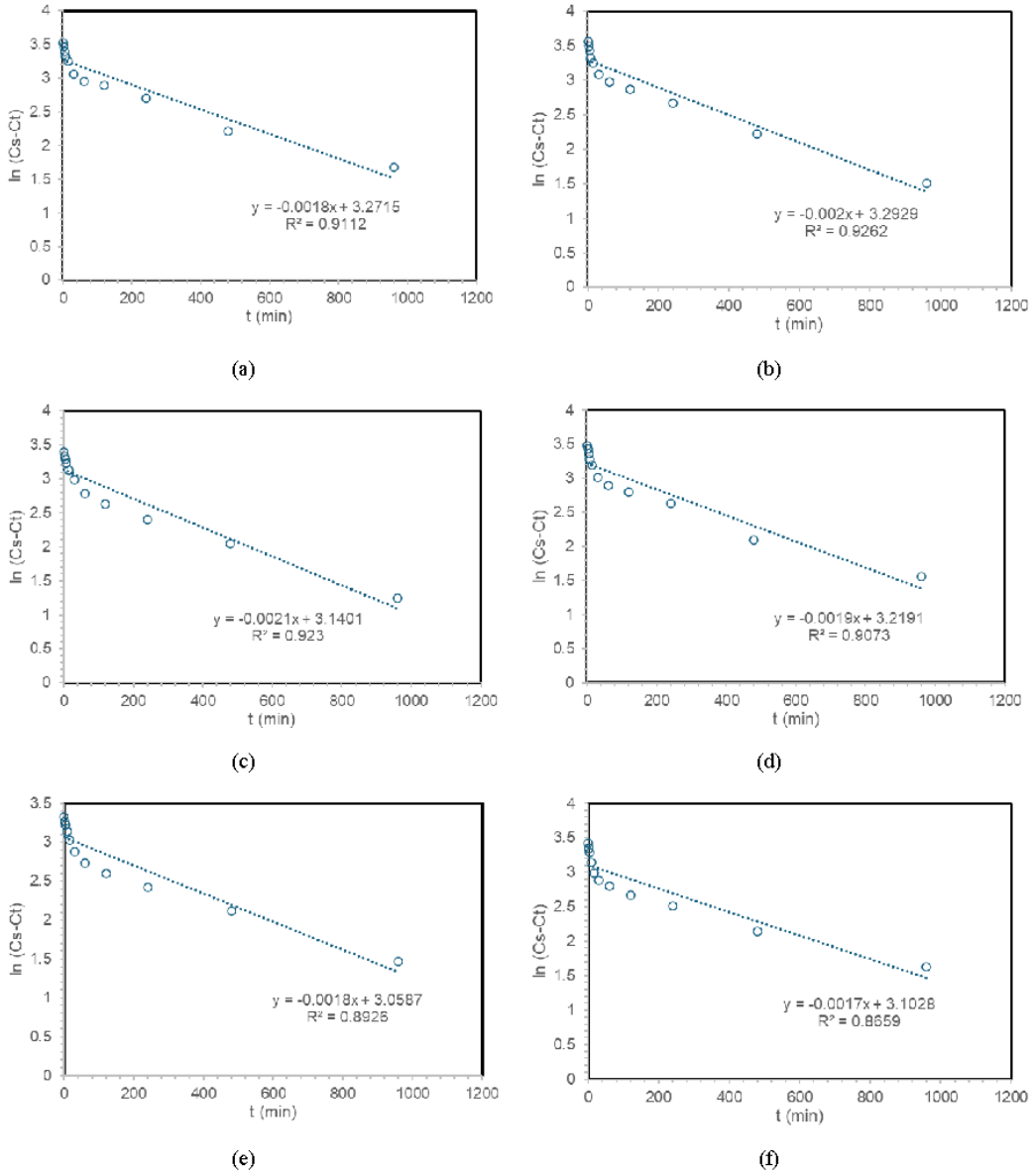

Figure 3. Linear plots of the first-order kinetic model for tin extraction from DMT by-products: (a) water solvent at 300 rpm; (b) water solvent at 400 rpm; (c) 50% methanol solvent at 300 rpm; (d) 50% methanol solvent at 400 rpm; (e) pure methanol solvent at 300 rpm; (f) pure methanol solvent at 400 rpm

The second-order kinetic model produced the highest R^2 values, indicating that it better predicts the extraction behavior. The kinetic parameters (k and Cs) in the second-order model were generally larger than those in the first-order model. First-order R^2 values ranged from 0.86 to 0.92, while second-order values exceeded 0.98. Based on these R^2 values, the second-order model more accurately represents the extraction rate of tin from the DMT by-product.

However, RMSE values in Table 3 show that the second-order model produced larger RMSE values, meaning poorer numerical fit despite a high R^2. Ideally, smaller RMSE values indicate better model accuracy [12].

Table 3. Kinetic parameters of the first-order and second-order extraction models using the linear method

No	Solvents	rpm	Kinetic models	k	Cs	R^2	RMSE
1	Water	300	First order	0.002	26.330	0.911	8.364
2	Water	300	Second order	0.000	33.560	0.980	14.549
3	Water	400	First order	0.002	26.900	0.926	8.958
4	Water	400	Second order	0.000	35.090	0.984	15.022
5	Methanol 50%	300	First order	0.002	23.120	0.923	7.138
6	Methanol 50%	300	Second order	0.000	29.760	0.988	12.665
7	Methanol 50%	400	First order	0.002	24.990	0.907	8.190
8	Methanol 50%	400	Second order	0.000	32.260	0.983	13.628
9	Methanol	300	First order	0.002	21.320	0.893	7.196
10	Methanol	300	Second order	0.000	27.400	0.981	10.930
11	Methanol	400	First order	0.002	22.250	0.866	8.799
12	Methanol	400	Second order	0.000	29.590	0.980	11.746

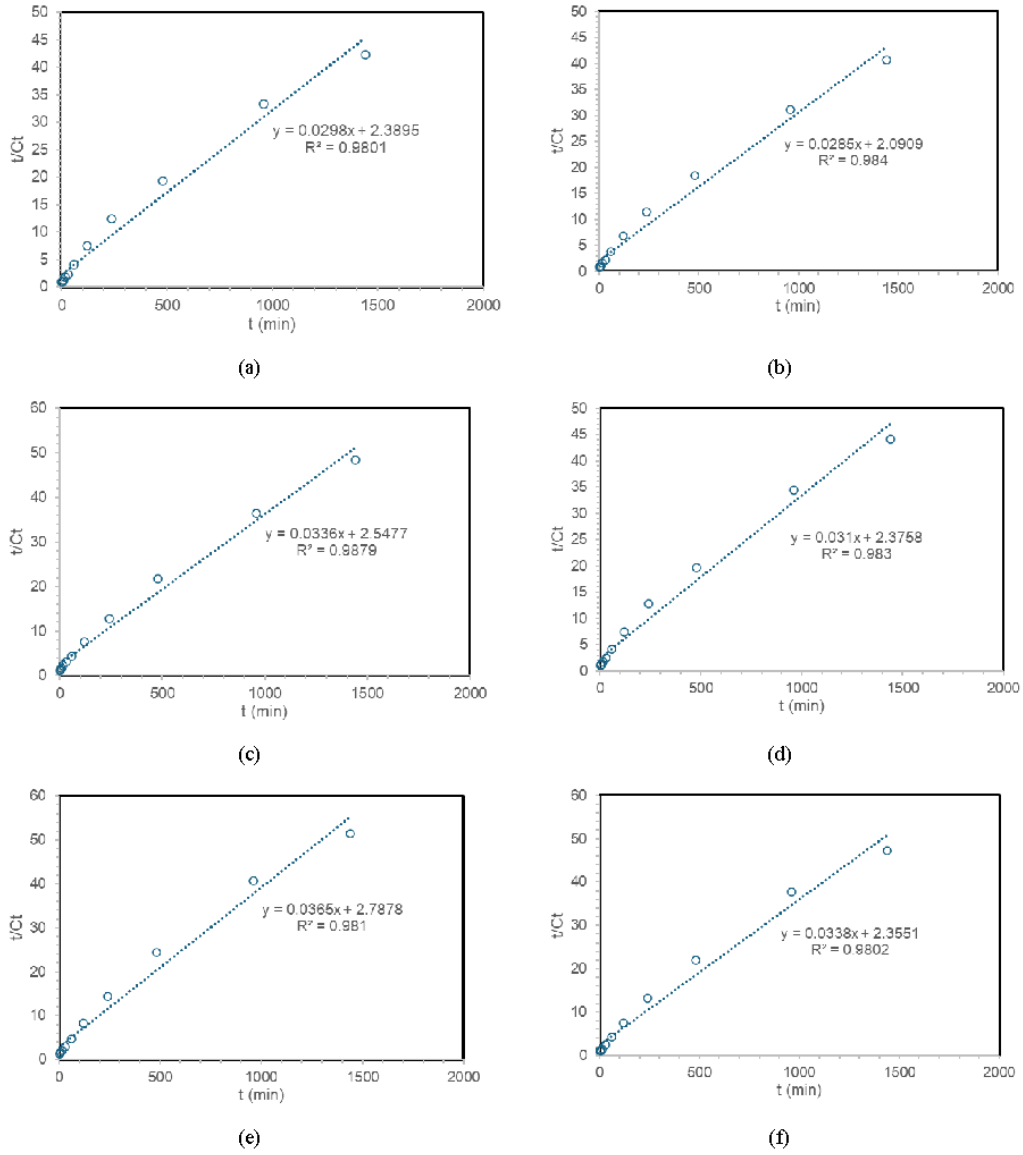

Figure 4. Linear plots of the second-order kinetic model for tin extraction from DMT by-products: (a) water solvent at 300 rpm; (b) water solvent at 400 rpm; (c) 50% methanol solvent at 300 rpm; (d) 50% methanol solvent at 400 rpm; (e) pure methanol solvent at 300 rpm; (f) pure methanol solvent at 400 rpm

This combination of high R^2 but high RMSE suggests that, although the model describes the general trend well, it does not fit the actual data precisely. While linear transformation can distort error distribution, creating misleadingly high R^2 values, nonlinear regression is recommended for more reliable kinetic parameter estimation.

Nonlinear modeling results (Table 4) show that first-order R^2 values remain similar to the linear approach (0.85–0.93), while second-order R^2 values decrease slightly but still remain higher (0.91–0.96). RMSE values are consistently smaller in the second-order model, indicating better model accuracy.

Table 4. Kinetic parameters of the first-order and second-order extraction models using the non-linear method

No	Solvents	rpm	Kinetic models	k	Cs	R^2	RMSE
1	Water	300	First order	0.011	27.340	0.893	3.831
2	Water	300	Second order	0.001	30.090	0.937	2.809
3	Water	400	First order	0.014	28.290	0.890	4.017
4	Water	400	Second order	0.001	31.160	0.938	2.910
5	Methanol 50%	300	First order	0.012	24.660	0.933	2.728
6	Methanol 50%	300	Second order	0.001	27.430	0.969	1.807
7	Methanol 50%	400	First order	0.010	32.650	0.906	5.007
8	Methanol 50%	400	Second order	0.001	28.910	0.941	2.608
9	Methanol	300	First order	0.015	21.910	0.899	2.938
10	Methanol	300	Second order	0.001	24.340	0.946	2.096
11	Methanol	400	First order	0.022	22.870	0.857	3.613
12	Methanol	400	Second order	0.001	25.280	0.918	2.684

DOI: 10.55981/metalurgi.2024.785

Metalurgi is Sinta 2 Journal (https://sinta.kemdikbud.go.id/journals/profile/3708) accredited by Ministry of Education, Culture, Research, and Technology, Republic Indonesia

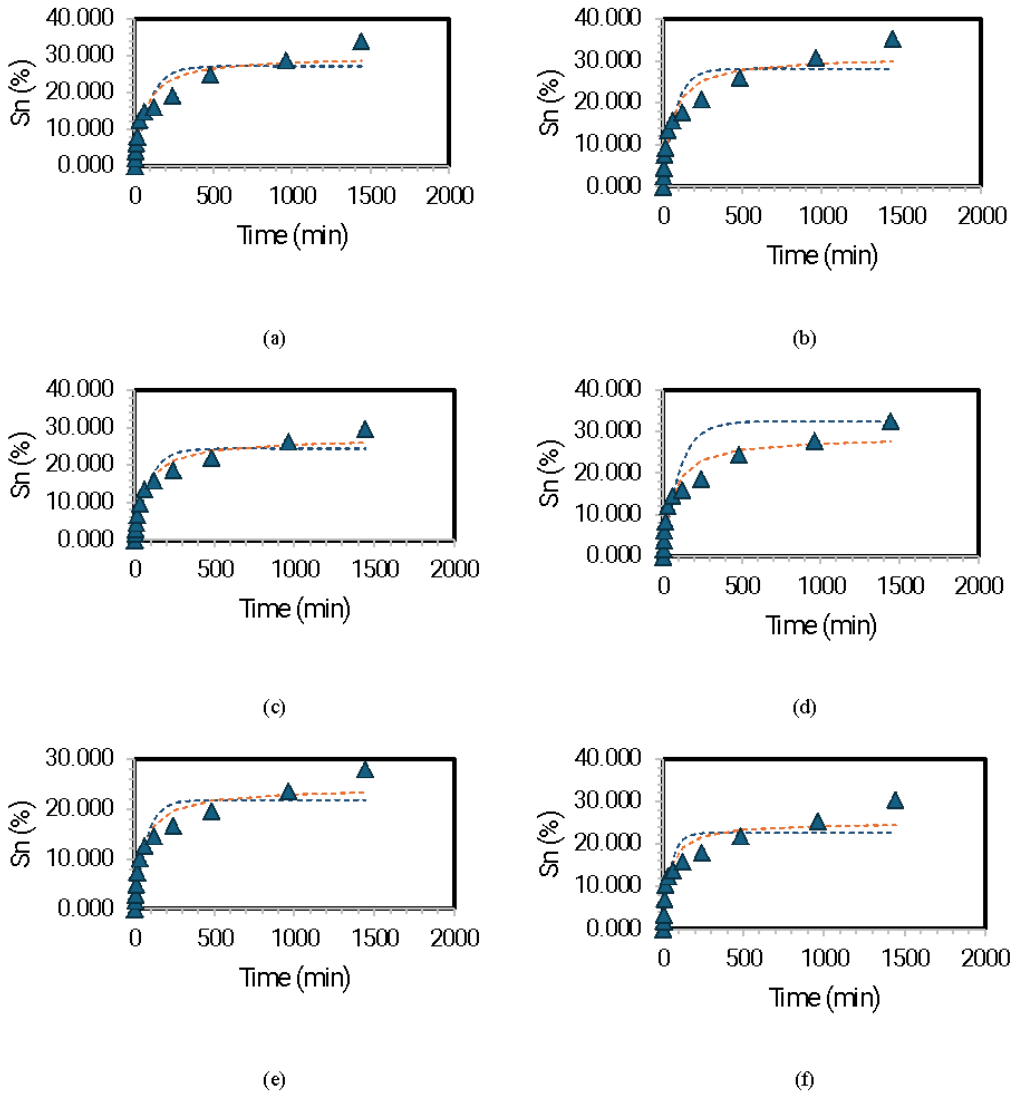

Figure 5. Comparison of experimental data with the non-linear extraction model for tin from DMT by-products: (a) water solvent at 300 rpm; (b) water solvent at 400 rpm; (c) 50% methanol solvent at 300 rpm; (d) 50% methanol solvent at 400 rpm; (e) pure methanol solvent at 300 rpm; (f) pure methanol solvent at 400 rpm (blue dashed line: first-order model, red dashed line: second-order model)

Nonlinear fitting also shows improved correspondence between the model and experimental data (Fig. 5), with reduced deviation compared to the linear approach. Nonlinear regression directly fits the original equation without mathematical transformation, resulting in more accurate and realistic kinetic parameter estimation [7], [12].

The extraction profile previously described, rapid extraction followed by a slower phase (Fig. 2), supports the interpretation that the process follows second-order kinetics. According to [10], second-order solid–liquid extraction kinetics indicate that the rate-limiting mechanism involves surface reactions and film diffusion rather than simple dissolution. This model is commonly associated with chemisorption-type interactions or strong interactions between solutes and solid surfaces. Second-order kinetics typically describe slower extraction processes and are consistent with long extraction durations [13]. This suggests the need for regime-based modeling to accurately represent the extraction behavior.

The extraction kinetics were further analyzed by separating the process into two regimes: rapid extraction (t = 0-120 min) and slow extraction (t = 240-1440 min). Figures 6 and 7 show the first- and second-order models under the two-regime approach. The nonlinear regression fitting significantly improved model accuracy for both kinetic models.

DOI: 10.55981/metalurgi.2024.785

Metalurgi is Sinta 2 Journal (https://sinta.kemdikbud.go.id/journals/profile/3708) accredited by Ministry of Education, Culture, Research, and Technology, Republic Indonesia

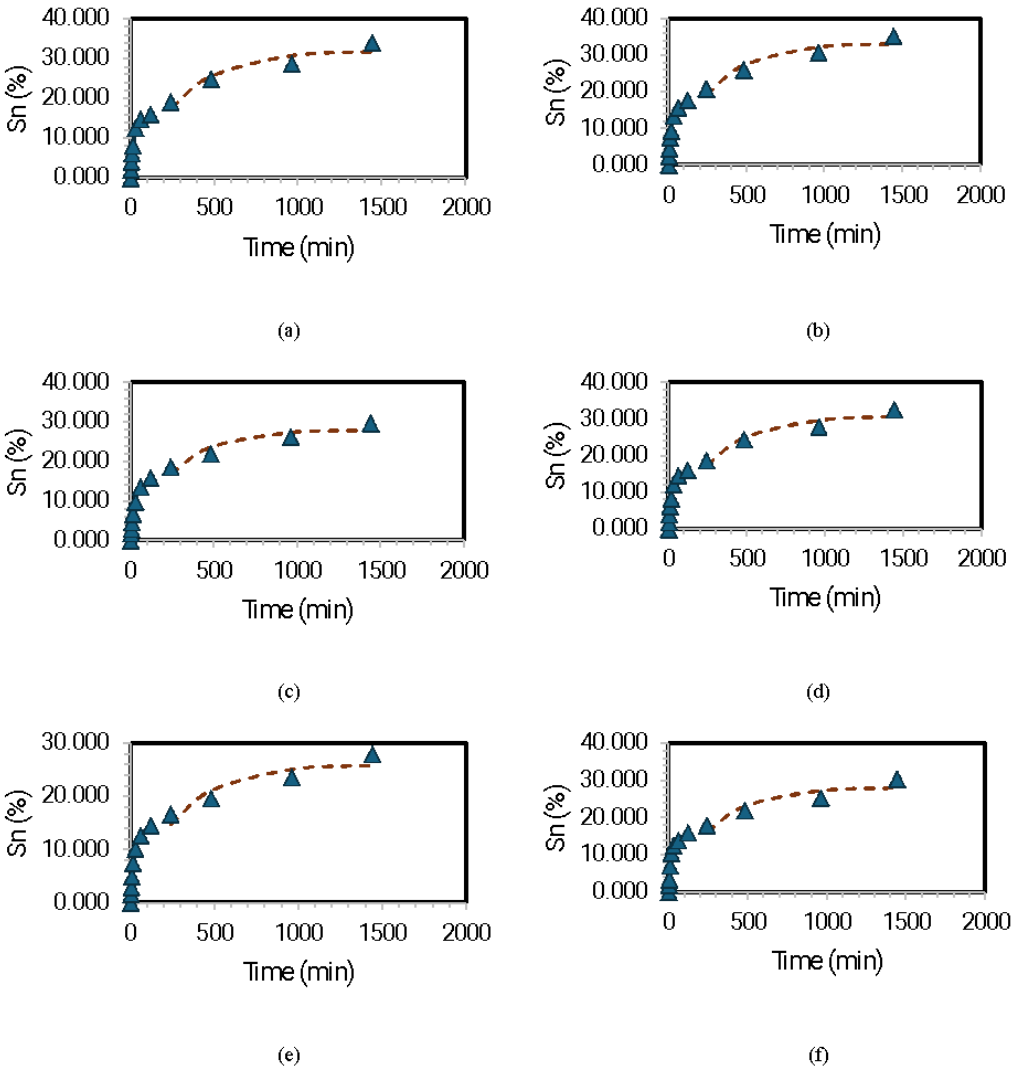

Figure 6. Comparison of experimental data with the first-order extraction model for tin from DMT by-products: (a) water solvent at 300 rpm; (b) water solvent at 400 rpm; (c) 50% methanol solvent at 300 rpm; (d) 50% methanol solvent at 400 rpm; (e) pure methanol solvent at 300 rpm; (f) pure methanol solvent at 400 rpm (blue dashed line: first-order model, red dashed line: second-order model)

DOI: 10.55981/metalurgi.2024.785

Metalurgi is Sinta 2 Journal (https://sinta.kemdikbud.go.id/journals/profile/3708) accredited by Ministry of Education, Culture, Research, and Technology, Republic Indonesia

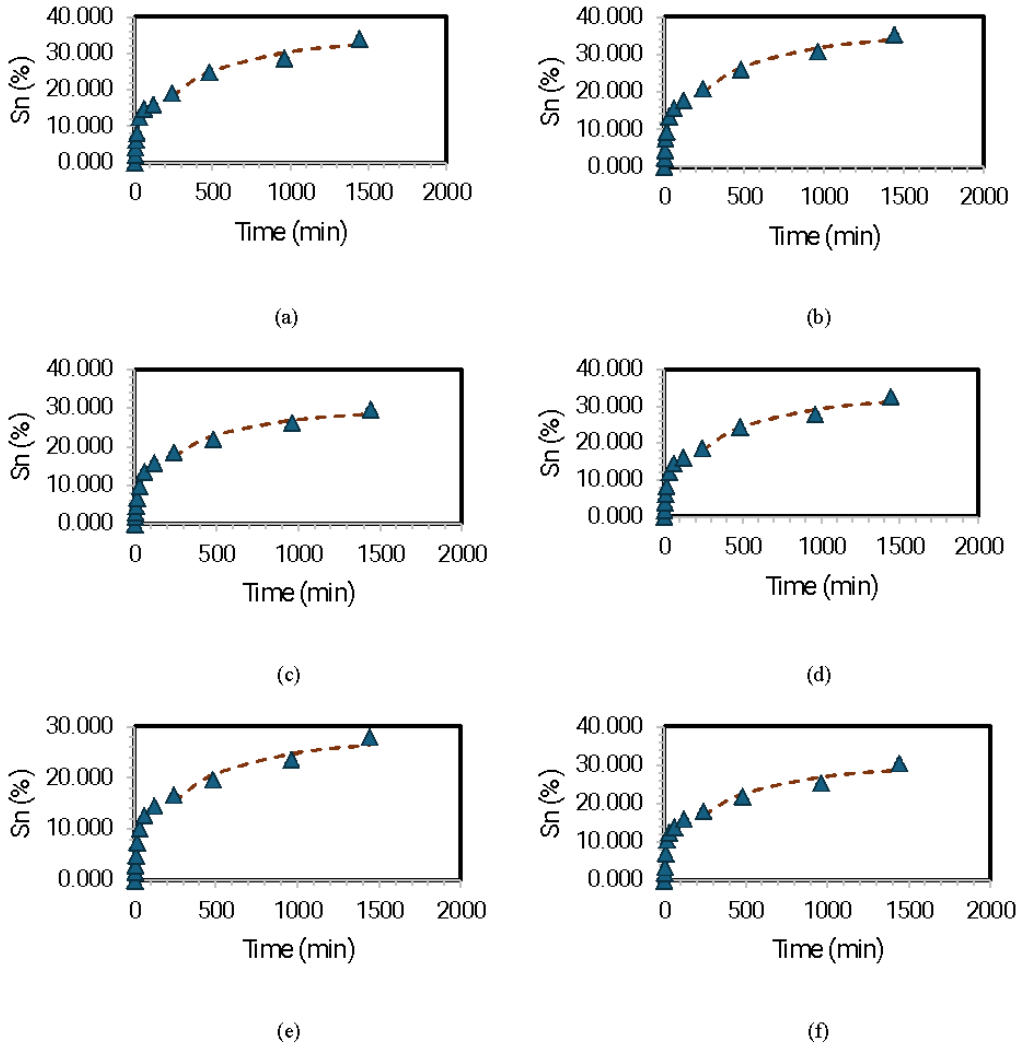

Figure 7. Comparison of experimental data with the second-order extraction model for tin from DMT by-products: (a) water solvent at 300 rpm; (b) water solvent at 400 rpm; (c) 50% methanol solvent at 300 rpm; (d) 50% methanol solvent at 400 rpm; (e) pure methanol solvent at 300 rpm; (f) pure methanol solvent at 400 rpm (blue dashed line: first-order model, red dashed line: second-order model)

The extraction rate constant (k) increased approximately fivefold in the rapid-extraction regime compared to the one-regime model (Table 5). For both orders, the value of k in the fast-extraction regime was consistently higher than in the slow-extraction regime, confirming the transition from fast surface release to diffusion-controlled extraction. According to [8], higher k-values reflect faster diffusion and evaporation processes, while lower values correspond to diffusion-limited stages.

In the two-regime model, the first-order R^2 increased substantially, reaching >0.99 in the rapid-extraction regime, approaching the R^2 of the second-order model. In the slow regime, R^2 values for both models decreased, but the second-order model still provided a better fit (Table 6). RMSE values consistently show that the second-order model yields lower RMSE in both regimes, reinforcing that second-order kinetics best represent the extraction behavior.

Table 5. Kinetic parameters of the first-order and second-order extraction models in the rapid-extraction stage (short-time regime)

No	Solvents	rpm	Kinetic models	k	Cs	R^2	RMSE
1	Water	300	First order	0.0567	15.632	0.992	0.538
2	Water	300	Second order	0.0034	18.435	0.995	0.394
3	Water	400	First order	0.0623	16.769	0.990	0.752
4	Water	400	Second order	0.0036	19.636	0.997	0.335
5	Methanol 50%	300	First order	0.0373	15.608	0.993	0.548
6	Methanol 50%	300	Second order	0.0020	19.276	0.997	0.307
7	Methanol 50%	400	First order	0.0556	15.541	0.994	0.507
8	Methanol 50%	400	Second order	0.0033	18.412	0.998	0.243
9	Methanol	300	First order	0.0487	13.973	0.997	0.446
10	Methanol	300	Second order	0.0031	16.826	1.000	0.064
11	Methanol	400	First order	0.0745	14.877	0.992	0.614
12	Methanol	400	Second order	0.0047	17.426	0.992	0.526

The second-order extraction behavior is also linked to possible partial hydrolysis of organotin compounds during extraction. [13] suggests that

second-order kinetics may involve hydrolysis of organic species during solid–liquid extraction. According to [14], dissolved organotin species exhibit Lewis acidity with different hardness levels ($RSn^{3+} > R_2Sn^{2+} > R_3Sn^{+}$), and all undergo hydrolysis to varying extents in aqueous solutions (Table 7).

Table 6. Kinetic parameters of the first-order and second-order extraction models in the slow-extraction stage (long-time regime)

No	Solvents	rpm	Kinetic models	k	Cs	R^2	RMSE
1	Water	300	First order	0.0034	32.228	0.905	1.726
2	Water	300	Second order	0.0001	38.546	0.958	1.118
3	Water	400	First order	0.0036	33.627	0.911	1.676
4	Water	400	Second order	0.0001	39.747	0.969	0.954
5	Methanol 50%	300	First order	0.0039	28.146	0.869	1.587
6	Methanol 50%	300	Second order	0.0002	32.751	0.951	0.941
7	Methanol 50%	400	First order	0.0035	30.922	0.924	1.462
8	Methanol 50%	400	Second order	0.0001	36.757	0.964	0.969
9	Methanol	300	First order	0.0035	26.192	0.844	1.761
10	Methanol	300	Second order	0.0001	30.988	0.923	1.190
11	Methanol	400	First order	0.0036	28.352	0.842	1.884
12	Methanol	400	Second order	0.0001	33.470	0.921	1.289

However, the hydrolysis behavior reported by [14] occurs at moderate pH values (pH 2–4.5). This contradicts the results of this study, where the extract solutions show much lower pH values (pH 0.81-1.65). At such strongly acidic conditions, hydrolysis is suppressed because water cannot act as a nucleophile due to the high proton concentration.

Any partially hydrolyzed species (e.g., $RSnCl_2(OH)$, $R_2SnCl(OH)$) would immediately reprotonate, reverting to their original halide forms. Consequently, the dominant species under these conditions are organotin halides such as DMT (R_2SnCl_2) and MMT ($RSnCl_3$), with minimal hydrolysis. Therefore, the extraction mechanism remains governed by surface reaction and film diffusion, consistent with second-order kinetics.

Table 7. Hydrolytic species formed under low organotin concentration conditions

Kation organotin	Spesies hidrolitik yang terbentuk
RSn^{3+}	$[RSn(OH)]^{2+}$, $[RSn(OH)_2]^{+}$, $[RSn(OH)_3]^{0}$, $[RSn(OH)_4]^{-}$, $[(RSn)_2(OH)_5]^{+}$
R_2Sn^{2+}	$[(R_2Sn(OH)]^{+}$, $[R_2Sn(OH)_2]^{0}$, $[R_2Sn(OH)_3]^{-}$, $[(R_2Sn)_2(OH)_2]^{2+}$, $[(R_2Sn)_2(OH)_3]^{+}$
R_3Sn+	$[R_3Sn(OH)]^{0}$, $[R_3Sn(OH)_2]^{-}$

The transition between the rapid and slow extraction phases observed mathematically can be elucidated through the physical mechanism illustrated in Fig. 8. In the initial stage (fast regime), the solutes (indicated as red dots) are concentrated on the particle surface or near the pore openings, making them highly accessible to the solvent. This is represented by the bold black arrows in the schematic, indicating the dominance of the surface reaction mechanism with high rate constants (k) during the first 120 minutes.

As the process continues, it enters the final stage (slow regime), where the remaining solutes are located deep within the solid matrix or trapped within internal structures. This phenomenon is depicted by the thin, wavy arrows, symbolizing resistance from film diffusion and intraparticle diffusion.

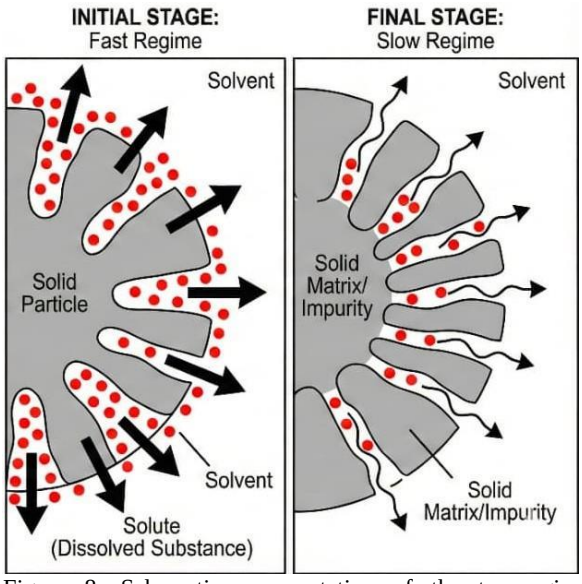

Figure 8. Schematic representation of the two-regime extraction mechanism for DMT by-product

The superior fit of the second-order kinetic model (lower RMSE) at this stage reinforces the evidence that the extraction rate is limited by physical mass transfer barriers of the solute from the matrix to the solvent, rather than simple dissolution. Furthermore, the stability of DMT and MMT species under strongly acidic conditions (pH 0.81-1.65) ensures that the illustrated diffusion pathways remain focused on the mass transfer of halide species without interference from hydrolysis products.

4. CONCLUSION

This study demonstrates that solvent polarity and agitation intensity play a critical role in governing tin extraction from DMT (dimethyltin dichloride) by-products. Water preferentially enhances inorganic tin dissolution, whereas methanol favors the extraction of organotin species. The extraction kinetics consistently follow a pseudo-second-order model, with nonlinear regression providing more reliable kinetic parameters than linear fitting. The distinction between short-time surface-controlled

and long-time diffusion-controlled regimes further strengthens the mechanistic interpretation of the extraction process.

Theoretically, this work refines the kinetic modeling of organotin residues by validating a regime-based analysis over traditional single-regime interpretations. Overall, optimizing these conditions significantly improves tin recovery, highlighting the potential of DMT by-products as viable secondary resources. Future research should explore temperature-dependent kinetics and advanced speciation analysis to further optimize industrial-scale recovery technologies.

ACKNOWLEDGEMENT

We gratefully acknowledge PT Timah Industri for research funding support through "Kegiatan kerja sama penelitian PT Timah Industri – Untirta" (No. 006/TI/SPK-2000/2024-S0 and 840/UN43/HK.06.00/2024.

REFERENCES

[1] L. O. Arham, "Studi perolehan kembali timah dari produk samping kerak reaktor pembuatan organotin asal PT Timah Industri dengan metode pelindian menggunakan asam sulfat dan electrowinning," Tesis, *Institut Teknologi Bandung*, Bandung, Indonesia, 2018.

[2] Fisher Scientific, "Dimethyltin dichloride", fishersci.fi, 2025. [Online]. Available: https://www.fishersci.fi/shop/products/dimethyltin-dichloride-thermo-scientific/11364829. [Accessed: Dec. 10, 2025].

[3] Fisher Scientific, "Methyltin trichloride, 97%, Thermo Scientific Chemicals", fishersci.com, 2025. [Online]. Available: https://www.fishersci.com/shop/products/methyltin-trichloride-97-thermo-scientific/AA7115603. [Accessed: Dec. 10, 2025].

[4] Fisher Scientific, "Tin (II) oxide, 99%", fischersci.be, 2025. [Online]. Available: https://www.fishersci.be/shop/products/tin-ii-oxide-99-thermo-scientific/11483498. [Accessed: Dec. 10, 2025].

[5] Fisher Scientific, "Tin (IV) oxide, 99.9% (metals basis)", fischersci.pt, 2025. [Online]. Available: https://www.fishersci.pt/shop/products/tin-iv-oxide-99-9-metals-basis-thermo-scientific/p-4904556. [Accessed: Dec. 10, 2025].

[6] A. J. Tušek, M. Benković, A. B. Cvitanović, D. Valinger, T. Jurina, and J. G. Kljusurić, "Kinetics and thermodynamics of the solid-liquid extraction process of total polyphenols, antioxidants and extraction yield from asteraceae plants," *Ind. Crops Prod.*, vol. 91, pp. 205-214, 2016. DOI: 10.1016/j.indcrop.2016.07.015.

[7] A. M. Kisiela-Czajka and B. Dziejarski, "Linear and non-linear regression analysis for the Adsorption Kinetics of SO2 in a fixed carbon bed reactor-A case study," *Energies (Basel)*, vol. 15, no. 2, 2022. DOI: 10.3390/en15020633.

[8] Satriana, A. Maulida, R. Qardhawi, Y. M. Lubis, R. Moulana, W. A. W. Mustapha, and N. Arpi, "Study of solid–liquid extraction kinetics of oil from dried avocado (Persea Americana) flesh using hexane as a solvent," *International Journal of Technology*, vol. 14, no. 5, pp. 982-992, 2023. DOI: 10.14716/ijtech.v14i5.6370.

[9] P. Hobbi, O. V. Okoro, C. Delporte, H. Alimoradi, D. Podstawczyk, L. Nie, K. V. Bernaerts, and A. Shavandi, "Kinetic modelling of the solid–liquid extraction process of polyphenolic compounds from apple pomace: influence of solvent composition and temperature," *Bioresour Bioprocess*, vol. 8, no. 1, 2021. DOI: 10.1186/s40643-021-00465-4.

[10] Y.S. Ho and G. McKay, "Pseudo second order model for sorption processes," *Process Biochemistry*, vol. 34, pp. 451-465, 1999. DOI: 10.1016/S0032-9592(98)00112-5.

[11] A. F. Arimalala, R. P. Herve, and R. Rafihavanana, "Modeling and kinetics study of avocado oil extraction from Madagascar using different mathematical models," *S. Afr. J. Chem. Eng.*, vol. 41, pp. 93-97, 2022. DOI: 10.1016/j.sajce.2022.05.006.

[12] S. Ahmadi, C. A. Igwegbe, S. Rahdar, and Z. Asadi, "The survey of application of the linear and nonlinear kinetic models for the adsorption of nickel(II) by modified multi-walled carbon nanotubes," *Appl. Water Sci.*, vol. 9, no. 4, Jun. 2019. DOI: 10.1007/s13201-019-0978-9.

[13] M. E. Yulianto, R. D. Nyamiati, and M. Mustikaningrum, "Kinetics modelling of the solid-liquid extraction process of linamarin compounds from cassava leaves assisted by UV-Photobioextractor," in *Materials Today: Proceedings*, Elsevier Ltd, pp. 230-233, 2023. DOI: 10.1016/j.matpr.2023.03.099.

[14] C. Bretti, R. Cigala, and A. Giacalone, "Hydrolysis of organotin compounds at

high concentration," in *Proc. XVIII Italian-Spanish Congress on Thermodynamics of Metal Complexes (SIMEC)*, 2008.

Metalurgi (2024) 3: 141-150

BRIN
BADAN RISET
DAN INOVASI NASIONAL

METALURGI
Majalah Ilmu dan Teknologi
p-ISSN 0126-3188 | e-ISSN 2443-3926
ejurnalmaterialmetalurgi.lipi.go.id

CORROSION BEHAVIOR OF EQUIATOMIC BIO-HIGH ENTROPY ALLOYS CoCrMoMnNb FABRICATED IN MULTIPLE REMELTING PROCESSES

Fendy Rokhmanto[a, b, *], Aprilia Erryani[a, b], Albertus Deny Heri Setyawan[b], Yudi Nugraha Thaha[b], Ahmad Zakiyuddin[a], Ika Kartika[b], Sri Harjanto[a,*]

[a]Department of Metallurgical and Materials Engineering, University of Indonesia
Kampus UI, Kukusan, Depok, Indonesia 16424
[b]Research Center for Metallurgy, National Research and Innovation Agency (BRIN)
B.J. Habibie Sains and Technology Area, Banten, Indonesia 15314
*E-mail: fend001@brin.go.id; sri.harjanto@ui.ac.id

Received: 27-10-2025, Revised: 05-01-2026, Accepted: 07-01-2026

Abstract

High-entropy alloys are described as equiatomic alloys of more than five elements or materials with five or more element constituents with a high mixing entropy (ΔSmix ≥ 1.5R), where the composition of the element is 5–35%, respectively. One application of HEA (high entropy alloys) materials is in the orthopedic field, where they are developed as biomaterials. Behavior, the correlation between the elemental distribution, and the microstructure of the material were investigated during multiple remelting processes known as Bio-HEAs. The development of Bio-HEAs is exciting in terms of design material, fabrication, and their properties. In this paper, the corrosion behavior and the correlation of the elemental distribution and the microstructure of the material were investigated during the multiple remelting process. The equiatomic CoCrMoMnNb was prepared in vacuum arc melting under an argon atmosphere and melted in a water-cooled copper mold. The total amount of ingot was approximately 25 grams, then flipped and remelted several times, 4, 8, and 12 cycles. The final composition of the alloys was confirmed by EDX (energy dispersive x-ray spectroscopy). The microstructure was investigated with an optical microscope and the SEM (scanning electron microscope). The corrosion parameter occurred in Hank's solution at 37°C, at a scan rate of 1 mV/s. The CCM-MnNb fabricated with 8 cycles of the remelting process exhibits the lowest corrosion rate (0.0038 mmpy) and donor densities (2.67 × 10^{19} cm^{-3}), while the charge transfer resistance number is the highest (18250.94 Ω cm^{-2}). The outstanding corrosion resistance of the alloys is induced by the presence of the finer dendrites and the chromium oxide (Cr_2O_3) protective layer on the alloy's surface.

Keywords: *High entropy alloy, bio-HEA, CoCrMo, biomaterial, remelting cycles, corrosion resistance*

1. INTRODUCTION

High entropy alloys (HEA) are described as equiatomic alloys of more than five elements or materials with five or more element constituents with a high mixing entropy (ΔSmix ≥ 1.5R), and the composition of the element is 5-35%, respectively [1]-[4]. The high entropy alloy material was introduced in 2004. Brian Cantor developed the equiatomic CrMnFeCoNi [5], and then, nowadays, known as the Cantor alloy. In its development up to 2016, 408 types of alloys with various applications have been obtained, which were then classified by D. B. Miracle and O. N. Senkov into 7 groups, that called as a taxonomy of HEA, there are: 3d transition HEA (Al, Co, Cr, Cu, Fe, Mn, Ni, Ti, V), Refractory HEA (Cr, Hf, Mo, Nb, Ta, Ti, V, W, Zr), Light metal HEA (Al, Be, Li, Mg, Sc, Si, Sn, Ti, Zn), Lanthanide (4f) transition metal HEA (Dy, Gd, Lu, Tb Tm, Y), Brass and bronze HEA (Al, Cu, Mn, Ni, Sn, Zn), Precious metal HEA (Ag, Au, Co, Cr, Cu, Ni, Pd,

DOI: 10.55981/metalurgi.2024.782

Metalurgi is Sinta 2 Journal (https://sinta.kemdikbud.go.id/journals/profile/3708) accredited by Ministry of Education, Culture, Research, and Technology, Republic Indonesia

Pt, Rh, Ru), and Interstitial compound HEA (with B, C, or N addition on the 3d HEA) [3].

One of the applications of HEA material is in the orthopedic field; the HEA material, which is developed as a biomaterial, is then known as Bio-HEAs. Bio-HEAs were introduced by Mitsuharu Todai et al. [6] and Shao Ping Wang et al. [7] in 2017, they developed equiatomic TiNbTaZrMo. In its development, the TiNbTaZrMo, TiZrHfNbTa, TiZrHfNbTaMo, TiZrHfCrMo, TiZrHfCoCrMo, and TiZrNbTaFe were introduced as Bio-HEA [6]-[17], Takeshi Nagase et al. [18] Introduced "CCM base Bio-HEA" in 2019, the alloys are CoCrMoFeMn, CoCrMoFeMnW, and CoCrMoFeMnWAg . Alina Elena Bololoi et al. [19] introduced CoCrMoNbTi as a CCM base Bio-HEA in 2023 by powder metallurgy process. Meanwhile, in 2017, Mina Zhang et al. [20] developed CoCrMoNbTi as a refractory HEA, the composition ratio of CoCrMo is more than 50%, so it can be classified as a CCM base Bio-HEA.

The development of Bio-HEAs is exciting both in terms of design material, fabrication, and their properties. The material design must follow several rules; the entropy is more than 12.471 J/K mol ($\Delta Smix \geq 1.5R$), the enthalpy is $-20 \leq \Delta Hmix \leq 5$ KJ/mol, the delta (δ) parameter is less than ≤ 6.6, the omega (Ω) parameter is greater than ≥ 1.1 [3], that mathematically can be described with the following equation:

$$\Delta Smix = -R \sum_{i=1}^{n} xilnxi \quad (1)$$

$$\Delta Hmix = \sum_{i=1,\, i\neq j}^{n} 4\Delta Hij xixj \quad (2)$$

$$\delta = 100\sqrt{\sum_{i=1}^{n} xi\left(1-\frac{ri}{\bar{r}}\right)^2} \quad (3)$$

$$\Omega = \left|\frac{Tm\,\Delta Smix}{\Delta Hmix}\right| \quad (4)$$

$$Tm = \sum_{i=1}^{n} xi(Tm)i \quad (5)$$

Where the ΔHij is the mixing enthalpy of two elements, ri is the atomic radius of the element, $\hat{r}$ is the average atomic radius of the alloy, and Tm is the melting temperature.

The biocompatibility of the Bio-HEA became crucial during material design. Biocompatibility can be analyzed by studying corrosion behavior in the simulated body fluids. Recently, the fabrication of Bio-HEAs has been dominated by the casting process in the vacuum arc melting furnace [6]-[7],[9],[13],[15],[17]-[18],[20], where the ingots are melted several times to improve the homogeneity of the alloying elements that relate to the mechanical properties and corrosion resistance of the alloys. The remelting cycles vary; several of them are remelted from 5 to 10 times, and most are remelted more than 10 times, though specific numbers are not stated. Based on that data, it is not possible to determine the optimal cycle times of the remelting process.

However, despite the application of multiple remelting cycles in Bio-HEA fabrication being commonly used, the influence of the number of remelting cycles on microstructure uniformity and corrosion resistance has not been systematically evaluated. Therefore, in this paper, the correlation of the corrosion behavior, elemental distribution, and microstructure of the material will be investigated during the multiple remelting processes. The developed material is equiatomic CCM base Bio-HEA CoCrMoMnNb, which refers to the traditional CoCrMo implant material, which is one of the biomaterials with good corrosion resistance and high wear resistance, making it suitable for orthopedic implants.

2. MATERIALS AND METHODS

The equiatomic CoCrMoMnNb, constructed according to the high entropy alloys rules in equations 1–5, has ΔSmix: 13.38 J/K mol, ΔHmix: -8.64 J/K mol, Ω: 3.19, δ: 5.94, and Tm: 2060.8 K. The ingot was prepared in vacuum arc melting under an argon atmosphere; the raw material, cobalt and chromium lumps, molybdenum and titanium rods, and manganese flakes (99.9%) were melted in a water-cooled copper mold. The total amount of ingot was approximately 25 grams, then flipped and remelted several times, 4, 8, and 12 cycles. The final composition and microstructure of the ingots were examined by EDX (energy-dispersive x-ray spectroscopy) and SEM (scanning electron microscopy) JEOL 6390A, respectively. Samples were prepared with methanol, 10% HCl, and electroetched after polishing with alumina. The corrosion characteristics were evaluated by potentiodynamic polarization and EIS (electrochemical impedance spectroscopy) using an Autolab 302 Multi BA electrochemical working station with Hank's solution at 37 °C and a scan rate of 1 mV/s. The samples were prepared in a 1 cm^2 area and then sanded up to 1200-grade sandpaper.

3. RESULTS AND DISCUSSION

Table 1 presents the high entropy alloys parameter of the CCM-MnNb; the mixing entropy of the alloys in the various remelting processes is above 1.5R.

Table 1. High entropy alloy parameter after alloying

	ΔSmix (J/K mol)	ΔHmix (J/K mol)	Ω	δ	ρ	Tm (K)
MnNb 4	13.21	-9.04	3.16	5.39	8.46	2161.91
MnNb 8	12.96	-9.84	3.01	5.54	8.65	2288.73
MnNb 12	12.76	-10.48	2.82	5.53	8.75	2312.17

The data in Table 1 indicates that the CCM-MnNb alloys were still categorized as high entropy alloy material, although the presence of Mn increased up to 6.7% in the 12 cycle times, as shown in Table 2.

Table 2. SEM EDX composition after alloying (at. %)

	Co	Cr	Mo	Mn	Nb
MnNb 4	26.46 ± 1.2	22.80 ± 0.7	14.22 ± 2.4	18.31 ± 1.4	18.21 ± 2.9
MnNb 8	25.02 ± 3.5	24.16 ± 1.2	21.05 ± 6.3	9.12 ± 2.1	20.80 ± 2.1
MnNb 12	26.79 ± 4.9	21.4 1± 1.8	24.15 ± 7.8	6.70 ± 1.1	20.95 ± 1.8

Table 2 presents the average chemical composition (at. %) of the various spots on the matrix and dendritic area of the CCM-MnNb button ingot with EDX characterization. The data in Table 2 shows that the remelting process decreases manganese (Mn) concentration from 20% (at. %) to 18.31% in 4 cycle times, 9.12% in 8 cycle times, and 6.7% in 12 cycle times. The Mn loss during the remelting process is caused by the volatilization behavior of manganese, where the higher melting temperature and longer processing time will increase manganese volatization [21].

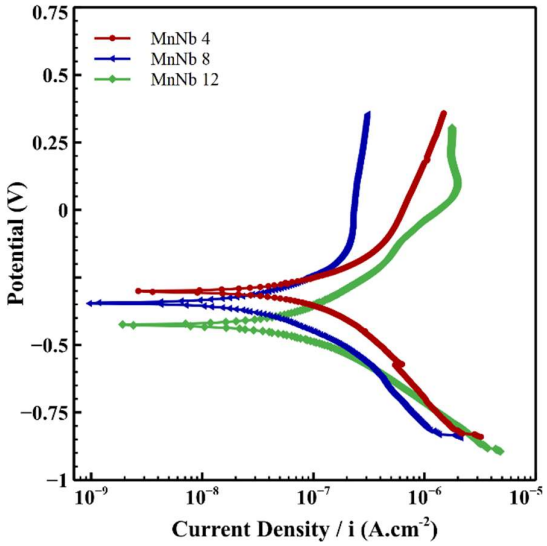

Figure 1. Tafel polarization curve of equiatomic CCM-MnNb, recorded at a scan rate of 1 mV/s, immersed in Hank's at 37 °C

The cycle of the remelting process induced the corrosion behavior of CCM-MnNb, as indicated by the shifting of the Tafel polarization curve of CCM-MnNb in Fig. 1. Meanwhile, Table 3 presents the potentiodynamic parameters of CCM-MnNb: corrosion current density, corrosion potential, and corrosion rate, which were calculated by Tafel extrapolation and included several biomaterials and Bio-HEAs (316L SS, CCM F75, TiAlV, and Bio-HEA TiZrNbTaMo).

Figure 1 shows that the corrosion potential shifts down up to -426 mV and the current density shifts left up to 0.94 µA/cm² after 12 cycles of remelting. A bigger current density indicates that the alloys are more corroded, which means they have weak corrosion resistance. In Table 3, the corrosion rate of CCM-MnNb 12 (0.0058 mmpy) is bigger than the others, CCM-MnNb 4 (0.0051 mmpy) and CCM-MnNb 8 (0.0038 mmpy). Compared to traditional biomaterials, Bio-HEAs have higher corrosion resistance, as shown in Table 3. The Titanium Bio-HEA TiZrNbTaMo has a lower corrosion current density than the Ti6Al4V. The CCM-MnNb 8 has a lower corrosion rate and a current density than CoCrMo F75, although it is higher than that of Titanium Bio-HEA.

Table 3. Potentiodynamic parameters of various alloys, immersed in Hank's at 37 °C

Alloys	i_{corr} (µA/cm²)	E_{corr} (mV)	Corr. Rate (mmpy)	Reff
316L SS	1.384	- 373	0.0109	[22]
CoCrMo F75	0.768	- 660	0.0061	[22]
Ti6Al4V	0.07	- 325	-	[23]
Bio-HEA TiZrNbTaMo	0.08	- 660	-	[23]
MnNb 4	0.828	- 302.28	0.0051	Present work
MnNb 8	0.619	- 345.88	0.0038	Present work
MnNb 12	0.940	- 426.22	0.0058	Present work

In this study, the CCM-MnNb 8 has a lower corrosion rate and a current density, which means it has higher corrosion resistance than others, even including the traditional CCM biomaterial (CoCrMo F75). The high corrosion resistance performance of CCM-MnNb alloys is related to the homogeneity of the elemental distribution, which is shown in the EDX characterizations in Figs. 2 and 3.

Figure 2 presents the EDX mapping of the alloys, while Fig. 3 shows the chemical composition of the CCM-MnNb matrix, as investigated using EDX point characterization. Figures 2 and 3 show that the matrix of CCM-MnNb dominates with cobalt, chromium, and manganese, even though molybdenum and niobium were also present. Meanwhile, the dendritic arm is rich in molybdenum and niobium, where it is typically an HEA material; the elements with high melting temperatures dominate in the dendritic arms [6]-[7].

Figure 2(a) shows the EDX mapping of the 4-cycle remelting process; the dendritic region appears dominated by Mo and Nb, while the other elements are widely spread on the matrix. Figure

3(a) reveals the dominance of Co (28.1%), Cr (23.4%), and Mn (19.9%). Whereas, the chromium induced the formation of a protective chromium oxide (Cr_2O_3) layer on the surface of Co-Cr alloys, which can protect from chloride ion attack [24]-[26]. Figure 2(b) reveals the EDX mapping of the 8-cycle remelting process, where the Co matrix is rich in Cr (25.7%), Mo (13.2%), and Nb (20.9%), as shown in Fig. 3(b), which enhances corrosion resistance. Mo and Nb are well known to have good compatibility [27]-[28], which can enhance the protection from chloride ion attack. Meanwhile, the Nb enrichment on the matrix is induced by the volatilization of Mn, where it decreases to 11.4% as shown in Fig. 3(b).

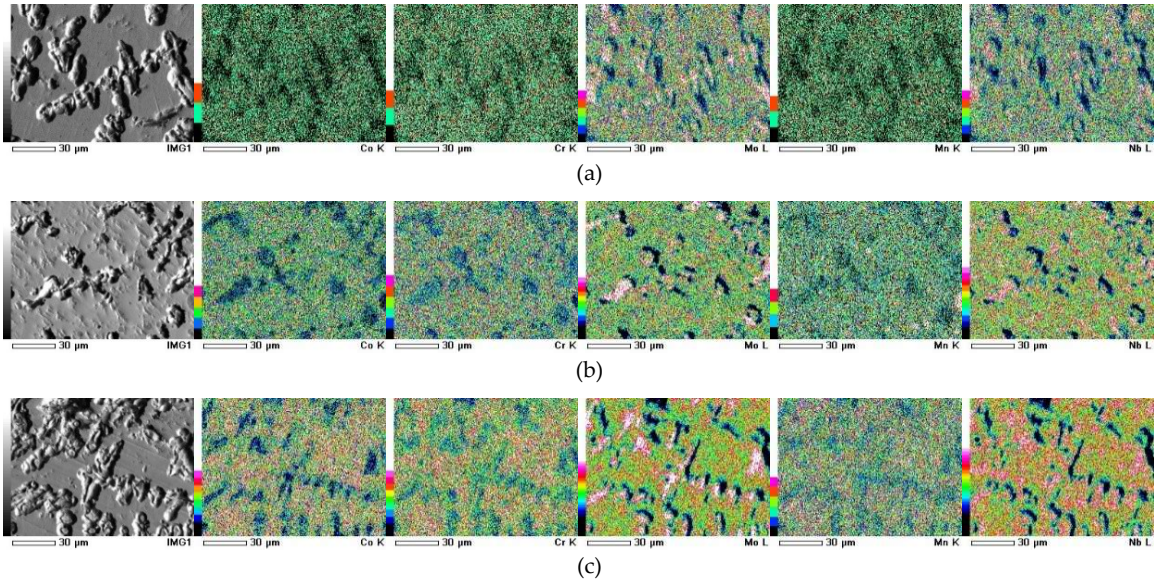

Figure 2. EDX – mapping image of equiatomic CCM-MnNb; (a) MnNb 4, (b) MnNb 8, (c) MnNb 12

Figure 2(c) shows the EDX mapping of the 12-cycle remelting process; the dendrite structure is observable and rich in Mo and Nb, and the Mn concentration decreased up to 7.16% as shown in Fig. 3(c). The Mn volatilization enhanced the homogeneous distribution of Nb (26.5%) in the matrix along with Co (31.5). The decrease of Mo (11.8%) and Cr (23.2%) content, as shown in Fig. 3(c), induces a lack of a Cr_2O_3 passive layer, which decreases the corrosion resistance, resulting in the highest corrosion rate (0.0058 mmpy).

CCM-MnNb 8 has the highest charge transfer resistance, as shown in the Nyquist plot in Fig. 4(a), which indicates that the alloys are strongly covered by a thin passive layer, which is Cr_2O_3 that protects from corrosion attack. CCM-MnNb 8 is also a higher impedance, as shown in Fig. 4(b). The Bode modulus plots show that in the high-frequency region (> 100 Hz), the $|Z|$ tends to remain constant and independent of frequency, and the low-frequency region has a linear relation with the impedance value, which means that the alloy has good protection from corrosion, which is chloride ion attack. Figure 4(c) is the Bode phase plot; the high and wide phase angle indicates the ideal capacitive behavior of alloys, and the CCM-MnNb has the biggest, which clarifies that the alloy has the best corrosion resistance.

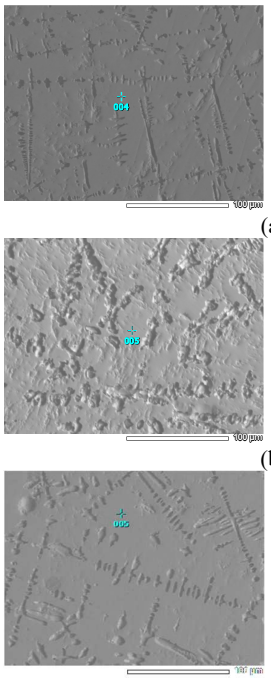

(a)

Element	Atomic %
Co	28.07
Cr	23.37
Mo	13.71
Mn	19.93
Nb	14.92

(b)

Element	Atomic %
Co	28.78
Cr	25.69
Mo	13.22
Mn	11.4
Nb	20.91

(c)

Element	Atomic %
Co	31.46
Cr	23.16
Mo	11.76
Mn	7.16
Nb	26.46

Figure 3. EDX – point Image of equiatomic CCM-MnNb; (a) MnNb 4, (b) MnNb 8, (c) MnNb 12

Figure 4(d) is the equivalent circuit model that was constructed based on the fitting result of impedance, and Table 4 is the fitting parameters of the equivalent circuit. The highest Rct (charge transfer resistance) on the CCM-MnNb indicates that the ion transfer between the alloy surface and the Hank's solution became tougher, which means the alloy has good corrosion resistance.

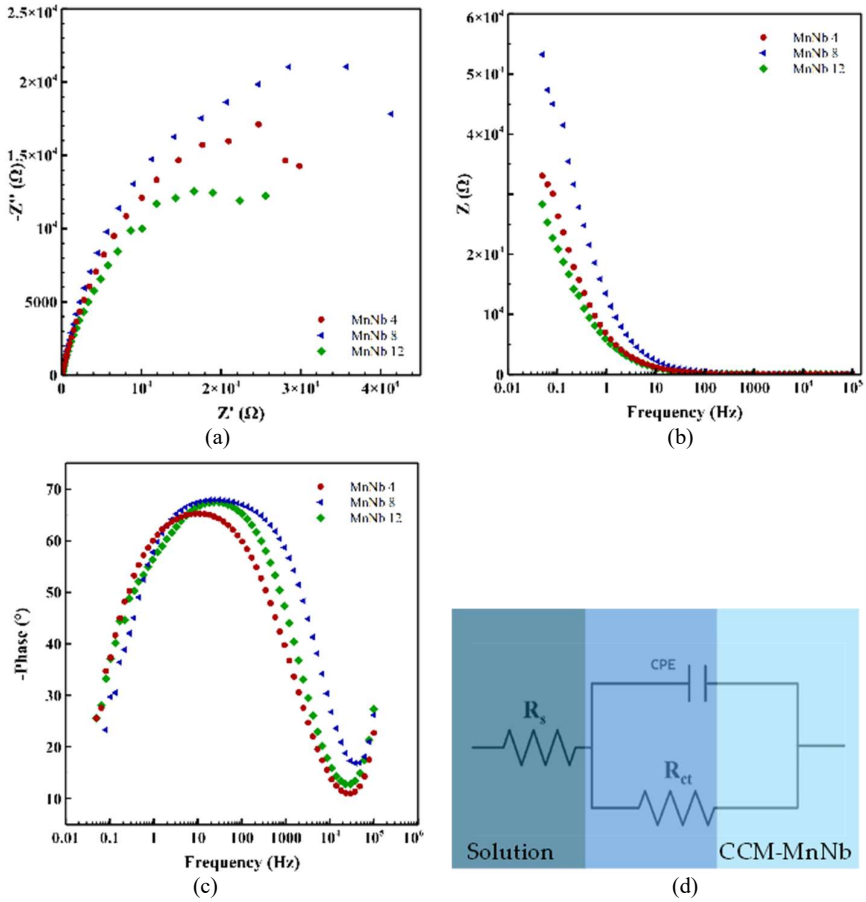

Figure 4. EIS curve of equiatomic CCM-MnNb, recorded at scan rate 1 mV/s, immersed in Hank's at 37 °C

Fig. 5 shows the Mott-Schottky plots of the CCM-MnNb alloys with different remelting cycles. The Mott-Schottky plots exhibit a positive slope; it is present that these alloys exhibit n-type semiconductive behavior. The donor densities (Nd) were approximately 3.93×10^{19} cm^{-3} (MnNb 4), 2.67×10^{19} cm^{-3} (MnNb 8), and 5.5×10^{19} cm^{-3} (MnNb 12). CCM-MnNb 8 has the lowest donor density, indicating lots of oxygen vacancies and other donor-type defects in the film structure, which means the alloys have good corrosion resistance.

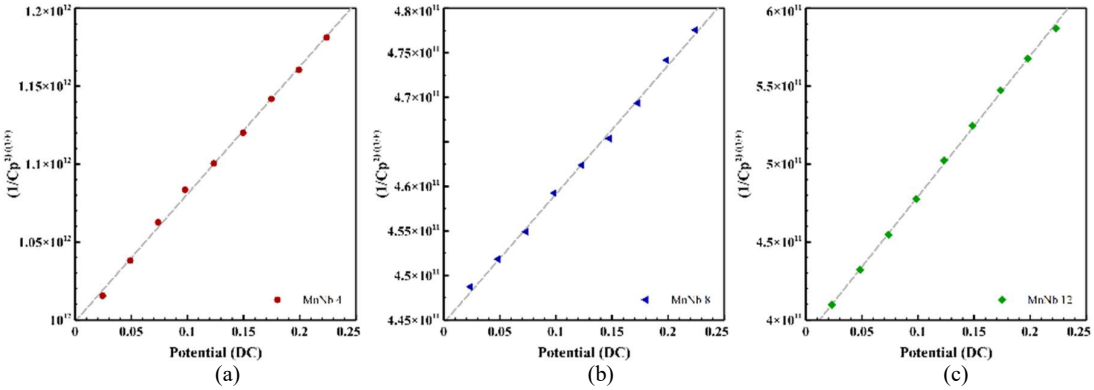

Figure 5. Mott–Schottky curve of equiatomic CCM-MnNb recorded at scan rate 1 mV/s, immersed in Hank's at 37 °C

Mn losses also affect the microstructure of CCM-MnNb, as shown in Fig. 6. The dendritic structure changed during the cycle of the remelting process. The dendrite formation in the 12-cycle remelting process is more widely distributed than in the 4- and 8-cycle processes. Besides that, the Mn losses also induce the segregation of niobium (Nb) and molybdenum (Mo) in the dendritic arm, which is indicated by the bright white area (Fig. 2). The form of dendrites in the CCM-MnNb 8 is short and tiny; it may prevent corrosion formation in the interface of the matrix and dendrite, so that it enhances the corrosion resistance of the alloys.

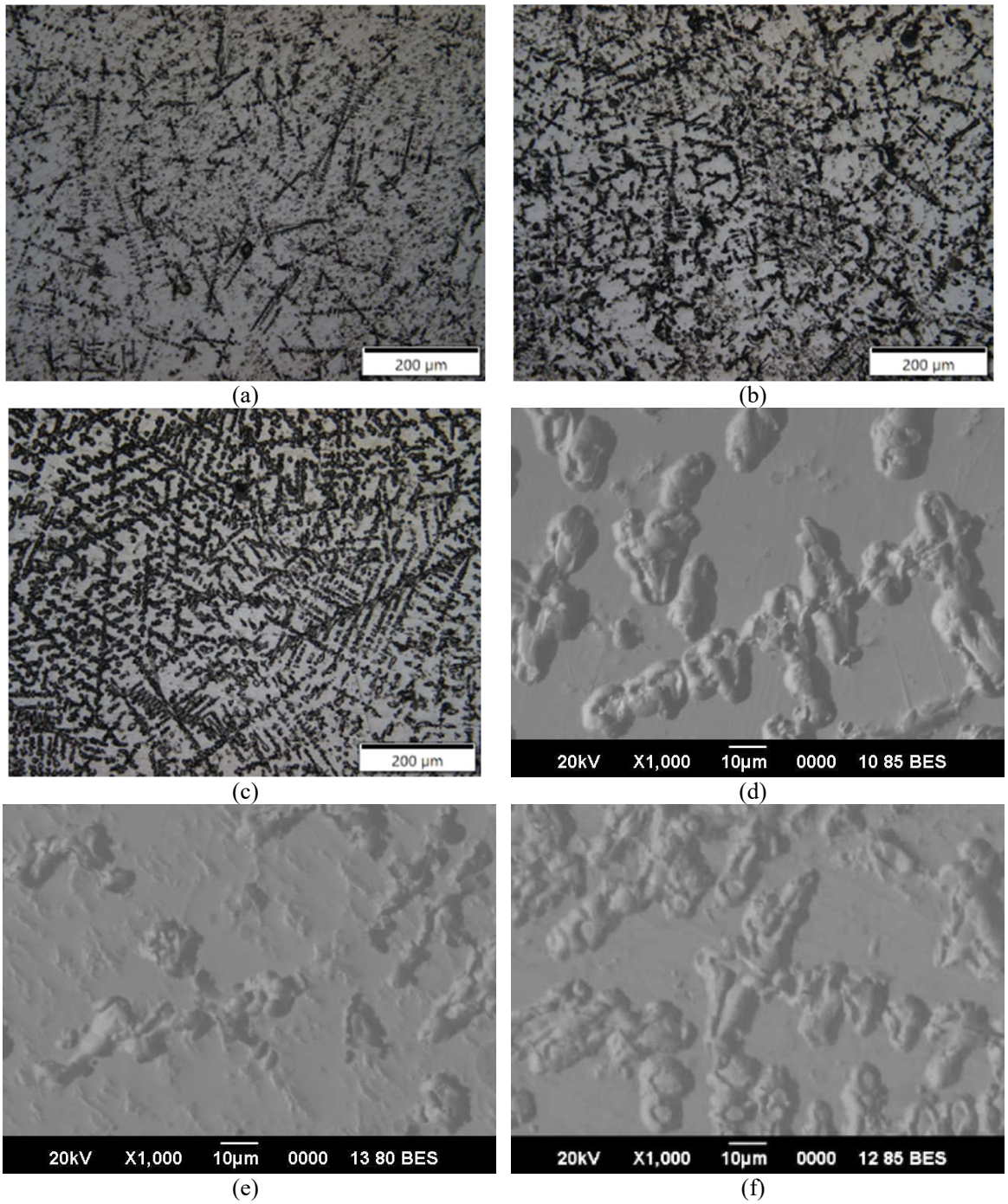

Figure 6. Microstructure of equiatomic CCM-MnNb: Optical microscope image of (a) MnNb 4, (b) MnNb 8, (c) MnNb 12; SEM-BSE image of (d) MnNb 4, (e) MnNb 8, (f) MnNb 12

The short and tiny dendrites formation in CCM-MnNb 8 induced the homogeneity of the microstructure, which significantly reduced the electrochemical potential difference between the dendrites (cathode-Mo rich) and the matrix (anode). The finer dendrite formation also reduces the surface area of the micro cathode, which can inhibit the rate of anodic solution, as confirmed by the low current density (0.619 μA/cm^2), as shown in Table 3. In addition, the finer microstructure also induced the stability of Cr_2O_3 passive film formation on the matrix surface, as indicated by the lowest donor density (2.67 × 10^{19} cm^{-3}) and highest charge transfer resistance (18,250.94 Ω/cm2) on the CCM-MnNb 8, as shown in Table 4. Comprehensively, it can prevent localized corrosion, such as pitting corrosion in the alloys, which promotes the CCM-MnNb 8 to have outstanding corrosion resistance.

Table 4. The fitting parameters of the equivalent circuit model for EIS data fitting of the CCM-MnNb alloy

	R_s	R_{ct}	Q	
	(Ω cm^{-2})	(Ω cm^{-2})	Y_0 (μFcm^{-2})	N
MnNb 4	8.94	15094.83	1.09E-05	0.23325
MnNb 8	4.91	18250.94	5.17E-06	0.24134
MnNb 12	4.54	9479.40	1.08E-05	0.21461

4. CONCLUSION

The corrosion behavior of equiatomic Bio-HEA CCM-MnNb that was fabricated through multiple remelting (4, 8, and 12 cycles) processes was investigated. The remelting process decreases Mn concentration from 20% (at. %) to 18.31% in 4 cycle times, 9.12% in 8 cycle times, and 6.7% in 12 cycle times, which is related to the homogeneity of the elemental distribution of the alloys. Furthermore, the CCM-MnNb 8 was fabricated using 8 cycles, resulting in the lowest corrosion rate (0.0038 mmpy), followed by CCM-MnNb 4 (0.0051 mmpy) and CCM-MnNb 12 (0.0053 mmpy), as well as the number of donor densities, 2.67 × 10^{19} cm^{-3}, 3.93 × 10^{19} cm^{-3}, and 5.5 × 10^{19} cm^{-3}, respectively. Nevertheless, it contrasts with the charge transfer resistance (Rct), the CCM-MnNb 8 has the highest number of 18250.94 Ω cm^{-2}, then CCM-MnNb 4 (15094.83 Ω cm^{-2}) and CCM-MnNb 12 (9479.4 Ω cm^{-2}). The CCM-MnNb 8 leads in corrosion resistance among the other equiatomic Bio-HEAs, which is attributed to the presence of the finer dendrites and the chromium oxide (Cr_2O_3) protective layer on the alloy's surface.

ACKNOWLEDGEMENT

This work was supported by the National Research and Innovation Agency (BRIN) through the Rumah Program Research Grant of Nanotechnology and Materials Research Organization (grant number 20/III.10/HK/2024). This work was also part of the Degree by Research (DbR) Program of the National Research and Innovation Agency (BRIN) of the Republic of Indonesia.

REFERENCES

[1] E. J. Pickering and N. G. Jones, "High-entropy alloys: a critical assessment of their founding principles and future prospects," *International Materials Reviews*, vol. 61, no. 3, pp. 183-202, 2016. DOI: 10.1080/09506608.2016.1180020.

[2] O. N. Senkov and D. B. Miracle, "A new thermodynamic parameter to predict formation of solid solution or intermetallic phases in high entropy alloys," *Journal of Alloys and Compounds*, vol. 658, pp. 603-607, 2016. DOI: 10.1016/j.jallcom.2015.10.279.

[3] D. B. Miracle and O. N. Senkov, "A critical review of high entropy alloys and related concepts," *Acta Materialia*, vol. 122, pp. 448-511, 2017. DOI: 10.1016/j.actamat.2016.08.081.

[4] P. Martin, C. E. Madrid-Cortes, C. Cáceres, N. Araya, C. Aguilar, and J. M. Cabrera, "HEAPS: A user-friendly tool for the design and exploration of high-entropy alloys based on semi-empirical parameters," *Computer Physics Communications*, vol. 278, p. 108398, 2022. DOI: 10.1016/j.cpc.2022.108398.

[5] B. Cantor, I. T. H. Chang, P. Knight, and A. J. B. Vincent, "Microstructural development in equiatomic multicomponent alloys," *Materials Science and Engineering: A*, vol. 375-377, no. 1-2 SPEC. ISS., pp. 213-218, 2004. DOI: 10.1016/j.msea.2003.10.257.

[6] M. Todai, T. Nagase, T. Hori, A. Matsugaki, A. Sekita, and T. Nakano, "Novel TiNbTaZrMo high-entropy alloys for metallic biomaterials," *Scripta Materialia*, vol. 129, pp. 65-68, 2017. DOI: 10.1016/j.scriptamat.2016.10.028.

[7] S. P. Wang and J. Xu, "TiZrNbTaMo high-entropy alloy designed for orthopedic implants: As-cast microstructure and mechanical properties," *Materials Science and*

DOI: 10.55981/metalurgi.2024.782

Engineering C, vol. 73, pp. 80-89, 2017. DOI: 10.1016/j.msec.2016.12.057.

[8] G. Popescu, B. Ghiban, C. A. Popescu, L. Rosu, R. Truscă, I. Carcea, V. Soare, D. Dumitrescu, I. Constantin, M. T. Olaru, and B. A. Carlan, "New TiZrNbTaFe high entropy alloy used for medical applications," *IOP Conference Series: Materials Science and Engineering*, vol. 400, no. 2, 2018. DOI: 10.1088/1757-899X/400/2/022049.

[9] T. Nagase, M. Todai, T. Hori, and T. Nakano, "Microstructure of equiatomic and non-equiatomic Ti-Nb-Ta-Zr-Mo high-entropy alloys for metallic biomaterials," *Journal of Alloys and Compounds*, vol. 753, pp. 412-421, 2018. DOI: 10.1016/j.jallcom.2018.04.082.

[10] A. Motallebzadeh, N. S. Peighambardoust, S. Sheikh, H. Murakami, S. Guo, and D. Canadinc, "Microstructural, mechanical and electrochemical characterization of TiZrTaHfNb and Ti1.5ZrTa0.5Hf0.5Nb0.5 refractory high-entropy alloys for biomedical applications," *Intermetallics*, vol. 113, p. 106572, 2019. DOI: 10.1016/j.intermet.2019.106572.

[11] T. Hori, T. Nagase, M. Todai, A. Matsugaki, and T. Nakano, "Development of non-equiatomic Ti-Nb-Ta-Zr-Mo high-entropy alloys for metallic biomaterials," *Scripta Materialia*, vol. 172, pp. 83-87, 2019. DOI: 10.1016/j.scriptamat.2019.07.011.

[12] Y. Yuan, Y. Wu, Z. Yang, X. Liang, Z. Lei, H. Huang, H. Wang, X. Liu, Ke An, and W. Wu, Z. Lu., "Formation, structure and properties of biocompatible TiZrHfNbTa high-entropy alloys," *Materials Research Letters*, vol. 7, no. 6, pp. 225-231, 2019. DOI: 10.1080/21663831.2019.1584592.

[13] T. Nagase, Y. Iijima, A. Matsugaki, K. Ameyama, and T. Nakano, "Design and fabrication of Ti–Zr-Hf-Cr-Mo and Ti-Zr-Hf-Co-Cr-Mo high-entropy alloys as metallic biomaterials," *Materials Science and Engineering C*, vol. 107, p. 110322, 2020. DOI: 10.1016/j.msec.2019.110322.

[14] J. González-Masís, J. M. Cubero-Sesin, A. Campos-Quirós, and K. Edalati, "Synthesis of biocompatible high-entropy alloy TiNbZrTaHf by high-pressure torsion," *Materials Science and Engineering: A*, vol. 825, 2021. DOI: 10.1016/j.msea.2021.141869.

[15] N. Hua, W. Wang, Q. Wang, Y. Ye, S. Lin, L. Zhang, Q. Guo, J. Brechtl, P. K. Liaw, "Mechanical, corrosion, and wear properties of biomedical Ti-Zr-Nb-Ta-Mo high entropy alloys," *Journal of Alloys and Compounds*, vol. 861, 2021. DOI: 10.1016/j.jallcom.2020.157997.

[16] T. Ishimoto, R. Ozasa, K. Nakano, M. Weinmann, C. Schnitter, M. Stenzel, A. Matsugaki, T. Nagase, T. Matsuzaka, and M. Todai, H. S. Kim, T. Nakano, "Development of TiNbTaZrMo bio-high entropy alloy (BioHEA) super-solid solution by selective laser melting, and its improved mechanical property and biocompatibility," *Scripta Materialia*, vol. 194, 2021. DOI: 10.1016/j.scriptamat.2020.113658.

[17] Y. Iijima, T. Nagase, A. Matsugaki, P. Wang, K. Ameyama, and T. Nakano, "Design and development of Ti-Zr-Hf-Nb-Ta-Mo high-entropy alloys for metallic biomaterials," *Materials and Design*, vol. 202, p. 109548, 2021. DOI: 10.1016/j.matdes.2021.109548.

[18] T. Nagase, M. Todai, and T. Nakano, "Development of Co - Cr - Mo - Fe - Mn - W and Co - Cr - Mo - Fe - Mn - W - Ag high- entropy alloys based on Co - Cr - Mo Alloys," *Materials Transactions*, vol. 61, no. 4, pp. 567-576, 2020. DOI: 10.2320/matertrans.MT-MK2019002.

[19] A. E. Bololoi, L. E. Geambazu, I. V. Antoniac, R. V. Bololoi, C. A. Manea, V. D. Cojocaru, and D. Pătroi, "Solid-state processing of CoCrMoNbTi High-entropy alloy for biomedical applications," *Materials*, vol. 16, no. 19, pp. 1-12, 2023. DOI: 10.3390/ma16196520.

[20] M. Zhang, X. Zhou, and J. Li, "Microstructure and mechanical properties of a refractory CoCrMoNbTi high-entropy alloy," *Journal of Materials Engineering and Performance*, vol. 26, no. 8, pp. 3657-3665, 2017. DOI: 10.1007/s11665-017-2799-z.

[21] F. J. Lan, C. L. Zhuang, C. R. Li, J. B. Chen, G. K. Yang, and H. J. Yao, "Study on manganese volatilization behavior of Fe-Mn-C-Al twinning-induced plasticity steel," *High Temperature Materials and Processes*, vol. 40, no. 1, pp. 461-470, 2021. DOI: 10.1515/htmp-2021-0049.

[22] Z. Zhou, Q. Wei, Q. Li, B. Jiang, Y. Chen, and Y. Sun, "Development of Co-based bulk metallic glasses as potential

biomaterials," *Materials Science and Engineering C*, vol. 69, pp. 46-51, 2016. DOI: 10.1016/j.msec.2016.05.025.

[23] W. Yang, Y. Liu, S. Pang, P. K. Liaw, and T. Zhang, "Bio-corrosion behavior and in vitro biocompatibility of equimolar TiZrHfNbTa high-entropy alloy," *Intermetallics*, vol. 124, p. 106845, 2020. DOI: 10.1016/j.intermet.2020.106845.

[24] Y. Okazaki, T. Tateishi, and Y. Ito, "Corrosion resistance of implant alloys in pseudo physiological solution and role of alloying elements in passive films," *Materials Transactions, JIM*, vol. 38, no. 1, pp. 78-84, 1997.

[25] A. W. E. Hodgson, S. Kurz, S. Virtanen, V. Fervel, C.-O. Olsson, and S. Mischler, "Passive and transpassive behaviour of CoCrMo in simulated biological solutions," *Electrochimica Acta*, vol. 49, no. 13, pp. 2167-2178, 2004.

[26] A. Ghiban, B. Ghiban, C. M. Bortun, and M. Buzatu, "Structural investigations in CoCrMo (Ti) welded dental alloys," *Rev. Chim. (Bucharest)*, vol. 65, no. 11, pp. 1314-1318, 2014.

[27] D. Kuroda, M. Niinomi, M. Morinaga, Y. Kato, and T. Yashiro, "Design and mechanical properties of new β type titanium alloys for implant materials," *Materials Science and Engineering: A*, vol. 243, no. 1-2, pp. 244-249, 1998. DOI: 10.1016/s0921-5093(97)00808-3.

[28] X. Z. Wang, Q. Hu, L. Zhang, and Z. Cui, "The influence of Nb addition on the passivity of CoCrNiNbx multi-principal element alloys," *Journal of Electroanalytical Chemistry*, vol. 908, 2022. DOI: 10.1016/j.jelechem.2022.116107.

Metalurgi (2024) 3: 151-158

METALURGI
Majalah Ilmu dan Teknologi
p-ISSN 0126-3188 | e-ISSN 2443-3926
ejurnalmaterialmetalurgi.lipi.go.id

INVESTIGATION OF FAILURE MECHANISMS IN U-BEND TUBES OF SHELL-AND-TUBE HEAT EXCHANGERS

Mochamad Achyarsyah[a,*], Kus Hanaldi[a], Wiwik Purwadi[a], Gita Novian Hermana[b], Ari Siswanto[b], Cecep Ruskandi[b], Muhammad Rizki Gorbyandi Nadi[b]

[a]Department of Foundry Engineering, Bandung Polytechnic for Manufacturing
[b]Department of Advanced Materials Engineering, Bandung Polytechnic for Manufacturing
Kanayakan No. 21, Bandung, Jawa Barat, Indonesia 40135
*E-mail: achyarsyah@polman-bandung.ac.id

Received: 110-09-2025, Revised: 05-01-2025, Accepted: 08-01-2026

Abstract

The U-bend tubes of a shell-and-tube heat exchanger made of SA-234 Grade WPB carbon steel failed prematurely within 14 days after replacement and welding. This study investigates failure mechanisms through an integrated failure analysis that includes visual inspection, dye penetrant testing, chemical composition analysis, hardness measurements, and microstructural characterization. The results reveal that the tube contained 0.324 wt.% C, exceeding the maximum limit specified by the standard, which promoted the formation of Widmanstätten ferrite and reduced toughness. The welded joint exhibited multiple defects, including porosity and lack of fusion, which acted as stress concentration sites. Hardness measurements showed average values of 205 HV in the weld metal, 199 HV in the HAZ (heat-affected zone), and 184 HV in the base metal. Under operating conditions of 275 °C and 58.48 barg, these defects progressively opened, leading to fluid leakage. The escaping high-pressure fluid accelerated erosion-corrosion, as evidenced by oxygen-rich corrosion products detected by EDS analysis. The findings demonstrate that the combined effects of material non-compliance, poor welding quality, and unfavorable microstructural evolution governed the premature failure. This study provides quantitative insights to improve welding practices and material selection, thereby enhancing the reliability of U-bend tubes in shell-and-tube heat exchangers.

Keywords: *U-bend tube, failure analysis, heat exchangers, steel, widmanstätten*

1. INTRODUCTION

Shell-and-tube heat exchangers play an essential role in a wide range of industries, including chemical, thermoelectric power generation, oil refining, and mineral processing [1]-[3]. These exchangers are widely used because they reduce energy consumption by transferring heat between fluids at different temperatures. Among the critical components of shell-and-tube heat exchangers, the shell-and-tube themselves are essential for facilitating heat transfer between two fluids; one fluid flows through the tubes, while another fluid flows across the shell side [4].

Failures in shell-and-tube heat exchangers pose significant challenges to the industry, despite regular maintenance being scheduled to prevent such issues. Chemical corrosion, SCC (stress corrosion cracking), and mechanical failures, or a combination of these factors, are the leading causes of failure in shell-and-tube heat exchangers [5]-[8]. Edi Purnomo et al. reported that the failure of the U-bend in the heat exchanger was caused by welding defects and corrosion due to oxygen reactions, exacerbated by cyclic operational stresses [2]. Another study by Rezaei et al. reported that erosion-corrosion, caused by solid particles generated during catalysis, affected the

DOI: 10.55981/metalurgi.2024.775

Metalurgi is Sinta 2 Journal (https://sinta.kemdikbud.go.id/journals/profile/3708) accredited by Ministry of Education, Culture, Research, and Technology, Republic Indonesia

performance of heat exchangers and led to tube failure [9]. Panahi et al. also investigated failures in shell-and-tube heat exchangers caused by crevice corrosion between the external surface of the tubes and the tube sheet [6]. Previous studies reported that welded joints are particularly susceptible to deterioration mechanisms such as pitting corrosion, SCC, and welding defects [10]-[11]. As a result, cracks and other defects may form in the welded joints, potentially leading to failure of the shell-and-tube heat exchanger.

Although numerous investigations have addressed failures in shell-and-tube heat exchangers, most studies focus on individual failure mechanisms in isolation, such as corrosion or welding defects. A systematic correlation between material composition, welding quality, microstructural evolution, and operational conditions, especially in cases of premature failure after repair welding, remains insufficiently explored.

Therefore, this study aims to investigate the root cause of failure at the welded joint on the U-bend tube in a shell-and-tube heat exchanger that failed during operation by correlating material properties, joining processes, microstructural features, and service conditions. Furthermore, this study seeks to establish an integrated failure mechanism, demonstrating that premature failure is governed by the combined effects of material non-compliance, welding-induced defects, and unfavorable microstructural evolution under high-temperature and high-pressure operating conditions. The investigation process involves examining the failed tube and U-bend tube using a combination of visual examination, non-destructive testing, and microstructural observations. By thoroughly evaluating the failed components, identifying material degradation, and analyzing the microstructure, the root cause of failure can be determined.

2. MATERIALS AND METHODS

2.1 Material

The operating conditions on the tube side of the shell-and-tube heat exchanger in the chemical plant were 275 °C and 58.48 barg. According to the design specifications, the heat exchanger tubes were rated to withstand temperatures up to 360 °C and pressure up to 72 barg. Figure 1 shows a schematic of the failed shell-and-tube heat exchanger that was investigated in this study. The materials used for the U-bend tube are carbon steel, specifically SA-234 Grade WPB.

The first signs of leakage in several tubes were observed around 6 months after the commencement of operation. The leaking tube was subsequently replaced with a new U-bend tube and joined using GTAW (gas tungsten arc welding), with TG-S50 (Kobelco, Japan) filler metal classified under AWS A5.18 ER70S-G, with a filler diameter of 2.4 mm.

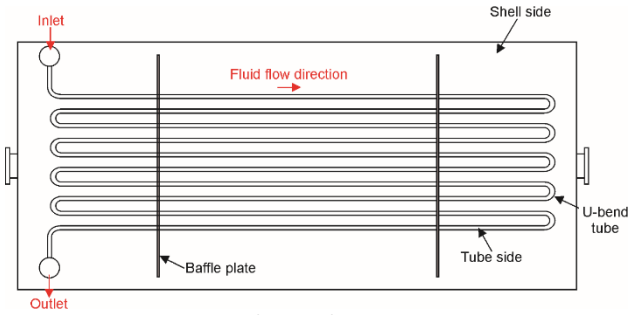

Figure 1. Schematic of the failed shell-and-tube heat exchanger

However, another leak occurred approximately 14 days after the replacement. The failed tube and its condition near the weld metal are shown in Fig. 2.

(a)

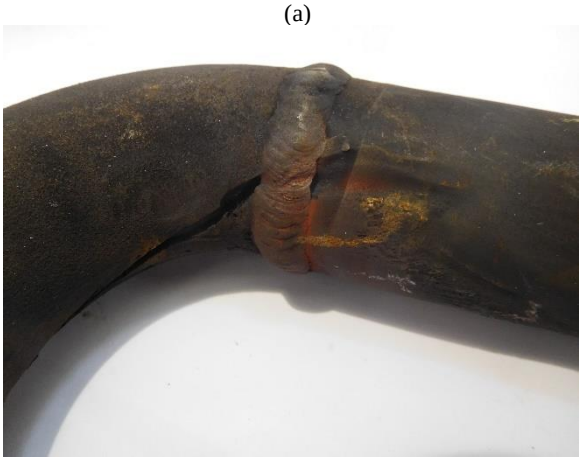

(b)

Figure 2. Photograph of the shell-and-tube heat exchanger (a) overall and (b) near the welded metal

Upon leakage, as indicated by several symptoms presented in Table 1, there was a significant drop in both the pressure inside the tube and temperature. Furthermore, the outlet temperature on the shell side also plummeted to 75.54 °C.

2.2 Method

In the present study, an investigation of all possible causes of failure was carried out through experimental analysis. Visual observations and dye penetrant testing were performed on the failed tube, and macroscopic evaluation was conducted using a stereomicroscope (Olympus SZ61, Japan). Optical emission spectrometry (OES; ARL 3460) was employed to evaluate the chemical composition of the failed tube. The failed tube was carefully cut near the weld, and the surface was cleaned to remove contaminants. Standard metallographic preparation was performed on the sample before observation under an optical microscope (OM; Olympus QX71, Japan).

Table 1. Indications of leakage in the tube during operation

Date	Time	Tube		Shell	
		P (barg)	T (°C)	Inlet T (°C)	Outlet T (°C)
30 Dec	22.11	59.01	274.81	384.42	280.66
31 Dec	10.00	59.15	274.23	384.27	280.76
	10.44	59.09	274.92	384.00	280.45
1 Jan	09.50	59.52	274.66	384.40	274.13
	10.06	55.35	271.99	384.42	235.21
	10.14	39.86	247.95	384.40	202.94
	11.00	13.99	189.80	381.06	75.54
7 Jan	09.00	59.35	276.41	384.60	282.07
	10.00	59.30	276.46	384.77	282.17
	11.00	59.19	276.34	384.73	282.04

To obtain more detailed information on chemical structure, an EDX (energy dispersive X-ray spectroscopy), which was equipped with the SEM (scanning electron microscope) Hitachi SU 3500 Japan, was utilized to observe the chemical structure of deposits. The mechanical properties of the failed tube were determined using the micro-Vickers hardness method with a universal hardness tester (Zwick Roell ZHU250CL, Germany).

3. Results and Discussion

3.1 Macroscopic Examination

Figure 3 shows the macroscopic evaluation of the failed U-bend tube after dye penetrant testing was conducted. The red areas in the image indicate defects revealed by the dye penetrant test. Several defects were observed in the failed U-bend tube. A continuous defect is observed around the joint area, as shown in Fig. 3(a). As seen from Figure 3(b), there are several holes in the outer surface of the failed tube, as shown by arrows. The formation of small holes in the outer surface of the failed tube is indicative of pitting corrosion. In the weld metal region, penetration is insufficient, as shown in Fig. 3(c). This indication refers to the condition in which the top part of the weld joint does not fuse with the base metal. These macroscopic defects indicate potential sites of stress concentration, which may serve as preferential locations for crack initiation under internal pressure and elevated operating temperatures.

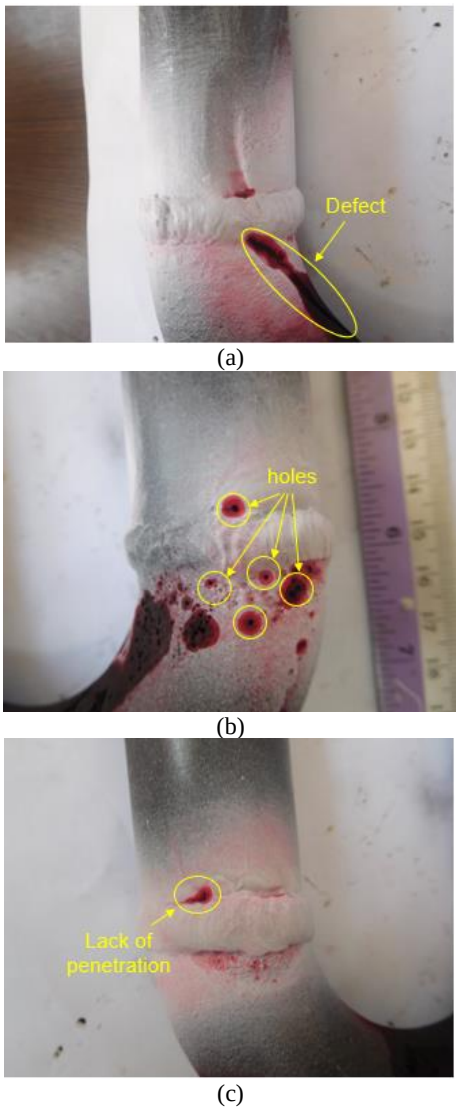

Figure 3. Macroscopic evaluation of defect types (a) continuous defect, (b) small holes, and (c) lack of penetration in the failed tube

3.2 Chemical Analysis

The chemical composition of the U-bend tube was tested using OES and compared with the standard specification of SA-234 Grade WPB. The results of the OES analysis, as shown in Table 2, indicate that the failed tube contains a carbon (C) composition exceeding 0.3 wt.%, which exceeds the carbon content specified in the standard material.

Table 2. Chemical composition of the U-bend failed tube

Element (wt.%)	Standard	Sample
C	0.300 Max	0.324
Si	0.100 Min	0.237
S	0.058 Max	0.001
P	0.050 Max	0.006
Mn	0.290-1.060	0.621
Ni	0.400 Max	0.009
Cr	0.400 Max	0.081
Mo	0.150 Max	0.020
Fe	Bal.	Bal.

Since carbon plays a vital role in microstructural transformations and the mechanical properties of steel, excessive carbon may significantly contribute to the failure of the shell-and-tube heat exchanger. The excess carbon content is significant because it promotes the formation of brittle microstructural features, such as Widmanstätten ferrite, thereby increasing crack susceptibility during service.

3.3 Hardness

The micro-Vickers hardness test was conducted to measure the hardness of the U-bend-failed tube using a 1 kg load. Measurements were taken in three different areas of the sample – the weld metal, the heat-affected zone (HAZ), and the base metal – with three indentations performed in each region. The hardness values of the failed U-bend tube are presented in Table 3. The hardness results indicate that the weld metal has the highest average hardness among the regions, although the difference is not statistically significant, with an average hardness of 205 HV. Meanwhile, the hardness testing results in the HAZ area show an average of 199 HV, whereas the base metal exhibits the lowest average of 184 HV.

Table 3. Hardness test results of the failed U-bend tube sample

Test No.	Sample		
	Weld metal	HAZ	Base metal
1	207	202	185
2	208	193	183
3	201	199	180
4	203	200	187
Average	205	199	184

3.4 Microscopic Examination

A sample was carefully cut from the welded joint of the failed U-bend tube, then ground with silicon carbide (SiC) grade 60-1500, polished with alumina paste (Al_2O_3), and etched with Nital. The morphology of the sample is divided into three distinct areas: the weld metal, the HAZ, and the base metal. Figure 4(a) shows a low-magnification overview of the weld metal and adjacent HAZ from the sample. The region adjacent to the weld metal exhibits microstructural features characteristic of the HAZ, with a gradual variation in grain size due to thermal gradients during welding.

The microstructure of the welded metal consists of evenly dispersed acicular ferrite phase and bainite throughout the welded metal, as can be seen in Fig. 4(b). The acicular ferrite can be differentiated by morphological observation because it forms a microstructure called small, non-aligned grains. The formation of the acicular ferrite microstructure may result from inclusions as a driving force for nucleation. The generation of thermal strains in the austenite phase or the formation of solute-depleted regions are the most likely mechanisms for this phenomenon [12]-[13]. A previous study also reported that the acicular ferrite microstructure on the weld metal provides an optimum combination of strength and toughness [14]. On the other hand, bainite (lath structures) is identified as a ferrite arranged in parallel positions. They can be characterized by more than two parallel lath ferrites within a single prior-austenite grain [12].

Figure 4(c) depicts the microstructure of the HAZ from the failed tube sample. Depending on the distance from the weld metal, the HAZ area can be divided into two distinct subzones: the coarse-grain HAZ (CGHAZ) and the fine-grain HAZ (FGHAZ). Several studies have reported that the peak temperature and cooling rate influence microstructural evolution in the HAZ in each subzone. Therefore, the effects of these two parameters can be correlated with the distance from the weld metal [15]-[18]. These subzones exhibit distinct mechanical and physical properties that may constitute weak points in the welded joint.

Several microstructures were observed in the base metal, as presented in Fig. 4(d). Pearlite is the dominant phase, while three distinct types of ferrite (α) can also be observed in the microstructure. The α-phase, with a plate-like or needle-like morphology, is known as α-Widmanstätten. This type of ferrite is usually undesirable because it reduces steel toughness and increases susceptibility to brittle fracture. This

structure is also classified as an unfavorable microstructure in carbon steel. The presence of Widmanstätten ferrite reduces toughness and increases susceptibility to brittle fracture, particularly under combined thermal and mechanical loading.

Other ferrite types observed in the microstructure include α-idiomorphic and α-allotriomorphic. These two types of ferrite have long been classified as transformation products of austenite, as their formation is strongly influenced by nucleation site location. In the case of α-idiomorphic, nucleation is closely associated with the presence of carbides or inclusions inside the grains [19]-[22]. On the other hand, α-allotriomorphic nucleates at the grain boundary of austenite and grows along the boundaries [23]-[24].

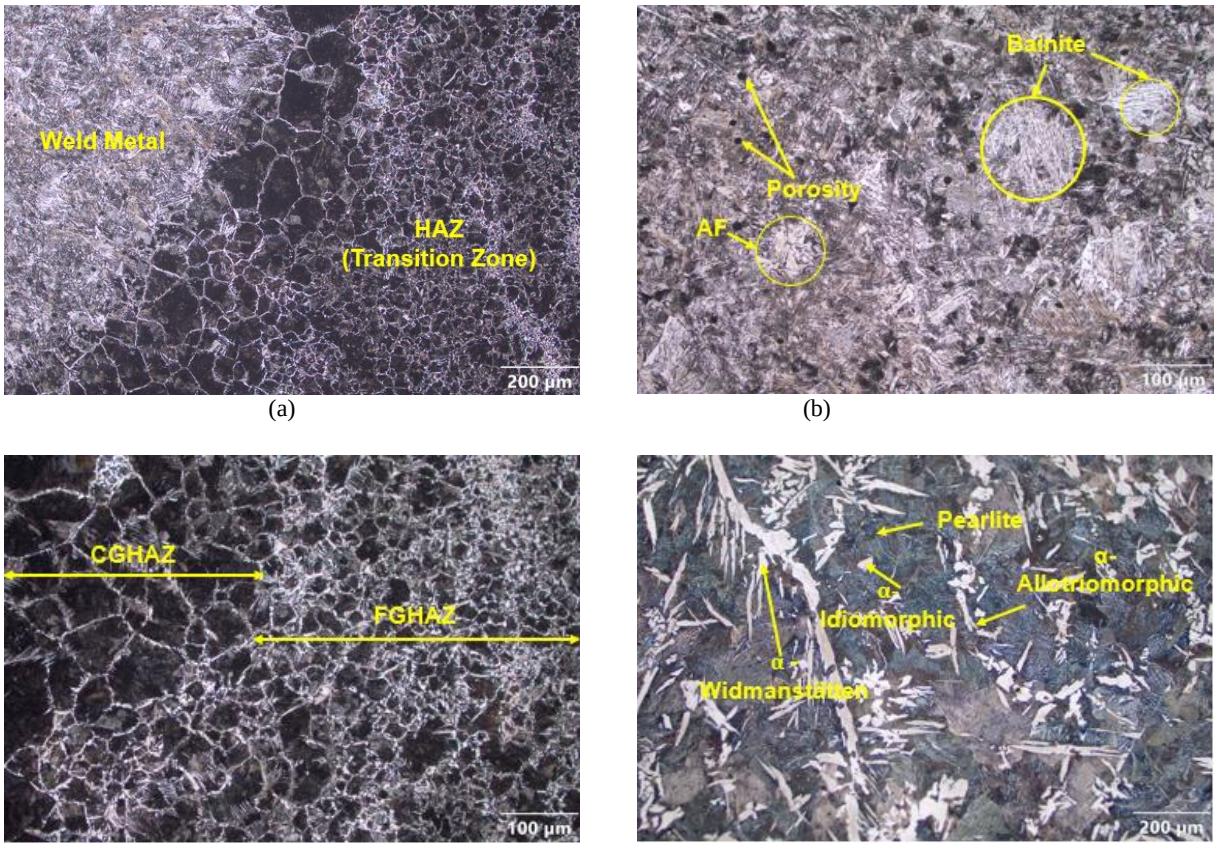

Figure 4. Metallurgical microstructure of the failed U-bend tube near the welded joint area, (a) low magnification overview of the welded joint, where the boundaries between the welded metal and HAZ are schematically indicated, (b) the weld metal, (c) the HAZ, and (d) the base metal

Figure 5 illustrates the metallurgical microstructure around the welded joint area of the failed tube. Numerous small porosities formed in the weld metal during welding, and a large porosity is present near the weld-base metal interface. Furthermore, the welding process appears to have been improperly performed, as evidenced by a lack of fusion between the weld metal and the base metal.

EDS analysis was conducted to investigate the potential for corrosion on the inner surface of the failed tube. As indicated by the white region in Fig. 6, the results revealed the existence of the oxygen (O) element. This element may react with Fe to form iron oxide, such as FeO, Fe_2O_3, or Fe_3O_4 on the surface of the failed tube. The formation of these compounds indicates that corrosion has occurred in the failed tube.

3.5 Root Causes Analysis

Owing to the complexity of the structure and operating conditions in shell-and-tube heat exchangers, several types of failure commonly occur, including corrosion and poor weld quality. Corrosion is a common cause of failure in this type of heat exchangers and is often triggered by water containing minerals or other corrosive substances. A different kind of failure that could occur in the failed tube is triggered by poor welding quality.

In this study, the chemical composition of the failed tube material does not comply with the material standard. The failed tube contains 0.324

wt.% C, which is 0.024 wt.% higher than the maximum requirements specified by the standard. Additionally, the Si content is also 0.137 wt.% higher than the standard value. These deviations may increase the tube's hardness and tensile strength. This condition may be further aggravated by the formation of Widmanstätten structures, which reduce the tube's toughness.

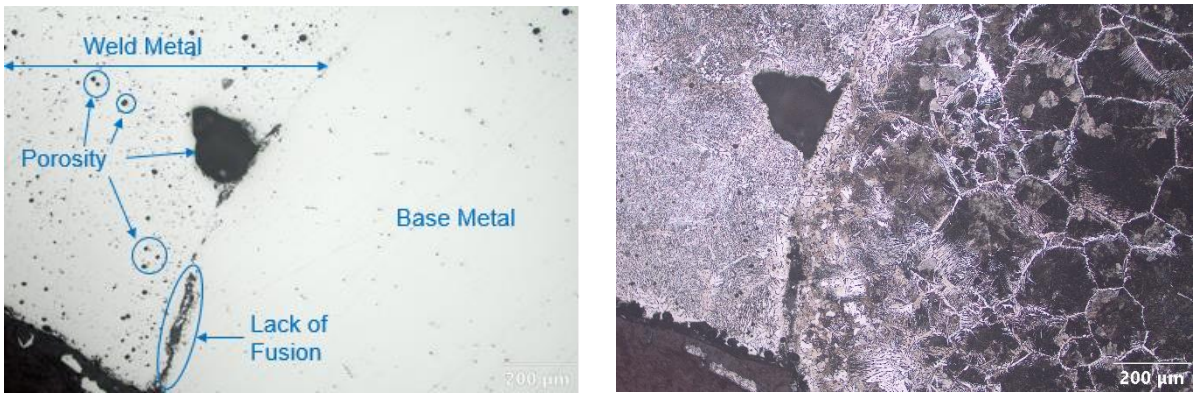

(a) (b)

Figure 5. Metallurgical microstructure of the welded joint area (a) without etching and (b) with 3% Nital etching

Welding quality is considered a primary cause of tube failure, as evidenced by multiple welding defects. These defects act as stress concentrators within the tube material. When the tube is subjected to internal loading from pressurized fluid flow and to elevated temperatures during operation, initial defects formed during welding tend to open, expand, and eventually allow fluid to leak from the tube.

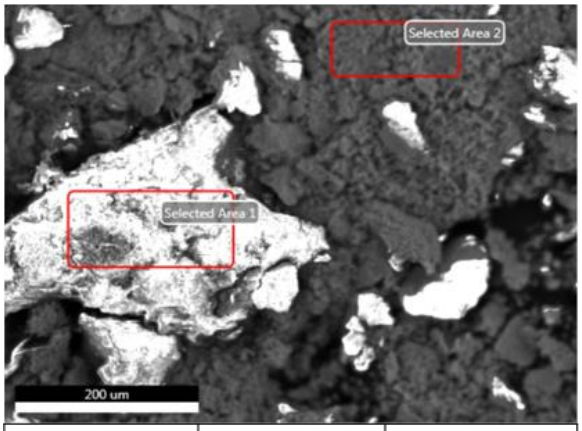

Element	wt.%	at.%
C K	48.22	63.74
O K	30.34	30.11
S K	0.28	0.14
Fe K	21.17	6.02

Figure 6. EDS results of the failed U-bend tube sample

Leakage of pressurized fluid from the tube, along with high temperatures on the shell side, promotes corrosion and erosion of the tube's outer surface. This is evidenced by the presence of oxygen on the tube surface, indicating the formation of iron oxides such as FeO, Fe_2O_3, or Fe_3O_4. Meanwhile, erosion is identified by the continuous appearance of surface defects on the tube exterior, as shown in Fig. 3(a).

Based on the combined macroscopic, chemical, mechanical, and microstructural analyses, the failure mechanism can be described as a sequential process in which material non-compliance promoted unfavorable microstructural features, welding defects acted as stress-concentration sites, and operational pressure and temperature facilitated crack opening and leakage. Subsequent erosion-corrosion further accelerated material degradation, leading to premature failure.

4. CONCLUSION

The interaction among material non-compliance, welding defects, and operational loading conditions led to the premature failure of the U-bend tube in the shell-and-tube heat exchanger. The carbon content of the tube (0.324 wt.%) exceeded the allowable limit, promoting the formation of Widmanstätten ferrite, thereby reducing toughness and increasing crack susceptibility. Welding defects, particularly porosity and lack of fusion, were identified as the primary initiation sites for failure. These defects produced localized stress concentrations that progressively opened under internal pressures of 58.48 barg and elevated operating temperatures of 275 °C. Hardness variations across the welded joint (184-205 HV) further indicate microstructural heterogeneity that contributed to mechanical instability. Following leakage, the interaction between the high-temperature fluid and the tube exterior accelerated erosion-

corrosion, as evidenced by iron oxide formation detected by EDS analysis. The findings highlight the necessity of strict control of material composition, improved welding procedures, and post-weld inspection. Future work should focus on quantitative life prediction models and process optimization for welded U-bend components operating under high-pressure and high-temperature conditions.

ACKNOWLEDGEMENT

The authors thank Yun Gemilang and Lili Hariyadi of the Materials Laboratory at Bandung Polytechnic for their assistance.

REFERENCES

[1] C. Wu, H. Yang, X. He, C. Hu, L. Yang, and H. Li, "Principle, development, application design and prospect of fluidized bed heat exchange technology: Comprehensive review," *Renewable and Sustainable Energy Reviews*, vol. 157, p. 112023, 2022. DOI:10.1016/j.rser.2021.112023.

[2] E. Purnomo, A. Wiranata, and M. A. Muflikhun, "Microstructural and mechanical characterization of u-bend economizer failures: Integrating experimental testing and CFD simulation," *Journal of Materials Research and Technology*, vol. 36, pp. 4692-4702, 2025. DOI:10.1016/j.jmrt.2025.04.178.

[3] C. R. d. F. Azevedo, F. B. Neto, S. D. Brandi, and A. P. Tschiptschin, "Cracking of 2.25 Cr-1.0 Mo steel tube/stationary tube-sheet weldment of a heat-exchanger," *Engineering Failure Analysis*, vol. 15, no. 6, pp. 695-710, 2008. DOI:10.1016/j.engfailanal.2007.06.013.

[4] L. Liu, N. Ding, J. Shi, N. Xu, W. Guo, and C.-M. L. Wu, "Failure analysis of tube-to-tubesheet welded joints in a shell-tube heat exchanger," *Case Studies in Engineering Failure Analysis*, vol. 7, pp. 32-40, 2016. DOI:10.1016/j.csefa.2016.06.002.

[5] R. T. Mousavian, E. Hajjari, D. Ghasemi, M. K. Manesh, and K. Ranjbar, "Failure analysis of a shell-and-tube oil cooler," *Engineering Failure Analysis*, vol. 18, no. 1, pp. 202-211, 2011. DOI:10.1016/j.engfailanal.2010.08.022.

[6] H. Panahi, A. Eslami, M. Golozar, and A. A. Laleh, "An investigation on corrosion failure of a shell-and-tube heat exchanger in a natural gas treating plant," *Engineering Failure Analysis*, vol. 118, p. 104918, 2020. DOI: 10.1016/j.engfailanal.2020.104918.

[7] S. Xu, C. Wang, and W. Wang, "Failure analysis of stress corrosion cracking in heat exchanger tubes during start-up operation," *Engineering Failure Analysis*, vol. 51, pp. 1-8, 2015. DOI: 10.1016/j.engfailanal.2015.02.005.

[8] Z. G. Yang, Y. Gong, and J. Z. Yuan, "Failure analysis of leakage on titanium tubes within heat exchangers in a nuclear power plant. Part I: Electrochemical corrosion," *Materials and Corrosion*, vol. 63, no. 1, pp. 7-17, 2012. DOI:10.1002/maco.201106189.

[9] M. Rezaei, Z. Mahidashti, S. Eftekhari, and E. Abdi, "A corrosion failure analysis of heat exchanger tubes operating in petrochemical refinery," *Engineering Failure Analysis*, vol. 119, p. 105011, 2021. DOI:10.1016/j.engfailanal.2020.105011.

[10] V. Korobko, A. Shevtsov, S. Serbin, H. Wen, and M. Dzida, "Impact of the type of heat exchanger on the characteristics of low-temperature thermoacoustic heat engines," *International Journal of Thermofluids*, vol. 24, p. 100953, 2024. DOI:10.1016/j.ijft.2024.100953.

[11] F. Yan, H. Lu, and S. Feng, "Numerical simulation of liquified natural gas boiling heat transfer characteristics in helically coiled tube-in-tube heat exchangers," *Frontiers in Heat and Mass Transfer*, vol. 22, no. 5, pp. 1493-1514, 2024. DOI:10.32604/fhmt.2024.055324.

[12] D. Abson, "Acicular ferrite and bainite in C–Mn and low-alloy steel arc weld metals," *Science and Technology of Welding and Joining*, vol. 23, no. 8, pp. 635-648, 2018. DOI:10.1080/13621718.2018.1461992.

[13] A. Takada, H. Terasaki, and Y. Komizo, "Effect of aluminium content on acicular ferrite formation in low carbon steel weld metals," *Science and Technology of Welding and Joining*, vol. 18, no. 2, pp. 91-97, 2013. DOI:10.1179/1362171812Y.0000000086.

[14] S. S. Babu, "The mechanism of acicular ferrite in weld deposits," *Current opinion in solid state and materials science*, vol. 8, no. 3-4, pp. 267-278, 2004. DOI:10.1016/j.cossms.2004.10.001.

[15] M. Amraei, S. Afkhami, V. Javaheri, J. Larkiola, T. Skriko, T. Björk, and X. L. Zhao, "Mechanical properties and microstructural evaluation of the heat-affected zone in ultra-high strength steels," *Thin-Walled Structures*, vol. 157, p.

107072, 2020. DOI:10.1016/j.tws.2020.107072.
[16] A. Smith, M. Asadikiya, M. Yang, J. Chen, and Y. Zhong, "An investigation of creep resistance in grade 91 steel through computational thermodynamics," *Engineering*, vol. 6, no. 6, pp. 644-652, 2020. DOI:10.1016/j.eng.2019.12.004.
[17] S. Afkhami, V. Javaheri, M. Amraei, T. Skriko, H. Piili, X. L. Zhao, and T. S. Björk, "Thermomechanical simulation of the heat-affected zones in welded ultra-high strength steels: Microstructure and mechanical properties," *Materials & Design*, vol. 213, p. 110336, 2022. DOI:10.1016/j.matdes.2021.110336.
[18] H. Zhou, Q. Zhang, B. Yi, and J. Wang, "Hardness prediction based on microstructure evolution and residual stress evaluation during high tensile thick plate butt welding," *International Journal of Naval Architecture and Ocean Engineering*, vol. 12, pp. 146-156, 2020. DOI:10.1016/j.ijnaoe.2019.09.004.
[19] C. Capdevila, F. G. Caballero, C. García-Mateo, and C. G. De Andrés, "The role of inclusions and austenite grain size on intragranular nucleation of ferrite in medium carbon microalloyed steels," *Materials transactions*, vol. 45, no. 8, pp. 2678-2685, 2004. DOI:10.2320/matertrans.45.2678.
[20] M. Y. Chen, H. W. Yen, and J. R. Yang, "The transition from interphase-precipitated carbides to fibrous carbides in a vanadium-containing medium-carbon steel," *Scripta Materialia*, vol. 68, no. 11, pp. 829-832, 2013. DOI:10.1016/j.scriptamat.2013.01.020.
[21] Y. Chi, Y. Tsai, B. Huang, and J. Yang, "Investigation of idiomorphic ferrite and allotriomorphic ferrite using electron backscatter diffraction technique," *Materials Science and Technology*, vol. 33, no. 5, pp. 537-545, 2017. DOI:10.1080/02670836.2016.1216027.
[22] T. Yokomizo, M. Enomoto, O. Umezawa, G. Spanos, and R. Rosenberg, "Three-dimensional distribution, morphology, and nucleation site of intragranular ferrite formed in association with inclusions," *Materials Science and Engineering: A*, vol. 344, no. 1-2, pp. 261-267, 2003. DOI:10.1016/S0921-5093(02)00411-2.
[23] C. Capdevila, F. Caballero, and C. García de Andrés, "Modeling of kinetics of austenite-to-allotriomorphic ferrite transformation in 0.37 C-1.45 Mn-0.11 V microalloyed steel," *Metallurgical and Materials Transactions A*, vol. 32, pp. 661-669, 2001. DOI:10.1007/s11661-001-1001-1.
[24] W. Lange, M. Enomoto, and H. Aaronson, "The kinetics of ferrite nucleation at austenite grain boundaries in Fe-C alloys," *Metallurgical Transactions A*, vol. 19, pp. 427-440, 1988. DOI:10.1007/BF02649256.

AUTHOR INDEX

SUBJECT INDEX